

Site U1391¹

Expedition 339 Scientists²

Chapter contents

Background and objectives	1
Operations	2
Lithostratigraphy	3
Biostratigraphy	6
Paleomagnetism	9
Physical properties	10
Geochemistry	13
Downhole measurements	15
Stratigraphic correlation	16
References	17
Figures	20
Tables	81

Background and objectives

Integrated Ocean Drilling Program (IODP) Site U1391 is located on the West Iberian margin ($37^{\circ}21.5322'N$, $9^{\circ}24.6558'W$) and represents the most distal site within the contourite depositional system (CDS) explored during Expedition 339 (Fig. F1, F2). It is situated over a large plastered drift on the middle slope terrace from Sector 5 of the CDS (the canyons sector in Stow et al., 2011, previously defined by Hernández-Molina et al., 2003, and Llave et al., 2007). This site represents an opportunity for recovering a sedimentary record for the Quaternary and Pliocene caused by Mediterranean Outflow Water (MOW) deposition on the southwest Portuguese margin (see Fig. F21 in the “Expedition 339 summary” chapter [Expedition 339 Scientists, 2013a]).

Regional work has determined the tectonic and stratigraphic evolution of this part of the margin. These previous studies identified that the sedimentary record of the southwest Portuguese margin spans from the Late Triassic through Quaternary and consists of Mesozoic rift and postrift sediments deformed during the Cenozoic alpine compression (Terrinha et al., 2003). Major unconformities/hiatuses generated during this tectonic inversion phase separate Late Cretaceous from middle Eocene sediments and late Eocene from early Miocene sediments (Alves et al., 2003; Pereira et al., 2011). The present-day morphostructural attributes of the margin are the result of the middle Miocene uplift of fault blocks inherited from the Mesozoic rifting phases. This structural compartmentalization of the margin controlled its tectonic and sedimentary evolution during the Pliocene and Quaternary transpressive regime because of the activity of some structures located near Site U1391, such as the São Vicente Canyon and Horseshoe faults to the south, the Pereira de Sousa fault to the north, and the Marquês de Pombal fault to the east (e.g., Alves et al., 2000; Terrinha et al., 2003; Zitellini et al., 2004).

In this morphostructural context, contourite features developed over the middle slope as a northward extension of the CDS from the Gulf of Cádiz. As no previous work has been published on contourite sedimentation along this margin, the results from this site are very important for increasing the knowledge of margin evolution. The plastered drift at this site is one of a series of contourite features formed under the influence of the northern branch of MOW as it continues north along the Iberian margin and beyond (Iorga and Lozier, 1999; Serra et al., 2010). These in-

¹Expedition 339 Scientists, 2013. Site U1391. In Stow, D.A.V., Hernández-Molina, F.J., Alvarez Zarikian, C.A., and the Expedition 339 Scientists, *Proc. IODP, 339: Tokyo* (Integrated Ocean Drilling Program Management International, Inc.).

doi:10.2204/iodp.proc.339.109.2013

²Expedition 339 Scientists' addresses.



clude those along the middle slope of the northwest Portuguese margin (Alves et al., 2003; Pereira and Alves, 2011), the Galicia Bank and Galician slope (Ercilla et al. 2009, 2010, 2011; Bender et al. 2010; Mena et al. 2010), Ortegal Spur (Hernández-Molina et al. 2009), Le Danois Bank or “Cachucho” (Ercilla et al. 2008; Iglesias, 2009; Van Rooij et al. 2010), and the Porcupine slope (Van Rooij et al. 2003).

Objectives

The major objective for Site U1391 was to recover a sedimentary contourite record for the Pliocene and Quaternary deposited under the influence of MOW along the West Iberian margin (see Fig. F21 in the “Expedition 339 summary” chapter [Expedition 339 Scientists, 2013a]). This record will allow us to investigate more specific objectives including

- The influence of the Strait of Gibraltar (or Gibraltar Gateway) through the Pliocene and the Quaternary in the West Iberian margin,
- MOW paleoceanography and its global climate significance during the last 4 m.y.,
- The effects of climate and sea level changes on the sediment architecture of the plastered drift on the middle slope off Portugal, and
- The sedimentary stacking pattern of the plastered drift in relation to changes in sea level and other forcing mechanisms.

To achieve these major scientific objectives, it is essential to integrate the results from Site U1391 with a network of existing seismic reflection profiles from the Portuguese margin and to correlate these with results from the Gulf of Cádiz.

Operations

The 115 nmi voyage from Site U1390 to Site U1391 (proposed Site WI-01B) was made at an average speed of 11.5 kt. The vessel was positioned on the last site of the expedition at 1230 h on 8 January 2012.

Three holes were drilled at Site U1391 (Table T1). Hole U1391A was cored using the advanced piston corer (APC) to 171.1 meters below seafloor (mbsf) and then with the extended core barrel (XCB) to 353.1 mbsf. Hole U1391B was cored using the APC to 171 mbsf and then with the XCB to 353.5 mbsf. Hole U1391C was drilled without recovery to 340 mbsf and then cored using the rotary core barrel (RCB) to 671.5 mbsf. Downhole logging was carried out in Hole U1391C using the triple combination (triple combo) and Formation MicroScanner (FMS)-sonic tool strings (see “[Downhole logging at Site U1391](#)”). Overall recovery at Site U1391 was 342.1

m (104.7% recovery) with the APC, 230.7 m (90.7% recovery) with the XCB, and 269.02 m (81.15% recovery) with the RCB. The total cored interval at Site U1391 was 1038.1 m and total recovery was 958.57 m (92.3%).

Hole U1391A

The APC/XCB bottom-hole assembly (BHA) was made up, and a routine survey of the seafloor was conducted using a 30 m grid pattern. No significant obstructions were observed. Hole U1391A was spudded with the APC at 1080.0 meters below sea floor (mbrf; 1078.3 meters below sea level [mbsl]) at 2035 h on 8 January. Seafloor depth was established at 1085.4 mbrf (1073.7 mbsl). Piston coring advanced to a final depth of 171.1 mbsf, with a recovery of 106%. Cores were oriented starting with Core 4H. Temperature measurements were made at 32.6 (Core 4H), 61.1 (Core 7H), 89.6 (Core 10H), 118.1 (Core 13H), and 146.6 (Core 16H) mbsf. Nonmagnetic core barrels were used to obtain all piston cores. XCB coring deepened the hole to the depth objective of 353.1 mbsf by 0345 h on 10 January. Average recovery for the 182 m XCB interval was 88.8%. Combined recovery in Hole U1391A was 97%. The drill string was pulled out of the hole, clearing the seafloor at 0520 h on 10 January. The vessel was offset 20 m south of Hole U1391A.

Hole U1391B

Hole U1391B was spudded with the APC at 1085 mbrf at 0815 h on 10 January. Although the mudline core was 9.65 m, the desired vertical offset (5 m deeper) with the previous hole was maintained and piston coring continued to a final depth of 171 mbsf with a recovery of 104%. Cores were oriented starting with Core 3H. Temperature measurements were made at 19 (Core 2H), 47.5 (Core 5H), 76 (Core 8H), 104.5 (Core 11H), and 133 (Core 14H) mbsf. All cores were obtained with nonmagnetic core barrels. XCB coring deepened the hole to the depth objective of 353.5 mbsf. Average recovery for the XCB interval of 182.5 m was 93%. Combined recovery for Hole U1391B was 98%. The drill string was recovered with the bit clearing the seafloor at 1350 h and the rotary table at 1850 h on 11 January. The trip out of the hole was suspended 1.5 h for the routine maintenance procedure of slipping and cutting the drilling line.

Hole U1391C

A four-stand RCB BHA was made up with a new CC-4 Rock Bit International bit and mechanical bit release and deployed. After the driller tagged the sea-



floor at 1085 mbrf (1073.3 mbsl), Hole U1391C was spudded with the RCB at 2345 h on 11 January. The hole was drilled with a wash barrel to 340 mbsf by 1400 h on 12 January. The empty wash barrel was recovered and a fresh core barrel dropped at 1430 h, when rotary coring was initiated. Rotary coring advanced to a final depth of 671.5 mbsf by 1645 h on 14 January. Recovery for the 331.5 m cored interval in Hole U1391C was 81%. Recovery percentage was adversely affected by the absence of recovery in Cores 26R, 29R, and 35R, which was assumed to be formation related. The average rate of penetration for the 331.5 m cored interval was 14.2 m/h.

Downhole logging at Site U1391

Following the wiper trip, Hole U1391C was flushed with sepiolite mud and the bit was released at the bottom. The hole was displaced with 248 bbl of 10.5 ppg heavy mud, and the end of pipe was placed at the logging depth of 98.9 mbsf. The first log of the hole was made with the triple combo tool string, which was made up of the natural gamma radiation (NGR), density, and resistivity tools and deployed at 0330 h on 15 January. The tool string succeeded in reaching 668 mbsf. The tool string was recovered and rigged down by 0815 h. The second and final log was made with the FMS-sonic tool string. The tool string reached 666 mbsf and recorded resistivity images of the borehole, sonic velocities, and NGR data. The hole contained many thin washouts. As at previous sites, all the logs have medium-amplitude alternations on the several-meter scale. Sonic velocity, density, and resistivity all show a downhole compaction trend. Logging equipment was rigged down by 1915 h, concluding all science operations of the expedition. We departed Site U1391 at 0200 h on 16 January.

Expedition 339 ended at 1342 h on 16 January, with the first line ashore in Lisbon, Portugal.

Lithostratigraphy

Drilling at Site U1391 recovered a 670.98 m thick sedimentary section (Figs. F3, F4). The shipboard lithostratigraphic program involved detailed visual assessment of grain size, sediment color, sedimentary structures, and bioturbation intensity to describe the facies and facies associations at Site U1391. Petrographic analysis of smear slides taken regularly from Holes U1391A ($n = 87$) and U1391C ($n = 44$) were used to assess average grain size and composition of the sediments to aid in the descriptive sediment classification. Additional smear slides were taken from

Hole U1391B ($n = 5$) at specific locations for correlation with Hole U1391A. Samples were selected from Hole U1391A ($n = 37$) for powder X-ray diffraction (XRD) analysis of bulk mineralogy. No samples were taken from Hole U1391C.

The total carbonate content in these cores, based on shipboard analyses, ranges from 17.5 to 45.2 wt%, although shipboard analyses were only carried out for Hole U1391A (Fig. F5). These results are consistent with the abundance of biogenic carbonate and detrital carbonate estimated from smear slides, so the lithologic names determined from smear slide analyses have been used without modification through this text, the accompanying summary diagrams, and the visual core description sheets. The character of sediment physical properties, including NGR, magnetic susceptibility, color reflectance parameters, and density, records the distribution of these various lithologies and sediment components (see “[Physical properties](#)”). Characteristics of the sedimentary sequence cored at Site U1391, together with some of these additional properties, are summarized in Figure F6.

The sedimentary succession at this site is divided into two lithologic units (I and II). Unit I is characterized by only contourite deposits and has been divided into two subunits (IA and IB). Subunit IA is characterized by sandy contourites and alternating reddish/brownish and greenish gray/greenish calcareous mud. Subunit IB is characterized by fewer and finer-grained contourite sequences, all without sand, and has a higher percentage of biosiliceous sediment. Color alternations in the calcareous mud sequences range from greenish gray to greenish. Unit II has a wider range of facies and features, including a debrite, contourites, a dolomitic mudstone, and microfaults. Unit II also shows less color banding than in Unit I.

General description

Texture

The sediment is fine grained through most of Site U1391 and dominated by the clay size fraction, with sand-sized material only making a minor contribution to the textural characteristics (Fig. F4). Subunit IA has the lowest clay size fraction (54%), followed by silt (31%). Subunit IA also has the highest contribution from the sand size fraction (15%). Sandy mud and silty sands, at times with biogenic carbonate, have an average grain size from very fine to fine sand with a maximum grain size of medium sand. Silty and sandy units are generally poorly sorted, and detrital siliciclastic grains are subrounded to rounded.

Detrital carbonate grains are generally subrounded to subangular, and many are abraded, indicating reworking. Subunit IB shows a slight increase in the clay size fraction to 65% and a decrease in the sand size fraction to 8%. Unit II shows similar textural characteristics to Subunit IB, with clay at 61% and sand at 9% (Table T2).

Bioturbation is the most obvious secondary sedimentary structure in cores collected from Site U1391. The most common indicators of bioturbation are diffuse centimeter-scale mottling and millimeter-scale pyritic burrow fills. Black iron sulfide mottling is also common. Discrete burrows and recognizable ichnofossils are rare; those present occur in a few beds with discrete burrows of *Chondrites* and *Zoophycos*. The bioturbation index ranges from sparse to slight.

Composition

All lithologies at Site U1391 are similar in composition, with only subtle changes in abundance between Subunits IA and IB and Unit II (Fig. F4; Table T2). All lithologic units and subunits have a relatively even contribution of terrigenous components including siliciclastics (quartz, feldspars, heavy minerals, clay minerals, and volcanic glass), detrital carbonate, and biogenic components (mainly calcareous nannofossils with rare to common foraminifers). Biogenic silica components are rare but when present include sponge spicules and fragmented radiolarians. Unit II has slightly more biogenic silica than Subunits IA or IB (7% in Unit II versus 3% in Unit I; Fig. F4). No discrete ash or dust layers and no dropstones were observed. Authigenic products, such as pyrite (usually classified as opaque mineral grains) and dolomite, are also present in minor amounts throughout Unit I (<1%).

Thirty-seven samples were selected from Hole U1391A for powder XRD analysis of bulk mineralogy, and nine samples were processed to show the clay mineralogy of the clay size fraction. Twenty-one of the bulk samples and six of the clay samples were from Subunit IA, and sixteen of the bulk samples and four of the clay samples were in Subunit IB (Fig. F7; Table T3).

Unit/Subunit descriptions

Subunit IA

Intervals: 339-U1391A-1H-1, 0 cm, through 22X-6, 10 cm; 339-U1391B-1H-1, 0 cm, through 20X-CC, 40 cm

Depths: Hole U1391A = 0–196.1 mbsf, Hole U1391B = 0–184.5 mbsf

Age: Holocene and Pleistocene

Lithologies and bedding

The dominant lithology is calcareous mud, alternating in places with biogenic mud. Together these lithologies account for ~90% of the sediment in this subunit. Minor lithologies include calcareous silty mud, calcareous sandy mud, nannofossil mud, and biogenic mud. Calcareous silty sand is rare (Figs. F4, F6).

Structures and texture

Bi-gradiational contouritic sequences are common throughout Subunit IA, with bioturbated and gradational lower and upper contacts and grading from silty clay to silty mud, sandy mud, or silty sand. Some of the bi-gradiational sequences have a sharp to erosional contact in the middle of the sequence. In these cases, part of the underlying inversely graded sequence appears to have been removed by downward erosion of the normally graded sequence. The maximum grain size occurs directly above the erosional contact (Figs. F8, F9, F10). Two of these sequences show foraminifer-rich sand in the basal or upper part (Sections 339-U1391A-6H-4 and 6H-6; Figs. F8, F10). A few sequences with sharp bases and normal grading are also described; the maximum grain size is silty mud, sandy mud, or silty sand. A maximum of seven silty and sandy contouritic beds occur per core in Subunit IA (Fig. F4).

Composition

Subunit IA is dominated by clay-sized (54%) and silt-sized (31%) sediment. Sand-sized sediment is only a minor component (15%). Compositinally, the unit has a relatively constant contribution of siliciclastics (43%), biogenic carbonate (30%), and detrital carbonate (26%) throughout. Biogenic silica makes only a minor contribution (1%), except for one specific bed in Section 339-U1391A-11H-3 in which biogenic silica is up to 50% (Fig. F4).

XRD analyses of 21 bulk samples from Subunit IA record reflections from siliciclastic framework minerals (quartz, K-feldspar, plagioclase, and hornblende), clay minerals (illite, chlorite, kaolinite, and smectite), and carbonates (calcite, dolomite, and rare aragonite). Peak intensities appear fairly constant throughout the subunit. Six clay mineral analyses confirm the presence of smectite in five of the six samples.

Color

Alternating greenish gray intervals and thicker reddish/brownish intervals are common. In the greenish gray intervals, colors range from dark greenish gray (10Y 4/1 and 5GY 4/1) to greenish gray (10Y 5/1



and 5GY 5/1). In the reddish/brownish intervals, colors include dark gray (2.5Y 4/1), dark grayish brown (10YR 4/1 and 2.5Y 4/2), gray (10YR 5/1 and 10Y 6/1), and grayish brown (10YR 5/2 and 2.5Y 5/2) (Fig. F11). Nannofossil mud has a lighter color range of 10Y 5/1, 5GY 5/1, 10YR 5/1, and 10Y 6/1. Biosiliceous mud is commonly greenish in color (5GY 4/1).

Subunit IB

Intervals: 339-U1391A-22X-6, 10 cm, through 38X-CC; 339-U1391B-20X-CC, 40 cm, through 38X-CC; 339-U1391C-2R-1, 0 cm, through 25R-CC

Depths: Hole U1391A = 196.1–353.5 mbsf (bottom of hole [BOH]), Hole U1391B = 184.5–354.5 mbsf (BOH), Hole U1391C = 340.0–566.1 mbsf

Age: Pleistocene

Lithologies and bedding

The dominant lithology is calcareous mud, alternating in places with biogenic mud. Together these lithologies account for ~95% of the sediment in this subunit. The only minor lithology identified is calcareous silty mud (Figs. F4, F6).

Structures and texture

Subunit IB has rare and widely spaced contouritic sequences with a maximum grain size of silty mud and no sand. Only bi-gradational sequences with bioturbated or gradational upper and basal contacts are observed. There is a maximum of four silty mud contouritic beds per core in Subunit IB (Fig. F4). Millimeter-scale laminations in mud and silty mud are observed at 483–485 mbsf (Sections 339-U1391C-17R-3 through 17R-CC) (Figs. F12, F13). The remainder of the unit is described as massive, and sedimentary structures are poorly preserved due to the intensity of bioturbation.

Composition

Subunit IB has the highest clay size fraction (65%). Compared to Subunit IA, this subunit has a similar silt size fraction (27%) and a lower sand size fraction (8%). Compositionally, the unit has very even percentages of siliciclastics (32%), biogenic carbonate (35%), and detrital carbonate (30%). Biogenic silica makes only a minor contribution (3%), except in seven beds where it occurs with percentages from 10% to as high as 52% (Section 339-U1391A-28X-5) (Fig. F4).

The 16 XRD bulk samples from Subunit IB record reflections from siliciclastic framework minerals (quartz, K-feldspar, plagioclase, and hornblende),

clay minerals (illite, chlorite, kaolinite, and smectite), and carbonates (calcite, dolomite, and rare aragonite). Peak intensities appear fairly constant throughout the subunit, and are, on average, 30%–50% higher than in Subunit IA. Smectite is only present in two of the four analyses.

Color: The most common dark colors are dark greenish gray (10Y 4/1) and greenish gray (10YR 5/1 and 10Y 6/1), alternating with thin greenish intervals (5GY 4/1 and 5GY 5/1) (Fig. F14). These color alternations are quite prominent throughout Subunit IB. The downhole cessation of this color alternation is one of the factors used in determining the boundary with Unit II.

Unit II

Interval: 339-U1391C-25R-CC, 16 cm, through 36R-CC (bottom of hole)

Depth: 566.10–670.98 mbsf (bottom of hole)

Age: Pliocene

Lithologies and bedding

The dominant lithology is calcareous mud, alternating with biogenic mud. Together these lithologies account for ~80% of sediments in this unit. Minor lithologies identified include calcareous silty mud and a dolomitic mudstone (Figs. F4, F6).

Structures and texture

Unit II has a wider variety of sedimentary structures than does Unit I, including more silty mud contourite sequences. The contourite beds in Unit II are bi-gradational, several of them with a sharp upper contact (top-cut-out contourite). The base of a debrite (≥ 35 cm thick) occurs at the top of Section 339-U1391C-30R-1 (632.6–633.2 mbsf) (Fig. F15; the overlying Core 29R was not recovered). The debrite intraclasts and the matrix are both muddy. The intraclasts show indications of having been burrowed prior to emplacement, are subrounded to rounded, and are as large as a few centimeters in diameter.

A 56 cm thick dolomitic mudstone bed occurs between 632.6 and 633.2 mbsf (interval 339-U1391C-32R-7, 20–76 cm). This sedimentary rock contains abundant fine dolomite grains as well as a few biosiliceous fossils, such as sponge spicules, and rare calcareous nannofossils (Fig. F16). The mudstone bed is overlain by biosiliceous mud. Millimeter-scale laminations of mud and silty mud with biogenic carbonate occur regularly between 634.5 and 650.1 mbsf (Sections 339-U1391C-33R-2 to 34R-5), some of which appear to be low-angle cross-lamination. A reverse microfault offsetting at least two burrows is



present in Section 339-U1391C-34R-6 (650.1–651.14 mbsf) together with associated dewatering structures (Fig. F17).

Composition

Unit II comprises a dominant clay size fraction (60%), a silt size fraction (31%), and a minor sand size fraction (9%). Compositonally, siliciclastics are the dominant component (40%), and biogenic carbonate (28%) and detrital carbonate (23%) have a relative equal contribution. Unit II has generally higher biogenic silica (7%) than Unit I. This is evident throughout Unit II, whereas in Unit I it is present only in discrete beds (Fig. F4). No XRD samples were processed from this unit.

Color

Unit II displays a dominant greenish gray background color (10Y 4/1 and 10Y 5/1) that alternates with thin and less common ($n = 6$) greenish intervals (5GY 4/1).

Discussion

Textual and compositional characteristics are very uniform throughout Site U1391. Accordingly, lithologic unit and subunit division is based on subtle variations in composition and facies characteristics. Specifically, Subunit IA is characterized by cyclic color alternation between reddish gray and greenish gray. This subunit also contains more silty mud and silty sand units than the underlying units. These silty units have been interpreted as parts of contourite sequences. Stacked contourite sequences are relatively common with top- and/or base-cut-out sequences. Erosional or sharp contacts are common within these stacked sequences, indicating changes in current velocity. Subunit IA correlates with formal and informal Subunit IA at Sites U1386, U1387, and U1389.

Subunit IB has fewer distinct contourite sequences and is dominated by thick beds of calcareous muds with green mottles, some of which are rich in biogenic silica (diatoms and sponge spicules), and laminated. Subunit IB clearly represents a low-energy contourite depositional environment, and the preservation of lamination in parts of the subunit probably indicates periodically decreased oxygenation of the bottom waters resulting in less biological activity (a decrease in bioturbation).

In Unit II (Pliocene), the alternating successions of reddish and green calcareous muds are less obvious and more irregular, suggesting some change in the controls on cyclicity. The dolomitic mudstone in Unit II occurs at a similar stratigraphic position as

that observed at Site U1387, and we would interpret a similar formation mechanism linked with a hiatus in sedimentation. This is clear evidence for widespread strong bottom current activity linked with MOW intensification at ~3 Ma.

Debrites and microfaulting are also present in Unit II, the latter perhaps indicative of slump-slide processes. Both deformation features indicate slope instability and downslope mass movement that might be related to regional tectonic activity.

Biostratigraphy

Sediments at Site U1391 date from the Holocene to the late Pliocene (Fig. F18; Table T4), with the base age of Hole U1391C estimated to span between 3.31 and 3.5 Ma. Site U1391 shows a continuous record with some changes in sedimentation rates. For the Pleistocene, from the seafloor to ~1.5 Ma, a sedimentation rate of 27 cm/k.y. was estimated, whereas during the early Pleistocene (1.5–2.588 Ma), it is 17 cm/k.y. The Pliocene records the lowest values with an estimation of 13 cm/k.y.

The microfossil content of sediment recovered at Site U1391 is usually high. The samples are rich in planktonic and benthic foraminifers as well as calcareous nannofossils (Tables T5, T6). Ostracods are present but were not studied in this site.

Pollen and spores are abundant in the eight samples analyzed in Holes U1391A and U1391C. Total pollen and spore concentrations range from ~12,000 to 48,000 grains/cm³, excluding Sample 339-U1391A-35X-CC in which the amount is surprisingly an order of magnitude higher, exceeding 170,000 grains/cm³. The preservation of the grains is mostly good to moderate. The proportion of unidentifiable grains progressively increases downhole, as is the case at Sites U1387, U1389, and U1390 (see Fig. F26 in the “Site U1387” chapter, Fig. F22 in the “Site U1389” chapter, and Fig. F21 in the “Site U1390” chapter [Expedition 339 Scientists, 2013d, 2013e, 2013f]). We also observed microcharcoal particles and dinocysts.

Calcareous nannofossils

We examined all core catcher samples from Holes U1391A–U1391C for calcareous nannofossil biostratigraphy. Additionally, selected samples from Hole U1391A were analyzed in order to constrain biohorizons, paying attention only to marker species. Calcareous nannofossil assemblages are very abundant to common and diverse, and the preservation is good to moderate. Small placoliths (<3 µm) and occasionally medium placoliths (3–5 µm) dominate the assemblages.



In total, 12 Pleistocene and Pliocene nannofossil datums defined and/or calibrated by Raffi et al. (2006 and references therein) and Flores et al. (2010) were identified in the holes (Table T4). Inorganic input and reworking of early Neogene and Paleogene species vary from few to common throughout all sections (Table T5).

The change in abundance of large *Emiliania huxleyi* ($>4\text{ }\mu\text{m}$) that characterizes Termination 1 in mid- to low-latitude water masses in the Atlantic Ocean has been proven as a useful event by Flores et al. (2010). This change in abundance was recorded between Samples 339-U1391A-1H-2, 142 cm, and 1H-3, 60 cm (2.92–3.60 mbsf), and between the top of Hole U1391B to 1H-CC (0–9.61 mbsf), making it possible to distinguish the onset of the Holocene.

The first occurrence (FO) of *E. huxleyi* (0.26 Ma), which marks the base of Zone NN21, was placed between Samples 339-U1391A-8H-CC and 9H-1, 75 cm (70.18–71.35 mbsf), and between 339-U1391B-7H-CC and 8H-CC (67.07–76.94 mbsf). However, this event should be taken with caution because of dissolution effects and the low proportion of this species. The last occurrence (LO) of *Pseudoemiliania lacunosa* (0.46 Ma), considered a globally synchronous event that defines the top of Zone NN19, occurs between Samples 339-U1391A-13H-5, 75 cm, and 13H-6, 75 cm (114.57–115.95 mbsf), and between 339-U1391B-12H-CC and 13H-CC (114.83–123.75 mbsf).

A biohorizon considered useful in Pleistocene sediments is the LO of *Reticulofenestra asanoi* (0.90 Ma), which was placed between Samples 339-U1391A-25X-CC and 26X-3, 84 cm (227.46–231.11 mbsf), and between 339-U1391B-25X-CC and 26X-CC (231.21–240.53 mbsf). The FO of *R. asanoi* (1.07 Ma), another significant event for the Pleistocene, was recorded between Samples 339-U1391A-32X-5, 60 cm, and 32X-7, 60 cm (291.84–294.70 mbsf), and between 339-U1391B-32X-CC and 33X-CC (298.63–308.79 mbsf). To define these biohorizons, we considered specimens of *R. asanoi* $\geq 6\text{ }\mu\text{m}$ in size.

The LO of large *Gephyrocapsa* spp. ($>5.5\text{ }\mu\text{m}$) (1.24 Ma) was recorded between Samples 339-U1391A-36X-CC and 37X-1, 75 cm (334.10–343.25 mbsf), and between 339-U1391B-35X-CC and 36X-CC (328.74–338.45).

The LO of *Helicosphaera sellii* (1.25 Ma) was identified between Samples 339-U1391A-37X-CC and 38X-CC (343.25–353.10 cm) and between 339-U1391B-35X-CC and 36X-CC (328.74–338.45 mbsf). This event is considered diachronous (Raffi et al., 1993; Wei, 1993). However, the occurrence of *H. sellii* at this site is consistent with the ages provided by Raffi

et al. (2006) for the Mediterranean Sea when compared with other calibrated events.

The FO of large *Gephyrocapsa* spp. ($>5.5\text{ }\mu\text{m}$) (1.61 Ma) was identified between Samples 339-U1391C-7R-CC and 8R-CC (391.49–399.92). The LO of *Calcidiscus macintyreui* (1.66 Ma) was placed between Samples 8R-CC and 9R-CC (399.92–412.14 mbsf).

The genus *Discoaster* is rare in Hole U1391C, however, it is possible to recognize some bioevents. The LO of *Discoaster brouweri* (1.95 Ma), defining the boundary of Zones NN18 and NN19, occurs between Samples 339-U1391C-15R-CC and 16R-CC (470.36–478.52 mbsf).

The LO of *Discoaster surculus* (2.53 Ma) is an event useful to approximate the Pleistocene/Pliocene boundary. This bioevent was identified between Samples 339-U1391C-24R-CC and 25R-CC (556.62–566.10 mbsf). The LO of *Discoaster tamalis* (2.8 Ma), another species with low abundance at this site, was placed between Samples 28R-CC and 30R-CC (594.85–613.97 mbsf). These events should be taken with caution because of the scarcity of the species used for its definition.

Planktonic foraminifers

Planktonic foraminifers were studied in all core catcher samples from Holes U1391A–U1391C. Planktonic foraminifers are abundant and well preserved in most samples (Table T6).

Planktonic foraminifer assemblages dominated by *Neogloboquadrina pachyderma* (sinistral), *Turborotalita quinqueloba*, and *Globigerina bulloides*, typically living in polar to subpolar waters today, are replaced by those dominated by *Globigerinoides ruber*, including the pink morphotype, *Globigerinoides trilobus*, and *Globigerinoides sacculifer*, which are characteristic of warmer waters prevalent during interglacial or interstadial periods. Sample 339-U1391A-1H-CC, taken at 4.16 mbsf, contains abundant *N. pachyderma* (sinistral), and therefore we relate it to a Heinrich event, very likely Heinrich Event 1, constraining the depth of the Holocene to the upper part of Core 339-U1391A-1H. In many samples, especially in glacial periods, *G. bulloides* is very abundant, indicating high productivity conditions. Deep-dwelling foraminifers, typically *Globorotalia truncatulinoides* and/or *Globorotalia crassaformis*, were observed in many samples, especially in interglacial periods (Table T6). No evidently reworked foraminifers were found at this site.

In Holes U1391A and U1391B, only one biostratigraphic event, the top of the paracme of *N. pachyderma* (sinistral), has been observed. This event, de-



fined by the reappearance of the species in marine isotope stage (MIS) 36 (1.21 Ma; Lourens et al., 2004; Raymo et al., 1989; Sierro et al., 2009) (Table T6), was observed between Samples 339-U1391A-35X-CC and 36X-CC (324.44–334.10 mbsf) and between 339-U1391B-34X-CC and 35X-CC (318.90–328.74 mbsf). Large, heavily encrusted specimens of *Neogloboquadrina atlantica* (dextral) have been observed in other sites of this expedition occurring at ~1.3 Ma, always within the paracme of *N. pachyderma* (sinistral). In Holes U1391A and U1391B, such specimens are missing, indicating that the bases of these holes are probably younger than 1.3 Ma. However, this event was observed in Hole U1391C between Samples 339-U1391C-5R-CC and 15R-CC (374.53–470.36 mbsf).

The FO of *Globorotalia inflata*, (2.09 Ma; Lourens et al., 2004), was placed between Samples 339-U1391C-18R-CC and 19R-7, 0–5 cm (498.75–507.95 mbsf) (Table T4).

For the first time during this expedition, the LO of *N. atlantica* (sinistral) (2.41 Ma; Weaver and Clement, 1987) was observed between Samples 339-U1391C-23R-CC and 24R-CC (546.94–556.62 mbsf).

The LO of *Globorotalia puncticulata* (2.41 Ma; Hilgen, 1991; Lourens et al., 2004), was observed between Samples 339-U1391C-24R-CC and 25R-CC (556.62–566.10 mbsf).

The coiling change in *G. crassaformis* from sinistral to dextral (2.99 Ma; Zachariasse et al., 1989; Berggren et al., 1995; Lourens et al., 2004; L. Lourens, pers. comm., 2012) that was also observed at Site U1389 (see “[Biostratigraphy](#)” in the “Site U1389” chapter [Expedition 339 Scientists, 2013e]) was placed between Samples 339-U1391C-28R-CC and 30R-CC (594.85–613.97 mbsf) (Table T4).

The LO of *Sphaeroidinellopsis seminulina* (3.19 Ma; Lourens et al., 2004) was found between Samples 339-U1391C-33R-5, 32–34 cm, and 33R-6 (639.55–641.6 mbsf), occurring, as in the Mediterranean and at Site U1389, during an interval of dextral coiling *G. crassaformis* (Zachariasse et al., 1989). The LO occurs below the dolostone (see “[Lithostratigraphy](#)”), confirming the basal age obtained for the dolostone and associated hiatus at Site U1387. The age of this event is well constrained (Lourens et al., 2004), and its offset from the general sedimentation rate line in Figure F18 points to a potentially lower sedimentation rate between the coiling change in *G. crassaformis* at 2.99 Ma and the LO of *S. seminulina* at 3.19 Ma.

The top of the temporal disappearance of *G. puncticulata* (3.31 Ma; Lourens et al., 2004) was recorded between Samples 339-U1391C-34R-CC and 36R-CC (652.11–670.98 mbsf) and constrains the base age of Hole U1391C.

Benthic foraminifers

A total of 28 samples between Sections 339-U1391A-1H-CC and 38X-CC and 20 samples between Sections 339-U1391C-2R-CC and 36R-CC were analyzed for benthic foraminiferal assemblages (Table T7). Benthic foraminifers are well preserved and abundant.

The benthic foraminiferal fauna is mainly composed of species of *Brizalina*, *Bulimina*, *Cassidulina*, *Cibicides*, *Globobulimina*, *Melonis*, *Siphonodosaria*, *Sphaeroidina*, and *Uvigerina* in varying proportions. Based on major fluctuations in *Brizalina* spp., *Cibicides/Cibicidoides* spp., and *Siphonodaria* spp., three assemblages can be distinguished that suggest variations in upwelling intensity, ventilation, and/or MOW current strength and that alternate throughout the succession:

1. Assemblages with high amounts of *Brizalina* spp. characterize environments with increased organic matter flux and reduced ventilation and are most likely linked to intensified upwelling along the Western Iberian margin (Samples 339-U1391A-1H-CC through 16H-CC, 339-U1391C-7R-CC through 14R-CC, and 27R-CC through 33R-CC) (van Morkhoven et al., 1986; Leckie and Olson, 2003; Murray, 2006).
2. Assemblages with high abundances of *Cibicides/Cibicidoides* spp. that parallel low abundances of *Brizalina* spp. indicate improved bottom water oxygenation and increased ventilation (Samples 339-U1391A-18H-CC through 34X-CC and 339-U1391C-36R-CC) (Kaiho, 1999; Murray, 2006).
3. Assemblages between Samples 339-U1391A-35X-CC and 38X-CC and 339-U1391C-2R-CC through 6R-CC reveal high abundances of *Siphonodosaria* spp. associated with variable amounts of *Cibicidoides* cf. *wuellerstorfi*, *Melonis* spp., *Sigmoilopsis schlumbergeri*, and *Uvigerina* spp. The faunal composition indicates high organic matter input with variable oxygen conditions (Kaiho, 1999; Kawagata et al., 2005; Murray, 2006). It is worthy to note that these assemblages show similarities to the lower part of Site U1385 (Samples 339-U1385A-12X-CC through 17X-CC; see Table T7 in the “Site U1385 chapter [Expedition 339 Scientists, 2013c]), which has high abundances of stiliostomellids, nodosariids, and pleurostomellids in general and regular occurrences of *Mylostomella fijiensis* and *Siphonodosaria lepidula* in particular. The latter species are rare or absent at Sites U1386–U1390 in the Gulf of Cádiz.

The “epibenthos group,” which has been suggested as an indicator for MOW intensity in the area (Schönfeld, 1997, 2002; Schönfeld and Zahn, 2000),



is generally rare at Site U1391, potentially resulting from the location in a distal portion of MOW.

The “*Stilostomella* extinction” event (0.58–0.7 Ma; Hayward, 2002; Kawagata et al., 2005) was placed between Samples 339-U1391A-21X-CC and 22X-CC (189.27–199.40 mbsf) based on the last common occurrence of stilostomellids, nodosariids, and pleurostomellids. However, individual shells occur in Samples 20X-CC and 19X-CC. This datum agrees well with the age constraints by the nannoplankton assemblages.

Palynology

Eight samples, six from Hole U1391A (Samples 1H-CC, 7H-CC, 14H-CC, 21X-CC, 28X-CC, and 35X-CC) and two from Hole U1391C (Samples 5R-CC and 15R-CC), were analyzed (Table T8).

A problem in the sample preparation could account for the high concentration value, 170,000 grains/cm³, found in Sample 339-U1391A-35X-CC. The sample is characterized by very fine clay, the dominance of semidesert plants, and one of the first occurrences of *N. pachyderma* (sinistral), can be assigned to MIS 36 or 34 (see above). This sample had to be sieved several times through the 10 µm sieve in order to concentrate the pollen grains. This methodology could have biased the known concentration of *Lycopodium* spores. However, the same protocol has been applied to proximate and similarly very fine clay Samples 339-U1391C-5R-CC and 15R-CC, which in contrast show similar concentration values to the other samples from this site. Therefore, other reasons that may relate to particular environmental and geomorphological conditions of one of these early Quaternary glacial periods in this region could explain the high pollen concentration of Sample 339-U1391A-35X-CC.

Besides that, the very low resolution pollen record reflects (Fig. F19), as at the previous sites (see “**Biostratigraphy**” in the “Site U1385” chapter and “**Biostratigraphy**” in the “Site U1390” chapter [Expedition 339 Scientists, 2013c, 2013f]), the alternating dominance of the four main plant ecological groups which characterize this region, *Pinus*, Mediterranean forest, semidesert, and grasslands, during the last 1.5 m.y. In particular, the high abundance of semidesert plants in the uppermost sample (339-U1391A-1H-CC) at the expense of the Mediterranean forest, heathlands, and grasslands allows us to assign this level to one of the most recent Heinrich stadials, as identified in the nearby Core SU81-18 (Turon et al., 2003).

Paleomagnetism

Paleomagnetic investigation of the 112 APC, XCB, and RCB cores (excluding 1 wash core and 4 cores without recovery) collected at Site U1391 included the measurement of magnetic susceptibility of whole-core and archive-half split-core sections and natural remanent magnetization (NRM) of archive-half split-core sections before and after alternating field (AF) demagnetization with 20 mT peak field. NRM before demagnetization was measured on Cores 339-U1391A-1H through 38X and 339-U1391B-1H through 24X but was discontinued because of time constraints at the end of the expedition. The FlexIt tool was used to orient 32 cores in the APC sections of Holes U1391A and U1391B, starting with Core 4H in Hole U1391A and 3H in Hole U1391B. The APC core orientations for Holes U1391B and U1391C are provided in Table T9 and used for APC core reorientation (Fig. F20). We processed data extracted from the Laboratory Information Management System database by removing all measurements that were made within intervals with interstitial water samples, intervals that contain voids as summarized in the core descriptions, anomalous intervals noted during measurement, and 10 cm of the section ends, which are slightly biased by measurement edge effects. The processed NRM inclination, declination (including the FlexIt tool corrected declination for Holes U1391A and U1391B), and intensity data after 20 mT peak field AF demagnetization are listed in Tables T10, T11, and T12.

Natural remanent magnetization and magnetic susceptibility

The intensity of NRM after 20 mT peak field AF demagnetization is similar in magnitude in the overlapping parts of Holes U1391A–U1391C, ranging from ~10⁻⁵ to ~10⁻² A/m (Fig. F20, third panel). Sediments from the uppermost ~105 mbsf exhibits the highest NRM intensities, on the order of 10⁻² A/m, with a mean of ~0.014 A/m. Below ~105 mbsf, magnetic intensities are variable but generally lower than those in the uppermost part of the section (mean value = ~0.0024 A/m).

Despite the coring disturbance and drill string overprint in the XCB-cored sections, a relatively stable magnetic component was preserved in sediment from all holes, allowing for the determination of magnetic polarity for most parts of the recovered sedimentary sequences. The XCB sections in Holes U1391A and U1391B are often heavily bisected and



frequently contain as much of the disturbed matrix as the intact material, severely compromising the quality of the resulting paleomagnetic data.

Magnetic susceptibility measurements were made on whole cores from all three holes as part of the Whole-Round Multisensor Logger (WRMSL) analysis and on archive-half split-core sections using the Section Half Multisensor Logger (SHMSL) (see “[Physical properties](#)”). Magnetic susceptibility is consistent between the two instruments and, in general, parallels the intensity of magnetic remanence. WRMSL susceptibility was stored in the database in raw meter units. These were multiplied by a factor of 0.68×10^{-5} to convert to the dimensionless volume SI unit (Blum, 1997). A factor of $(67/80) \times 10^{-5}$ was multiplied by the SHMSL acquired susceptibility stored in the database. Magnetic susceptibility varies between 5×10^{-5} and 40×10^{-5} SI (Fig. [F20](#), fourth panel). Susceptibility in the uppermost ~105 m of sediments (mean value is $\sim 20 \times 10^{-5}$ SI) is higher than that of sediments below that level (mean value = $\sim 10 \times 10^{-5}$ SI). Note that in Figure [F20](#), a constant of 25×10^{-5} SI was added to the SHMSL measurements (gray lines) to facilitate the comparison with the WRMSL measurements (black lines).

Magnetostratigraphy

We used magnetic inclinations, and FlexIt tool corrected declinations when available, to interpret magnetostratigraphy for the APC-cored sediment sequences. The lack of core orientation and significant coring disturbance, as well as drill string overprint in the XCB and RCB cores, limit our magnetostratigraphic interpretation for the XCB- and RCB-cored sediments in Holes U1391A and U1391B to relying on magnetic inclination changes. The geomagnetic field at the latitude of Site U1391 (37.56°N) has an expected inclination of 56.78° , assuming a geocentric axial dipole field model, which is sufficiently steep to determine magnetic polarity in cores that lack horizontal orientation.

NRM inclination data (after 20 mT peak field AF demagnetization) from all three holes indicate that the uppermost ~170 m of sediment was deposited during the Brunhes Chron (C1n) (Fig. [F20](#)). This interpretation is consistent with the LO of *P. lacunosa* (0.47 Ma) at ~114.68 and ~118.75 mbsf and the LO of *R. asanoi* (0.9 Ma) at 229.28 and ~235.87 mbsf in Holes U1391A and U1391B, respectively (see “[Biostratigraphy](#)”). The remainder of the XCB sections in Holes U1391A and U1391B is heavily disturbed and overprinted, and although several intervals reveal a clear reversed or normal polarity pattern, it is impossible to assign them to parts of the geomagnetic polarity

timescale without the analysis of discrete samples from the XCB biscuits.

The top of the RCB-cored section of Hole U1391C records the lower part of the Matuyama Chron (C1r.2r) and, surprisingly well, the top (~452–463 mbsf) and bottom (~486 mbsf) of the Olduvai Subchron (C2n). This interpretation is constrained by the LOs of *C. macintyreii* (1.66 Ma) and *D. broweri* (1.95 Ma) at ~406 and 474 mbsf, respectively (see “[Biostratigraphy](#)”). The long normal polarity interval between ~575 mbsf and the base of Hole U1391C is assigned to the Gauss normal chron. This interpretation is supported by the LO of *D. surculus* (2.53 Ma) at ~561 mbsf and the LO of *D. tamalis* (2.80 Ma) at ~604 mbsf. Shorter subchrons of the geomagnetic polarity timescale, such as the Reunion or the Kaena, could not be resolved. The resolved polarity boundaries at Site U1391 are summarized in Table [T13](#).

Physical properties

The shipboard physical properties program at Site U1391 included high-resolution nondestructive measurements of gamma ray attenuation (GRA) bulk density, magnetic susceptibility, and *P*-wave velocity mostly in 2.5 cm steps on the WRMSL. NGR on whole-round core sections was measured at 10 and 20 cm spacing, depending on the time available. The Special Task Multisensor Logger was only used in Hole U1391B for stratigraphic correlation purposes. Thermal conductivity was obtained on Section 3 of each core in Hole U1391A until Core 19H. Discrete measurements of *P*-wave velocities were determined on working-half sections, one every other section in Hole U1391A. However, reasonable results were only obtained for the upper 50 mbsf. Moisture and density (MAD) samples were measured for every second section of each core in Holes U1391A and U1391C. Color reflectance spectrometry and split-core point-logger magnetic susceptibility were obtained for every section in each hole in 5 cm steps.

Based on the physical property data, we can distinguish four units (Figs. [F21](#), [F22](#)). Physical properties Unit I, from 0 to ~155 mbsf, is characterized by a clear positive correlation between NGR, magnetic susceptibility, and a^* . The color reflectance measurement a^* is generally very variable and includes positive (reddish) values. Physical properties Unit II, between ~155 and 200 mbsf, is characterized by low magnetic susceptibility and a marked negative correlation between NGR and a^* . Physical properties Unit III, from 200 to 560 mbsf, exhibits low magnetic susceptibility values and a positive correlation between NGR, magnetic susceptibility, and GRA density. The correlation between magnetic susceptibility and



NGR is particularly pronounced. Conversely, color reflectance measurements (L^* and a^*) show a positive correlation in several peaks but a complex, unclear relationship when compared with NGR. Below 200 mbsf, a^* values are less variable and exclusively negative. Physical properties Unit IV can be recognized in Hole U1391C downhole from 560 mbsf as a marked reduction in NGR variability and magnetic susceptibility values.

Coinciding with the major change in physical properties at ~200 mbsf is the boundary between lithostratigraphic Units I and II, which is characterized by more abundant sandy intervals above 200 mbsf (see “[Lithostratigraphy](#)”). The color reflectance data is further in agreement with the visual core descriptions, which indicate that alternations of greenish and reddish intervals are only present above ~170 mbsf, whereas reddish intervals disappear below 200 mbsf.

Whole-Round Multisensor Logger measurements

GRA bulk density and magnetic susceptibility were measured using the WRMSL in all core sections at 2.5 cm intervals at Site U1391 after core acclimation for 3 h (Fig. F21).

Gamma ray attenuation bulk density

Measured GRA density at Site U1391 ranges between 1.4 and 2.1 g/cm³ and displays a steady increase in the upper 20 mbsf, probably caused by early diagenetic compaction. Downhole, we observed cyclic variations with average values around 1.85 to 1.9 g/cm³ and distinctive, low-GRA density intervals at 90, 108, 165, and 255 mbsf (Fig. F21A). In Hole U1391C, GRA density reaches a maximum value of 2.4 g/cm³ at 632 mbsf related to the presence of a dolomitic mudstone (see “[Lithostratigraphy](#)”) (Fig. F21B).

When GRA density is compared to lithology, no clear correlation can be found. Compared with the other physical properties, a similarity to magnetic susceptibility is present, although it is not as pronounced as observed for the other sites within the Gulf of Cádiz (e.g., Site U1389). In physical properties Unit III, from 200 to 560 mbsf, a moderately strong positive correlation can be found between GRA density and NGR.

Magnetic susceptibility

The most notable aspects of the magnetic susceptibility records in Hole U1391A are a sharp decrease at 28 mbsf (from 65×10^{-5} SI to $\sim 10 \times 10^{-5}$ SI) and cyclic

variations ranging from 5×10^{-5} to 60×10^{-5} SI between 28 mbsf and the lower boundary of physical properties Unit I. Generally, low values are found in physical properties Units II and III (mostly $<20 \times 10^{-5}$ SI), and a further decrease can be observed in physical properties Unit IV, with values usually $<10 \times 10^{-5}$ SI downhole (Fig. F21).

Magnetic susceptibility records at Site U1391 show a clear positive correlation with NGR data. This relationship becomes remarkably good below ~155 mbsf. In physical properties Unit I (0–155 mbsf), magnetic susceptibility is sensitive to the presence of sands, although with a complex pattern. For example, sandy layers in Sections 339-U1391A-6H-4 and 6H-6 exhibit low magnetic susceptibility in their lower parts and an abrupt shift to high values in the upper parts. Sharp compositional changes are described within these two sandy layers (see “[Lithostratigraphy](#)”). However, no correlation of magnetic properties can be found in relation to sand layers in the other physical properties units (e.g., sand layers in Cores 339-U1391A-22X and 30X).

Low magnetic susceptibility values through physical properties Units II, III, and IV could be explained by the reduction of fine-grained magnetite to Fe sulfides below the sulfate reduction zone. However, the present sulfate–methane transition zone occurs at a shallower depth of ~20 mbsf (see “[Geochemistry](#)”). A link between magnetic susceptibility and diagenetic processes could occur in physical properties Unit IV, where the decrease in magnetic susceptibility might relate to a large increase in alkalinity and the inferred presence of gas hydrate at roughly the same depth.

P-wave velocity

Sonic velocities were measured with the WRMSL in Hole U1391A, and an attempt was made to determine P-wave velocities on split cores in each section of Hole U1391A (Fig. F21A). Because of poor sediment to liner coupling, reasonable results from the WRMSL could only be obtained for the upper ~45 mbsf. The P-wave velocity profile can be extended downhole to 50 mbsf by using the P-wave measurements on split cores. Although the sediment surface appeared to be smooth and should have provided an adequate coupling to the transducers, no clear acoustic signal could be obtained at greater depths. An explanation for this might be the formation of small cracks in the relatively stiff and brittle sediment that negatively affects signal propagation through the sediment. Additionally, small voids between sediment and liner might prevent a sharp signal from being received by the transducer touching the liner.



P-wave velocities follow the trend of increasing GRA density in the upper 10 mbsf. Downhole values range from 1400 to 1650 m/s for WRMSL and split-core data (only accounting for automatically processed data). Values obtained by both types of measurements agree well, especially when only considering split-core data with high signal quality (solid symbols in Fig. F21A).

Natural gamma radiation

Measured values of NGR range from 20 to 55 cps, revealing cyclic patterns that are more abrupt than regular oscillations in physical properties Units I, II, and III (Fig. F22). In physical properties Unit IV, NGR decreases in variability between 30 and 45 cps and lacks distinct peaks (Fig. F22B).

NGR data do not show a clear correlation with grain size variations, which might indicate that detrital potassium and thorium are present independent of grain size variations. Notably, an almost perfect correlation exists between NGR and magnetic susceptibility, and a negative correlation with exists a^* in physical properties Unit II.

Moisture and density measurements

Determination of moisture content and density on discrete sediment samples was made on every second section of Hole U1391A (Fig. F23). Samples were consistently taken at ~60 cm intervals. Generally, GRA and MAD methods give consistent density results, with slightly lower values for MAD in the upper ~20 mbsf of Hole U1391A (Fig. F23A).

The compaction-related downhole moisture and porosity decrease follows a characteristic pattern. Rapid compaction can be recognized in the upper 2 mbsf, with a decrease in porosity from 70% to 60% and moisture content from 40% to 30%. More progressive compaction occurs from 2 to ~30 mbsf, where values reach 30% moisture and 55% porosity. This variation in compaction mode can be related to the different sediment composition and texture and might be a result of changes in the sedimentation rate. Below 30 mbsf in physical properties Unit I, we observed two long-wavelength cyclic variations between 25% and 30% in moisture content and 45% and 55% in porosity. Grain density shows an inverse correlation with these cyclic changes, which might indicate that these cycles are controlled by carbonate content.

In physical properties Unit II (155–200 mbsf), two peaks in porosity and moisture content can be recognized. The previously recognized anticorrelation to grain density appear to be more complex in this unit. Throughout physical properties Unit PPIII,

high-amplitude cyclicity appears to be superimposed upon other low- and high- amplitude oscillations. Grain density values are highly variable from 420 mbsf to the lowermost core, with sharp variations between 2.85 and 2.65 g/cm³. This interval is characterized by a slightly increased abundance of sandy intervals, which might explain the larger scatter of the grain density data. Data below 500 mbsf are not available because of time constraints at the end of the expedition.

Thermal conductivity

Thermal conductivity was measured once per core using the full-space probe, usually in Section 3 near the middle of sections downhole to Core 339-U1391A-19H (see “Downhole measurements”). Because cores retrieved using XCB drilling are severely disturbed and affected by biscuiting, thermal conductivity measurements were only taken on APC cores. Thermal conductivity varies between 1.1 and 1.6 W/(m·K), which is in the range observed at the other sites. In the upper 30 mbsf, thermal conductivity values show a low range of variation (1.1–1.3 W/[m·K]). Below 30 mbsf, no clear trend is imprinted in the data; however, more prominent variations appear between cores that reach the highest and lowest values. A weak correlation to moisture content and porosity can be recognized between Cores 339-U1391A-4H and 9H, in which relatively high moisture and porosity values appear to correlate with high thermal conductivity values. For the other cores, the relationship between thermal conductivity and other parameters is not evident, although pore water content should have an effect on thermal conductivity.

Summary of main results

Correlation of physical property data allows us to discern four physical properties units at Site U1391 with boundaries at 155, 200, and 560 mbsf. The boundary at 200 mbsf matches with a change in the abundance of sandy beds in the mud-dominated sediment (lithostratigraphic Units I and II). In general, a coherent relationship exists between high magnetic susceptibility, NGR, and GRA density. Especially notable is the excellent correlation between NGR and magnetic susceptibility below ~155 mbsf. The presence of coarse layers is, if at all, inconsistently expressed in the measured physical parameters. However, major changes in physical properties are evident in apparently homogeneous calcareous mud deposits. The varying (i.e., positive as well as negative) correlation of NGR and magnetic susceptibility in relation to color changes suggests that the associated changes in mineralogical composition are of a

different nature in this location when compared with previous reddish layers described during this expedition.

Geochemistry

Volatile hydrocarbons

Headspace gas analysis was performed as a part of the standard protocol required for shipboard safety and pollution prevention monitoring. In total, 34 headspace samples from Hole U1391A (sampling resolution of one per core) and 32 samples from Hole U1391C were analyzed (Fig. F24; Table T14), spanning the entire depth range of the site. In both Holes U1391A and U1391C, we detected methane (C_1), ethane (C_2), ethene ($C_{2=}$), propane (C_3), and propene ($C_{3=}$). Methane ranges from 5.4 ppmv near the surface to a maximum of 41,703 ppmv at 69.9 mbsf (Section 339-U1391A-8H-7). Below this depth, methane displays a decreasing trend, reaching 1,276 ppmv at the base of Hole U1391C. Ethane, ethene, propane, and propene were all detected in both holes, but concentrations remained low. All C_2 and C_3 hydrocarbons do not exceed 8 ppmv for the entire depth profile. Ethane does not exceed 7.1 ppmv, ethene does not exceed 2.6 ppmv, propene does not exceed 0.6 ppmv, and propane does not exceed 4.8 ppmv.

Sedimentary geochemistry

Sediment samples were collected for analysis of solid-phase geochemistry (inorganic and organic carbon) at a resolution of approximately one sample per core in Hole U1391A (Table T15); however, because of time constraints at this final site of the expedition, we could not analyze samples below 351 mbsf. $CaCO_3$ varies from 17.5 to 45.2 wt% (Fig. F25). The range is comparable, albeit greater, than the $CaCO_3$ variability measured at nearby Site U1385. Organic carbon varies between 0.5 and 1.8 wt% (Fig. F26A), with no discernible trends at this resolution.

Nitrogen (Fig. F26B) was measured downhole to 351 mbsf in Hole U1391A and ranges from 0.06 to 0.1 wt%. We did not observe any notable trends in nitrogen content with depth. The C/N ratio, used to distinguish the origin of organic matter (marine versus terrestrial) in sediment, varies between 7 and 22, indicating that the organic carbon is mainly of marine origin with a terrestrial component of varying contribution (Fig. F26C). Samples with a C/N ratio exceeding 10 indicate the presence of some terrestrial input, whereas those over 20 are predominantly terrestrial (Emerson and Hedges, 1988; Meyers, 1997).

The terrestrial component calculated at Site U1391 is greater than that measured at Site U1385, which is expected given the closer proximity of Site U1391 to land. Total organic carbon and C/N ratios are positively correlated, which agrees with the relationships observed at Sites U1385–U1388 and Site U1390 but is in contrast with the relationship between total organic carbon and C/N at Site U1389.

Interstitial water chemistry

Major cations and anions

Sulfate concentrations are near seawater values at the top of the section and decrease to zero at ~20 mbsf (Fig. F27A; Table T16). At 407.5 and 482.55 mbsf, a small amount of sulfate (<1 mM) was detected, which is likely due to sample contamination from drilling fluid.

Ammonium concentrations increase from 467 μM at the surface to ~7,000 μM at 204 mbsf (Fig. F27B). Ammonium values remain roughly constant between 204 and 480 mbsf, after which they increase to a maximum of near 11,200 μM at 649 mbsf.

Alkalinity increases from 8.2 meq/L near the seafloor to peak values of 15.2 meq/L at 13 mbsf and decreases to 6 meq/L at 42 mbsf (Fig. F27C). Alkalinity remains low downhole to 100 mbsf, where it increases again to 10 meq/L at ~150 mbsf. Missing alkalinity data between 168 and 223 mbsf is the result of an electrode malfunction. Downhole from ~400 mbsf, alkalinity begins to rise markedly, reaching values as high as 39.5 meq/L at 592 mbsf.

Calcium, magnesium, and potassium display similar patterns in the upper part of Hole U1391A. All show a sharp decrease from seawater values near the seafloor to lower values between 22 and 32 mbsf. Calcium concentrations decrease from 8.6 mM near the seafloor to a minimum of 2.9 mM at 22 mbsf (Fig. F28A). Magnesium concentration is 52 mM at the seafloor and decreases to 32 mM at 33 mbsf (Fig. F28B). Potassium concentration is 12 mM at the seafloor and decreases to 8.6 mM by 33 mbsf (Fig. F28C). Between 33 and 460 mbsf, potassium and magnesium continue to decrease, reaching values of 6.22 and 23.93 mM, respectively, at 460 mbsf. From 460 mbsf to the base of Hole U1391C, potassium and magnesium increase to 10.44 and 33.5 mM, respectively. Calcium concentrations increase in a step-wise pattern from 22 to 241 mbsf. Between 241 and 396 mbsf, calcium varies between 6.7 and 7.8 mM. At 396 mbsf, calcium begins to decrease and reaches a minimum value of 2.66 mM at 552 mbsf. At 552 mbsf, calcium increases again to 7 mM at 620 mbsf and decreases slightly to reach ~6 mM at the base of Hole U1391C.

Chloride concentrations are 580 mM at the seafloor and decrease downhole, reaching minimum values of ~545 mM near the base of the site (Fig. F29A). Chloride decreases rapidly from the seafloor to ~70 mbsf, after which it continues to decline but at a slower rate.

Sodium at Site U1391 shows very high variability, ranging from 460 to 523 mM (Fig. F29B). This rapidly fluctuating signal is unlikely to be real, as it is not observed in any of the other profiles. With this in mind, the variation of Na/Cl ratios away from the seawater value of 0.86 (Fig. F29C) is probably largely a function of error in measurement of the sodium concentrations.

Minor elements

Barium (Fig. F30A) increases from the seafloor to the base of Site U1391. Sharp increases in barium concentration of about 30 μM are apparent between the seafloor and 22 mbsf and between 582 and 592 mbsf.

Boron decreases rapidly from ~500 μM at the seafloor to 257 μM at 146 mbsf (Fig. F30B). The concentration then varies between 208 and 283 μM down-hole to 533 mbsf. From 533 to 552 mbsf, boron decreases sharply to 185 μM and increases to 284 μM at 563 mbsf, after which it decreases slightly to the base of Hole U1391C.

Iron concentration at Site U1391 decreases sharply from 37 to 1.6 μM between the seafloor and 42 mbsf (Fig. F30C). Several sharp increases in iron between 42 mbsf and the base of the hole that are as large as 19 μM are evident, but in general, below 42 mbsf the concentration remains close to our detection limit.

Lithium concentrations are <3 μM throughout Site U1391, which is very close to the detection limit (Fig. F31A).

Silicon varies but generally increases from a seafloor value of 320 μM to a maximum of 1020 μM at 620 mbsf (Fig. F31B). Silicon increases rapidly between 552 and 620 mbsf to ~700 μM .

Strontium increases smoothly from a seafloor value of 76 to 131 μM at 533 mbsf (Fig. F31C). The concentration decreases to 110 μM at 553 mbsf and rapidly increases to the base of the site, reaching a maximum of 184 μM .

Stable isotopes

Water isotopes were measured only in the upper 200 m of Site U1391 because of time constraints imposed by the end of the expedition (Table T17). At the seafloor, oxygen and hydrogen isotopes are ~0.9‰ and 3.8‰, respectively, reflecting the lower branch of

MOW. $\delta^{18}\text{O}$ oscillates around a mean value of 0.9‰ in the upper 50 mbsf and decreases to a minimum of 0.3‰ at 59.3 mbsf, followed by an increase between 60 and 89 mbsf to ~1.5‰. Below 89 mbsf, $\delta^{18}\text{O}$ decreases, reaching 0.8‰ at 127 mbsf and remaining near this value to 187 mbsf. The deepest sample, measured at 194 mbsf, has an even lower value of 0.4‰.

δD increases from 3.8‰ at the sediment/water interface to 8.7‰ at ~42 mbsf. A distinct minimum in δD occurs at 59.3 mbsf, reaching values as low as 1.5‰, and followed by an increase in values averaging 5.7‰ between 70 and 200 mbsf. The $\delta^{18}\text{O}$ and δD minimum at 59.3 mbsf was replicated by measuring the sample twice. Oxygen and hydrogen isotopes are positively correlated in the upper 115 mbsf (Figs. F32, F33).

Summary

It is useful to compare the interstitial water results from Site U1391 with those from Site U1385 because the former is influenced by the lower branch of MOW, whereas the latter reflects Northeast Atlantic Deep Water. The sulfate reduction zone is shallower at Site U1391 (20 mbsf) than at Site U1385 (50 mbsf), perhaps reflecting the higher sedimentation rate and accumulation rate of organic matter at Site U1391.

The rapid decrease in chloride in the uppermost 100 mbsf at Site U1391 is similar to the trend at Site U1386, which is located in the upper branch of MOW. Both sites are within MOW, but Site U1391 is in the lower branch.

The decrease of calcium and magnesium in the sulfate reduction zone reflects dolomite formation as a result of high alkalinity produced by sulfate reduction and anaerobic methane oxidation. The increase in calcium and decrease in magnesium below this level may reflect dolomitization of calcite that involves replacement of half the Ca^{2+} ions by Mg^{2+} , thereby resulting in removal of magnesium and addition of calcium to interstitial water.

Alkalinity values as high as 40 meq/L are found near the base of Hole U1391C. If the alkalinity is due to dissolved carbonate, this high value may be related to in situ water-solid equilibrium with the dolomite layer found at the base of the hole (see “[Lithostратigraphy](#)”). Correspondingly, high carbonate concentrations would enable the in situ precipitation of dolomite from solution.

The organic geochemistry analysis shows similar trends and values at Sites U1385 and U1391. The CaCO_3 values observed at this site is comparable to CaCO_3 values at Site U1385, albeit with a greater range at Site U1391. Both sites exhibit a strong posi-



tive correlation between total organic carbon and C/N ratios; Site U1391 has a greater organic contribution from terrestrial matter compared to Site U1385, which can be explained by its closer proximity to land.

Downhole measurements

Logging operations

After the last core from Hole U1391C arrived on deck, the hole was prepared for logging. Following a wiper trip, the hole was flushed with sepiolite mud and displaced with 248 bbl of barite-weighted heavy mud (10.5 ppg). The pipe was set at 98.9 mbsf. Two tool strings were deployed in Hole U1391C, the triple combo and FMS-sonic (Fig. F34; see also “[Downhole measurements](#)” and Table T6 in the “Methods” chapter [Expedition 339 Scientists, 2013b] for tool acronym definitions).

The triple combo tool string started downhole at 0335 h on 15 January 2012. The Hostile Environment Natural Gamma Ray Sonde (HNGS), High-Resolution Laterolog Array (HRLA), and Hostile Environment Litho-Density Sonde (HLDS) were included. The Accelerator Porosity Sonde was omitted because it allowed the HNGS to be placed at the bottom of the tool string to record to the base of the hole. The tool string reached the base of the hole at 668 mbsf, and the main pass was logged up to seafloor. FMS-sonic tool string rig-up started at 0920 h, and the tool string also reached close to the bottom of the hole at 666 mbsf. The Pass 1 uplog extended to the seafloor, but bridged sections were noted from 317 to 324 and 330 to 334 mbsf. The hole was closing up, so Pass 2 was run up from 314 mbsf.

Maximum ship heave was generally 1 to 1.5 m maximum peak-to-peak, but reached 2 m at times. The tide was high during the triple combo run (+0.7 to +1.2 m) and rising during the FMS-sonic run (-0.8 to +0.7 m) (Fig. F35). The sediments were Pliocene-Pleistocene nannofossil muds and silty muds (see “[Lithostratigraphy](#)”). The wireline heave compensator was used to counter ship heave during logging.

Log data quality

In Hole U1391C, the borehole wall was very rugose, with many narrow washouts often exceeding 18 inches wide, reducing log data quality (Fig. F36). Some caves were found that were generally associated with low values in all the logs, for example, a large washout from 310 to 320 mbsf. Numerous 1–3 m thick narrow bridged sections with diameters <6–8 inches (bit size = 9.875 inches) were also found and were mainly concentrated in the middle section of

the hole, from 245 to 390 mbsf. Of the all the logs, resistivity and sonic velocity were the least sensitive to variable hole diameter, although some reduction in values in the larger washouts is evident. The NGR log anticorrelates strongly with the caliper log. Density was highly affected, giving density values close to water density in washouts (Fig. F36). The photoelectric effect log gave anomalously high values below 390 mbsf, especially at washouts, because of the barite-weighted mud. FMS resistivity images were also dominated by poor contact with the borehole wall in the wide areas, although some intervals of good images are present.

Logging units

The baseline values of the Hole U1391C downhole logs change gradually downhole, with no major steps in the base levels. The entire logged interval was thus assigned to one logging unit (Fig. F36). At the scale of this unit, the NGR signal ranges on average from 30 to 65 gAPI, with peak values reaching 85 gAPI. The signal shows moderately high amplitude variability on a several-meter to submeter scale, and given the sedimentological context (see “[Lithostratigraphy](#)”), is primarily tracking clay content. This interpretation is supported by close correlation of the potassium and thorium logs (Fig. F37). Uranium generally contributes a relatively minor component to the total NGR signal and generally behaves as an independent constituent compared to potassium and thorium because it is not chemically combined in the main rock-forming minerals. The sonic velocity log increases downhole (Fig. F36), reflecting sediment compaction with depth, and generally co-varies with the NGR log. The logging unit is divided into two subunits, mostly on the basis of a relative absence of high NGR values below 562 mbsf and a small step down in the density, resistivity, and sonic velocity logs at this depth (Figs. F36, F37).

Logging Subunit 1A: base of drill pipe to 562 mbsf

Logging Subunit 1A is characterized by medium-amplitude alternations in bulk density, NGR (and its uranium, thorium, and potassium components), density, and sonic velocity values (Fig. F36). Several orders of cycles are observed in the NGR curves, varying from one to several tens of meters in thickness (Fig. F37). Potassium and thorium concentrations co-vary closely, suggesting that clay content controls these logs. The uranium concentrations correlate to potassium and thorium at some depths or vary independently at others. As expected from downhole compaction, the density and sonic velocity logs have an increasing downhole trend and are



generally well correlated. These logs also correlate well with the resistivity curve at a medium scale (several tens of meters). Logging Subunit 1A at Site U1391 resembles logging Subunit 1A observed at Sites U1389 and U1390 (see “[Downhole measurements](#)” in the “Site U1389” chapter [Expedition 339 Scientists, 2013e]).

Logging Subunit 1B: 562–668 mbsf

Subunit 1B is distinguished from the subunit above by the presence of lower NGR values (Figs. [F36](#), [F37](#)). In particular, two intervals with low NGR values are observed from 562 to 582 and 593 to 605 mbsf. These intervals suggest the presence of two several-meter thick sandy intervals that seem to correspond with intervals of low core recovery. A thin layer of high resistivity, high density (reaching 2.52 g/cm³), high velocity, and low NGR values is observed at 631 mbsf (Fig. [F36](#)). This high-resistivity horizon is caused by a well-consolidated dolomite mudstone identified in Core 339-U1391C-29R (see “[Lithostigraphy](#)”).

Heat flow

Ten advanced piston corer temperature tool (APCT-3) downhole temperature measurements in Holes U1391A and U1391B ranged from 11.8°C at 32.0 mbsf to 13.3°C at 145.95 mbsf (Fig. [F38](#); Table [T18](#)), giving a geothermal gradient of 14.2°C/km (Fig. [F39](#)). The measurements increase linearly with depth, and the trend line intersects the seafloor at 11.35°C. Some scatter and minor differences between the two holes is evident. These differences are probably caused by (1) uncertainty in fitting to the APCT-3 temperature equilibration curves to obtain the formation temperature and (2) lateral heterogeneity in heat flow leading to small temperature differences between the holes. Readings at shallower depths have more uncertainty because the APC barrel has more freedom of movement in the hole where the sediment is soft. Unlike at previous sites, the bottom water temperature was repeatably constrained from the APCT-3 temperature profiles (Fig. [F38](#)), both while the APC was held at the mudline (~11.6°C) and the minimum temperature in the profiles (~11.5°C), similar to, but a little higher than the estimate from the intersection of the linear temperature trend with the seafloor.

Thermal conductivity under in situ conditions was estimated from laboratory-determined thermal conductivity using the method of Hyndman et al. (1974) (see “[Physical properties](#)” in the “Methods” chapter [Expedition 339 Scientists, 2013b]). The calculated in situ values average 1.2% below the measured laboratory values. Thermal resistance was

then calculated by integrating the inverse of in situ thermal conductivity over depth (Fig. [F39](#)). A heat flow of 17.5 mW/m² was obtained from the linear fit between temperature and thermal resistance (Pribnow et al., 2000). This value is very low compared to heat flow values for the nearby Marques de Pombal escarpment (Grevemeyer et al., 2009).

Stratigraphic correlation

The meters composite depth (mcd) scale for Site U1391 was based on correlation of magnetic susceptibility and NGR data between Holes U1391A–U1391C. Both Holes U1391A and U1391B were cored to APC refusal, which occurred at ~171 mbsf at the base of Cores 339-U1391A-19H and 339-U1391B-18H, and then XCB cored to ~353 mbsf. Hole U1391C was RCB cored downhole from 340 mbsf, overlapping only the very basal part cored in the other two holes.

The correlation between Holes U1391A and U1391B is relatively straightforward downhole to 169 mcd (base of Core 339-U1391A-16H), except that the correlation of Core 339-U1391A-14H to 339-U1391B-13H is poor because susceptibility and NGR data lack distinctive features across this connection, which spans ~128–131 mcd (Fig. [F40](#)). From 169 mcd downhole to ~310 mcd, susceptibility is very low and has few features that can be correlated with confidence. Hence, NGR data are the primary constraint through this interval and generally provide distinct anomalies that can be correlated to within ~20 cm. An exception to this occurs from ~250 to 262 mcd, where the NGR signal is relatively constant, making correlation between holes very uncertain.

No gaps occur in the stratigraphic section until the base of Cores 339-U1391A-19H and 339-U1391B-18H, where both cores were unable to penetrate deeper than ~171 mbsf (i.e., the APC refusal depth), corresponding to ~196 mcd. Thus, a small gap occurs at this depth. Another small gap occurs at ~243 mcd (between Cores 339-U1391B-23X and 24X) that is not filled by core from Hole U1391A because Core 339-U1391A-24X had no recovery. Other very small gaps (less than ~30 cm) may occur at approximately 272, 283, 292, and 336 mcd.

NGR and susceptibility data for Cores 339-U1391C-2R and 3R correlate well with Cores 339-U1391A-38X and 339-U1391B-37X and 38X and those of Core 339-U1391C-4R with the base of 339-U1391B-38X. Hence, the base of Core 339-U1391C-4R marks the base of the multi-cored interval.

Overall, the three holes cored at Site U1391 provide enough material to produce a composite strati-



graphic section that is complete, with few or no gaps from seafloor downhole to the base of Core 339-U1391C-4R at 417.66 mcd (358 mbsf). The section below this depth is cored only in Hole U1391C downhole to a total depth of 671.5 mbsf, with short gaps inevitably occurring between cores and larger gaps occurring wherever core recovery is low.

The offsets and composite depths are listed in Table T19. A growth factor of 1.144 is calculated by linear regression for the multicored interval in Holes U1391A and U1391B, indicating a 14.4% expansion of mcd values relative to mbsf values (Fig. F41). Because of the very linear nature of the expansion, the mcd scale can readily be compressed by dividing by 1.144 to produce a modified depth scale (mbsf*) that corresponds more closely to true coring depths while retaining the between-hole correlations. This is illustrated for NGR data in Holes U1391A–U1391C in Figure F42. For the single-cored interval, the relative gaps between cores can be estimated by using a similar growth factor (Table T19).

Splice tie points for the composite section are given in Table T20. Spliced records are provided for susceptibility (Table T21) and NGR (Table T22).

References

- Alves, T.M., Gawthorpe, R.L., Hunt, D., and Monteiro, J.H., 2000. Tertiary evolution of the São Vicente and Setúbal submarine canyons, southwest Portugal: insights from seismic stratigraphy. *Cienc. Terra (UNL)*, 14:243–256. <http://hdl.handle.net/10362/4716>
- Alves, T.M., Gawthorpe, R.L., Hunt, D.W., and Monteiro, J.H., 2003. Cenozoic tectono-sedimentary evolution of the western Iberian margin. *Mar. Geol.*, 195(1–4):75–108. doi:10.1016/S0025-3227(02)00683-7
- Bender, V.B., Hanebuth, T.J.J., and Baumann, K.H., 2010. Detrital input, marine productivity, deep water currents, and sea level alternatively influencing sedimentation on the Galician continental margin over the past 30 ka BP. *Geo-Temas*, 11:19–20
- Berggren, W.A., Hilgen, F.J., Langereis, C.G., Kent, D.V., Obradovich, J.D., Raffi, I., Raymo, M.E., and Shackleton, N.J., 1995. Late Neogene chronology: new perspectives in high-resolution stratigraphy. *Geol. Soc. Am. Bull.*, 107(11):1272–1287. doi:10.1130/0016-7606(1995)107<1272:LNCNPI>2.3.CO;2
- Blum, P., 1997. Physical properties handbook: a guide to the shipboard measurement of physical properties of deep-sea cores. *ODP Tech. Note*, 26. doi:10.2973/odp.tn.26.1997
- Egbert, G.D., and Erofeeva, S.Y., 2002. Efficient inverse modeling of barotropic ocean tides. *J. Atmos. Oceanic Technol.*, 19(2):183–204. doi:10.1175/1520-0426(2002)019<0183:EIMOBO>2.0.CO;2
- Emerson, S., and Hedges, J.I., 1988. Processes controlling the organic carbon content of open ocean sediments. *Paleoceanography*, 3(5):621–634. doi:10.1029/PA003i005p00621
- Ercilla, G., Casas, D., Estrada, F., Vázquez, J.T., Iglesias, J., García, M., Gómez, M., Acosta, J., Gallart, J., Maestro-González, A., and the Marconi Team, 2008. Morphosedimentary features and recent depositional architectural model of the Cantabrian continental margin. *Mar. Geol.*, 247(1–2):61–83 doi:10.1016/j.margeo.2007.08.007
- Ercilla, G., Casas, D., Iglesias, J., Vázquez, J.T., Somoza, L., León, R., Medialdea, T., Juan, C., and García, M., 2010. Contourites in the Galicia Bank region (NW Iberian Atlantic). *Geo-Temas*, 11:33–34.
- Ercilla, G., Casas, D., Somoza, L., Vázquez, J.T., Iglesias, J., García-Gil, S., Medialdea, T., León, R., Estrada, F., and the ERGAP Project Cruise Teams, 2009. Cartografiando la dinámica sedimentaria de la región del Banco de Galicia. *Simp. Margen Ibérico Atlántico*, MIA09:201–204. http://digital.csic.es/bitstream/10261/20971/1/MIA09_BANCO.pdf
- Ercilla, G., Casas, D., Vázquez, J.T., Iglesias, J., Somoza, L., Juan, C., Medialdea, T., León, R., Estrada, F., García-Gil, S., Farran, M., Bohoyo, F., Gracia, M., Maestro, A., and the ERGAP Project Cruise Teams, 2011. Imaging the recent sediment dynamics of the Galicia Bank region (Atlantic, NW Iberian Peninsula). *Mar. Geophys. Res.*, 32(1–2):99–126. doi:10.1007/s11001-011-9129-x
- Expedition 339 Scientists, 2013a. Expedition 339 summary. In Stow, D.A.V., Hernández-Molina, F.J., Alvarez Zarikian, C.A., and the Expedition 339 Scientists, *Proc. IODP*, 339: Tokyo (Integrated Ocean Drilling Program Management International, Inc.). doi:10.2204/iodp.proc.339.101.2013
- Expedition 339 Scientists, 2013b. Methods. In Stow, D.A.V., Hernández-Molina, F.J., Alvarez Zarikian, C.A., and the Expedition 339 Scientists, *Proc. IODP*, 339: Tokyo (Integrated Ocean Drilling Program Management International, Inc.). doi:10.2204/iodp.proc.339.102.2013
- Expedition 339 Scientists, 2013c. Site U1385. In Stow, D.A.V., Hernández-Molina, F.J., Alvarez Zarikian, C.A., and the Expedition 339 Scientists, *Proc. IODP*, 339: Tokyo (Integrated Ocean Drilling Program Management International, Inc.). doi:10.2204/iodp.proc.339.103.2013
- Expedition 339 Scientists, 2013d. Site U1387. In Stow, D.A.V., Hernández-Molina, F.J., Alvarez Zarikian, C.A., and the Expedition 339 Scientists, *Proc. IODP*, 339: Tokyo (Integrated Ocean Drilling Program Management International, Inc.). doi:10.2204/iodp.proc.339.105.2013
- Expedition 339 Scientists, 2013e. Site U1389. In Stow, D.A.V., Hernández-Molina, F.J., Alvarez Zarikian, C.A., and the Expedition 339 Scientists, *Proc. IODP*, 339: Tokyo (Integrated Ocean Drilling Program Management International, Inc.). doi:10.2204/iodp.proc.339.107.2013
- Expedition 339 Scientists, 2013f. Site U1390. In Stow, D.A.V., Hernández-Molina, F.J., Alvarez Zarikian, C.A., and the Expedition 339 Scientists, *Proc. IODP*, 339: Tokyo (Integrated Ocean Drilling Program Management



- International, Inc.). doi:[10.2204/iodp.proc.339.108.2013](https://doi.org/10.2204/iodp.proc.339.108.2013)
- Flores, J.-A., Colmenero-Hidalgo, E., Mejía-Molina, A.E., Baumann, K.-H., Hendericks, J., Larsson, K., Prabhu, C.N., Sierro, F.J., and Rodrigues, T., 2010. Distribution of large *Emiliania huxleyi* in the central and northeast Atlantic as a tracer of surface ocean dynamics during the last 25,000 years. *Mar. Micropaleontol.*, 76(3–4):53–66. doi:[10.1016/j.marmicro.2010.05.001](https://doi.org/10.1016/j.marmicro.2010.05.001)
- Grevemeyer, I., Kaul, N., and Kopf, A., 2009. Heat flow anomalies in the Gulf of Cadiz and off Cape San Vincente, Portugal. *Mar. Pet. Geol.*, 26(6):795–804. doi:[10.1016/j.marpetgeo.2008.08.006](https://doi.org/10.1016/j.marpetgeo.2008.08.006)
- Hayward, B.W., 2002. Late Pliocene to middle Pleistocene extinctions of deep-sea benthic foraminifera (“*Stilostomella* extinction”) in the southwest Pacific. *J. Foraminiferal Res.*, 32(3):274–307. doi:[10.2113/32.3.274](https://doi.org/10.2113/32.3.274)
- Hernández-Molina, F.J., Llave, E., Somoza, L., Fernández-Puga, M.C., Maestro, A., León, R., Medialdea, T., Barnolas, A., García, M., Díaz del Río, V., Fernández-Salas, L.M., Vázquez, J.T., Lobo, F., Alveirinho Dias, J.M., Rodero, J., and Gardner, J., 2003. Looking for clues to paleoceanographic imprints: a diagnosis of the Gulf of Cádiz contourite depositional systems. *Geology*, 31(1):19–22. doi:[10.1130/0091-7613\(2003\)031<0019:LFCTPI>2.0.CO;2](https://doi.org/10.1130/0091-7613(2003)031<0019:LFCTPI>2.0.CO;2)
- Hernández-Molina, F.J., Nombela, M.A., Van Rooij, D., Roson, G., Ercilla, G., Urgorri, V., Llave, E., Francés, G., De Mol, L., Estrada, F., León, R., Mena, A., Pérez Arlucea, M., Alejo I., Jane, G., and VanReusel, A., 2009. The Ortegal spur contourite depositional system (Bay of Biscay): the implications of the Mediterranean Outflow Waters in sedimentary processes and cold-water coral ecosystems. *Simp. Margen Ibérico Atlántico*, MIA09:281–284. http://digital.csic.es/bitstream/10261/20974/1/MIA09_ORTEGAL.pdf
- Hilgen, F.J., 1991. Extension of the astronomically calibrated (polarity) time scale to the Miocene/Pliocene boundary. *Earth Planet. Sci. Lett.*, 107(2):349–368. doi:[10.1016/0012-821X\(91\)90082-S](https://doi.org/10.1016/0012-821X(91)90082-S)
- Hyndman, R.D., Erickson, A.J., and Von Herzen, R.P., 1974. Geothermal measurements on DSDP Leg 26. In Davies, T.A., Luyendyk, B.P., et al., *Init. Repts. DSDP*, 26: Washington, DC (U.S. Govt. Printing Office), 451–463. doi:[10.2973/dsdp.proc.26.113.1974](https://doi.org/10.2973/dsdp.proc.26.113.1974)
- Iglesias, J., 2009. Sedimentation on the Cantabrian continental margin from late Oligocene to Quaternary [Ph.D. thesis]. Univ. Vigo, Spain.
- Iorga, M.C., and Lozier, M.S., 1999. Signatures of the Mediterranean Outflow from a North Atlantic climatology—1. Salinity and density fields. *J. Geophys. Res. [Oceans]*, 104(C11):25985–26029. doi:[10.1029/1999JC900115](https://doi.org/10.1029/1999JC900115)
- Kaiho, K., 1999. Effect of organic carbon flux and dissolved oxygen on the benthic foraminiferal oxygen index (BFOI). *Mar. Micropaleontol.*, 37(1):67–76. doi:[10.1016/S0377-8398\(99\)00008-0](https://doi.org/10.1016/S0377-8398(99)00008-0)
- Kawagata, S., Hayward, B.W., Grenfell, H.R., and Sabaa, A., 2005. Mid-Pleistocene extinction of deep-sea foraminifera in the North Atlantic Gateway (ODP Sites 980 and 982). *Palaeogeogr., Palaeoclimatol., Palaeoecol.*, 221(3–4):267–291. doi:[10.1016/j.palaeo.2005.03.001](https://doi.org/10.1016/j.palaeo.2005.03.001)
- Leckie, R.M., and Olson, H.C., 2003. Foraminifera as proxies of sea-level change on siliciclastic margins. In Olson, H.C., and Leckie, R.M. (Eds.), *Micropaleontologic Proxies of Sea-Level Change and Stratigraphic Discontinuities*. Spec. Publ.—SEPM (Soc. Sediment. Geol.), 75:5–19.
- Llave, E., Hernández-Molina, F.J., Somoza, L., Stow, D.A.V., and Díaz Del Río, V., 2007. Quaternary evolution of the contourite depositional system in the Gulf of Cádiz. *Geol. Soc. Spec. Publ.*, 276:49–79. doi:[10.1144/GSL.SP.2007.276.01.03](https://doi.org/10.1144/GSL.SP.2007.276.01.03)
- Llave, E., Matias, H., Hernández-Molina, F.J., Ercilla, G., Stow, D.A.V., and Medialdea, T., 2011. Pliocene–Quaternary contourites along the northern Gulf of Cadiz margin: sedimentary stacking pattern and regional distribution. *Geo-Mar. Lett.*, 31(5–6):377–390. doi:[10.1007/s00367-011-0241-3](https://doi.org/10.1007/s00367-011-0241-3)
- Lourens, L., Hilgen, F., Shackleton, N.J., Laskar, J., and Wilson, D., 2004. The Neogene period. In Gradstein, F.M., Ogg, J.G., and Smith, A. (Eds.), *A Geologic Time Scale 2004*: Cambridge (Cambridge Univ. Press), 409–440.
- Mena, A., Francés, G., Pérez Arlucea, M., Hanebuth, T.J.J., and Nombela, M.A., 2010. Sedimentary evolution of the Galicia inner basin during the last 70 k.y. *Geo-Temas*, 11:125–126.
- Meyers, P.A., 1997. Organic geochemical proxies of paleoceanographic, paleolimnologic, and paleoclimatic processes. *Org. Geochem.*, 27(5–6):213–250. doi:[10.1016/S0146-6380\(97\)00049-1](https://doi.org/10.1016/S0146-6380(97)00049-1)
- Murray, J.W., 2006. *Ecology and Applications of Benthic Foraminifera*: Cambridge (Cambridge Univ. Press).
- Pereira, R., and Alves, T.M., 2011. Margin segmentation prior to continental break-up: a seismic-stratigraphic record of multiphased rifting in the North Atlantic (southwest Iberia). *Tectonophysics*, 505(1–4):17–34. doi:[10.1016/j.tecto.2011.03.011](https://doi.org/10.1016/j.tecto.2011.03.011)
- Pribnow, D., Kinoshita, M., and Stein, C., 2000. *Thermal Data Collection and Heat Flow Recalculations for Ocean Drilling Program Legs 101–180*: Hanover, Germany (Inst. Joint Geosci. Res., Inst. Geowiss. Gemeinschaftsauf. [GGA]). <http://www-odp.tamu.edu/publications/heatflow/ODPReprt.pdf>
- Raffi, I., Backman, J., Fornaciari, E., Pälike, H., Rio, D., Lourens, L., and Hilgen, F., 2006. A review of calcareous nannofossil astrobiochronology encompassing the past 25 million years. *Quat. Sci. Rev.*, 25(23–24):3113–3137. doi:[10.1016/j.quascirev.2006.07.007](https://doi.org/10.1016/j.quascirev.2006.07.007)
- Raffi, I., Backman, J., Rio, D., and Shackleton, N.J., 1993. Plio–Pleistocene nannofossil biostratigraphy and calibration to oxygen isotope stratigraphies from Deep Sea Drilling Project Site 607 and Ocean Drilling Program Site 677. *Paleoceanography*, 8(3):387–408. doi:[10.1029/93PA00755](https://doi.org/10.1029/93PA00755)
- Raymo, M.E., Ruddiman, W.F., Backman, J., Clement, B.M., and Martinson, D.G., 1989. Late Pliocene variation in Northern Hemisphere ice sheets and North Atlantic deep water circulation. *Paleoceanography*, 4(4):413–446. doi:[10.1029/PA004i004p00413](https://doi.org/10.1029/PA004i004p00413)



- Schönfeld, J., 1997. The impact of the Mediterranean Outflow Water (MOW) on benthic foraminiferal assemblages and surface sediments at the southern Portuguese continental margin. *Mar. Micropaleontol.*, 29(3–4):211–236. doi:[10.1016/S0377-8398\(96\)00050-3](https://doi.org/10.1016/S0377-8398(96)00050-3)
- Schönfeld, J., 2002. Recent benthic foraminiferal assemblages in deep high-energy environments from the Gulf of Cádiz (Spain). *Mar. Micropaleontol.*, 44(3–4):141–162. doi:[10.1016/S0377-8398\(01\)00039-1](https://doi.org/10.1016/S0377-8398(01)00039-1)
- Schönfeld, J., and Zahn, R., 2000. Late glacial to Holocene history of the Mediterranean Outflow. Evidence from benthic foraminiferal assemblages and stable isotopes at the Portuguese margin. *Palaeogeogr., Palaeoclimatol., Palaeoecol.*, 159(1–2):85–111. doi:[10.1016/S0031-0182\(00\)00035-3](https://doi.org/10.1016/S0031-0182(00)00035-3)
- Serra, N., Ambar, I., and Boutov, D., 2010. Surface expression of Mediterranean water dipoles and their contribution to the shelf/slope–open ocean exchange. *Ocean Sci.*, 6(1):191–209. doi:[10.5194/os-6-191-2010](https://doi.org/10.5194/os-6-191-2010)
- Sierro, F.J., Hernández-Almeida, I., Alonso-García, M., and Flores, J.A., 2009. Data report: Pliocene–Pleistocene planktonic foraminifer bioevents at IODP Site U1313. In Channell, J.E.T., Kanamatsu, T., Sato, T., Stein, R., Alvarez Zarikian, C.A., Malone, M.J., and the Expedition 303/306 Scientists, *Proc. IODP*, 303/306: College Station, TX (Integrated Ocean Drilling Program Management International, Inc.). doi:[10.2204/iodp.proc.303306.205.2009](https://doi.org/10.2204/iodp.proc.303306.205.2009)
- Stow, D., Hernández-Molina, F.J., Hodell, D., and Alvarez Zarikian, C.A., 2011. Mediterranean outflow: environmental significance of the Mediterranean Outflow Water and its global implications. *IODP Sci. Prosp.*, 339. doi:[10.2204/iodp.sp.339.2011](https://doi.org/10.2204/iodp.sp.339.2011)
- Terrinha, P., Pinheiro, L.M., Henriet, J.-P., Matias, L., Ivanov, M.K., Monteiro, J.H., Akhmetzhanov, A., Volkonskaya, A., Cunha, T., Shaskin, P., and Rovere, M., 2003. Tsunamigenic-seismogenic structures, neotectonics, sedimentary processes, and slope stability on the southwest Portuguese margin. *Mar. Geol.*, 195(1–4):55–73. doi:[10.1016/S0025-3227\(02\)00682-5](https://doi.org/10.1016/S0025-3227(02)00682-5)
- Turon, J.-L., Lézine, A.-M., and Denèfle, M., 2003. Land–sea correlations for the last glaciation inferred from a pollen and dinocyst record from the Portuguese margin.
- Quat. Res., 59(1):88–96. doi:[10.1016/S0033-5894\(02\)00018-2](https://doi.org/10.1016/S0033-5894(02)00018-2)
- van Morkhoven, F.P.C.M., Berggren, W.A., and Edwards, A.S., 1986. *Cenozoic Cosmopolitan Deep-Water Benthic Foraminifera*. Bull. Cent. Rech. Explor.—Prod. Elf-Aquitaine, 11.
- Van Rooij, D., De Mol, B., Huvenne, V., Ivanov, M., and Henriet, J.-P., 2003. Seismic evidence of current-controlled sedimentation in the Belgica mound province, upper Porcupine slope, southwest of Ireland. *Mar. Geol.*, 195(1–4):31–53. doi:[10.1016/S0025-3227\(02\)00681-3](https://doi.org/10.1016/S0025-3227(02)00681-3)
- Van Rooij, D., Iglesias, J., Hernández-Molina, F.J., Ercilla, G., Gomez-Ballesteros, M., Casas, D., Llave, E., De Hauwere, A., Garcia-Gil, S., Acosta, J., and Henriet, J.-P., 2010. The Le Danois contourite depositional system: interactions between the Mediterranean Outflow Water and the upper Cantabrian slope (North Iberian margin). *Mar. Geol.*, 274(1–4):1–20 doi:[10.1016/j.margeo.2010.03.001](https://doi.org/10.1016/j.margeo.2010.03.001)
- Weaver, P.P.E., and Clement, B.M., 1987. Magnetobiostratigraphy of planktonic foraminiferal datums: Deep Sea Drilling Project Leg 94, North Atlantic. In Ruddiman, W.F., Kidd, R.B., Thomas, E., et al., *Init. Repts. DSDP*, 94: Washington (U.S. Govt. Printing Office), 815–829. doi:[10.2973/dsdp.proc.94.120.1987](https://doi.org/10.2973/dsdp.proc.94.120.1987)
- Wei, W., 1993. Calibration of upper Pliocene–lower Pleistocene nannofossil events with oxygen isotope stratigraphy. *Paleoceanography*, 8(1):85–99. doi:[10.1029/92PA02504](https://doi.org/10.1029/92PA02504)
- Zachariasse, W.J., Zijderveld, J.D.A., Langereis, C.G., Hilgen, F.J., and Verhallen, P.J.J.M., 1989. Early late Pliocene biochronology and surface water temperature variations in the Mediterranean. *Mar. Micropaleontol.*, 14(4):339–355. doi:[10.1016/0377-8398\(89\)90018-2](https://doi.org/10.1016/0377-8398(89)90018-2)
- Zitellini, N., Rovere, M., Terrinha, P., Chierici, F., Matias, L., and the Bigsets Team, 2004. Neogene through Quaternary tectonic reactivation of SW Iberian passive margin. *Pure Appl. Geophys.*, 161(3):565–587. doi:[10.1007/s0024-003-2463-4](https://doi.org/10.1007/s0024-003-2463-4)

Publication: 17 June 2013
MS 339-109



Figure F1. 3-D sketch showing the plastered drift on the middle slope terrace from the most distal sector of the contourite depositional system of the Gulf of Cádiz and west off Portugal (made by H. Pereira, Escola Secundária de Loulé, using Mirone and iView4D software).

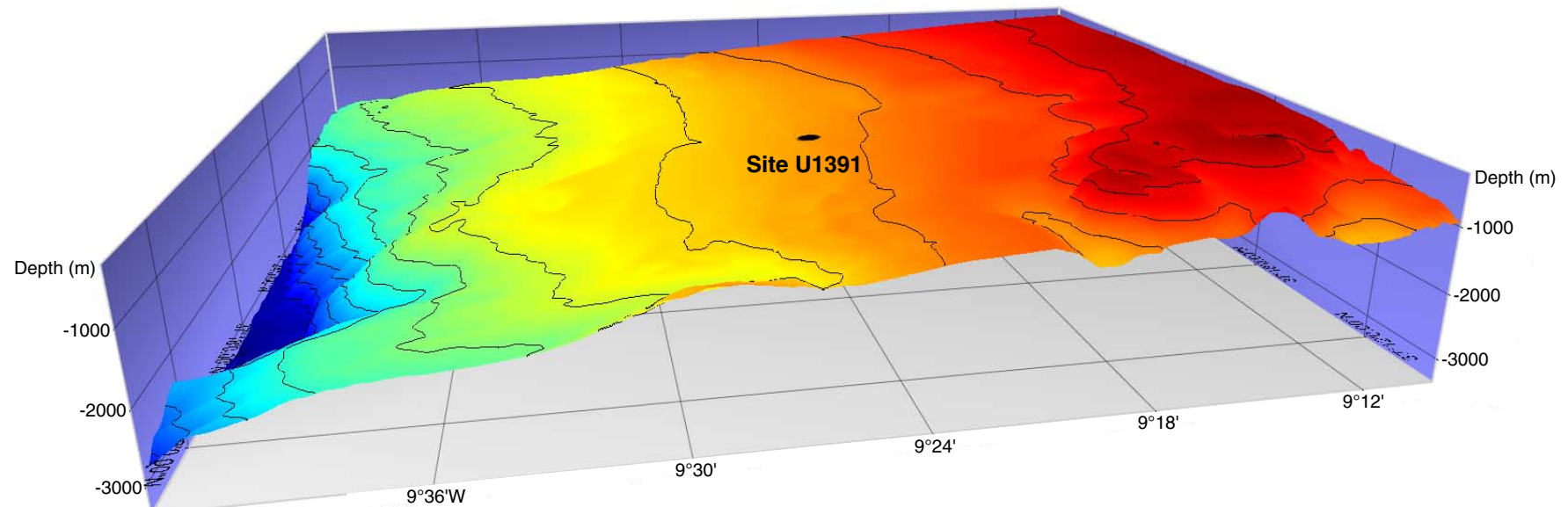


Figure F2. Bathymetric sketch showing the location of Site U1391 ($37^{\circ}21.5322'N$, $9^{\circ}24.6558'W$) on the plastered drift over the middle slope terrace in the Portuguese margin.

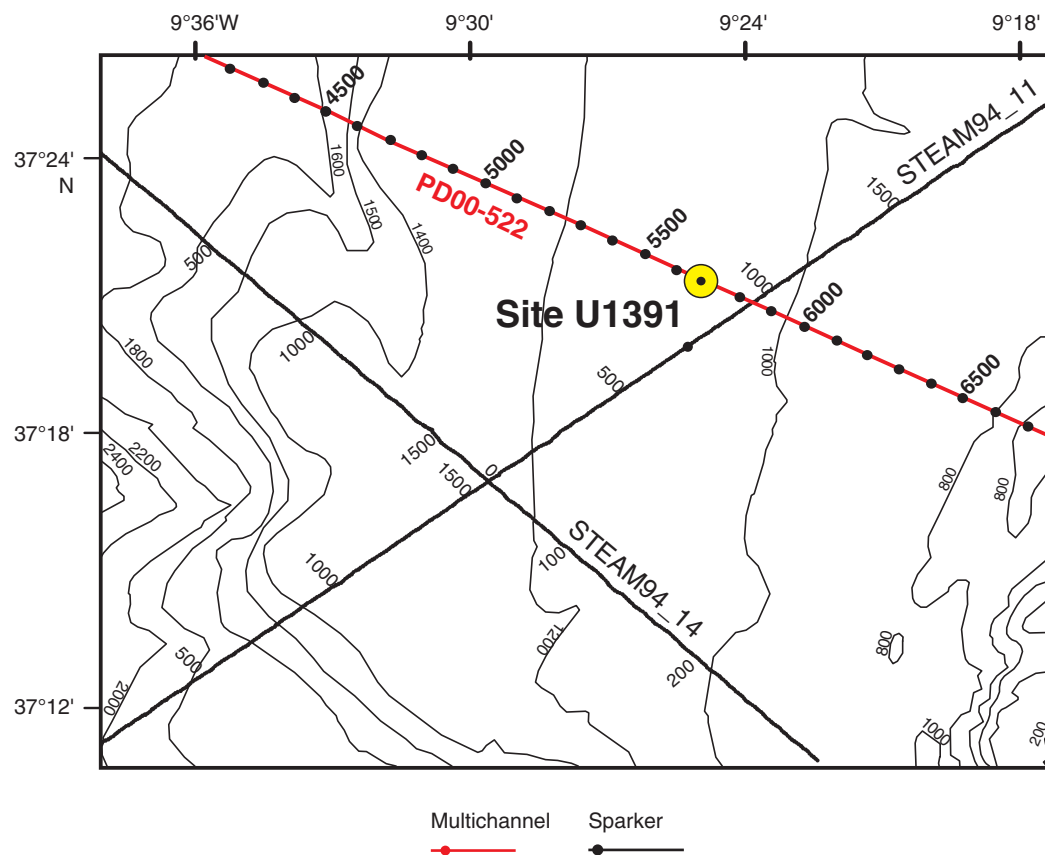


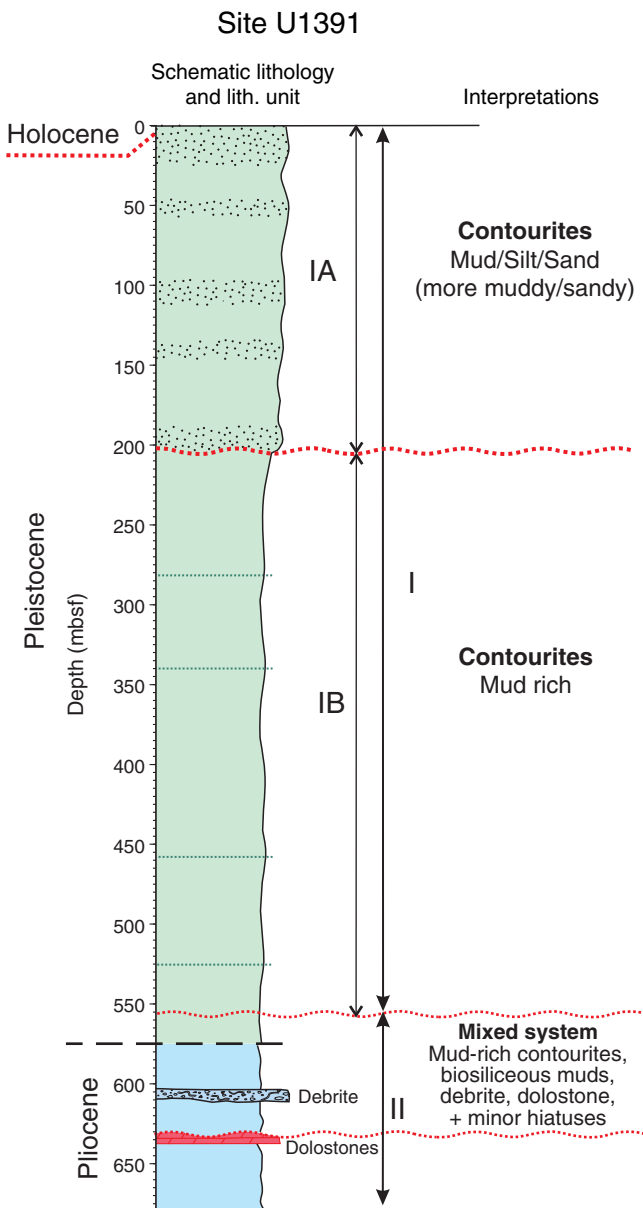
Figure F3. Graphic lithology summary log, Site U1391.

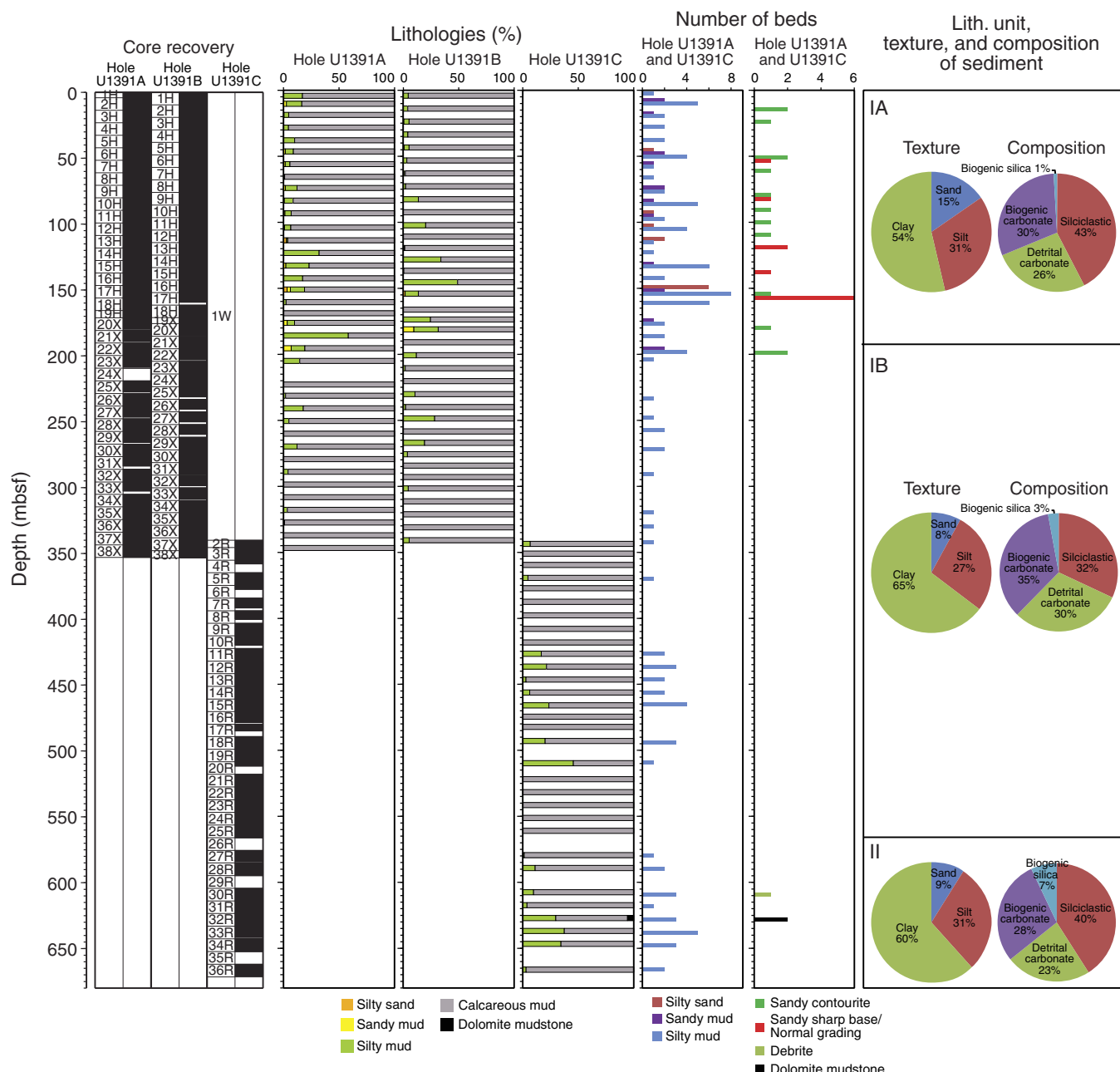
Figure F4. Plots of downhole variations in lithologies, texture and composition for Site U1391.

Figure F5. XRD peak intensity profiles, Site U1391.

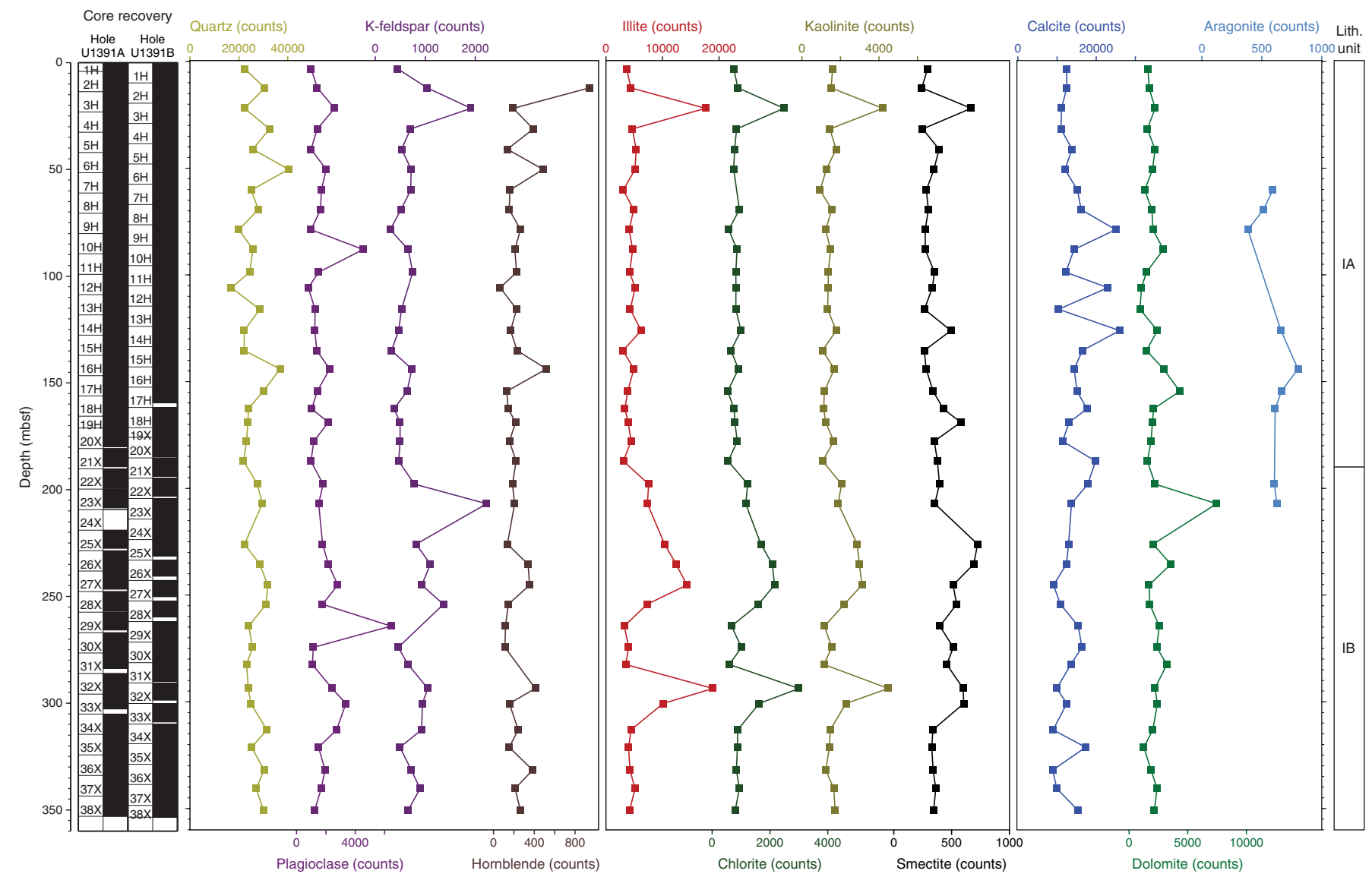


Figure F6. Graphic lithology summaries. A. Hole U1391A. (Continued on next two pages.)

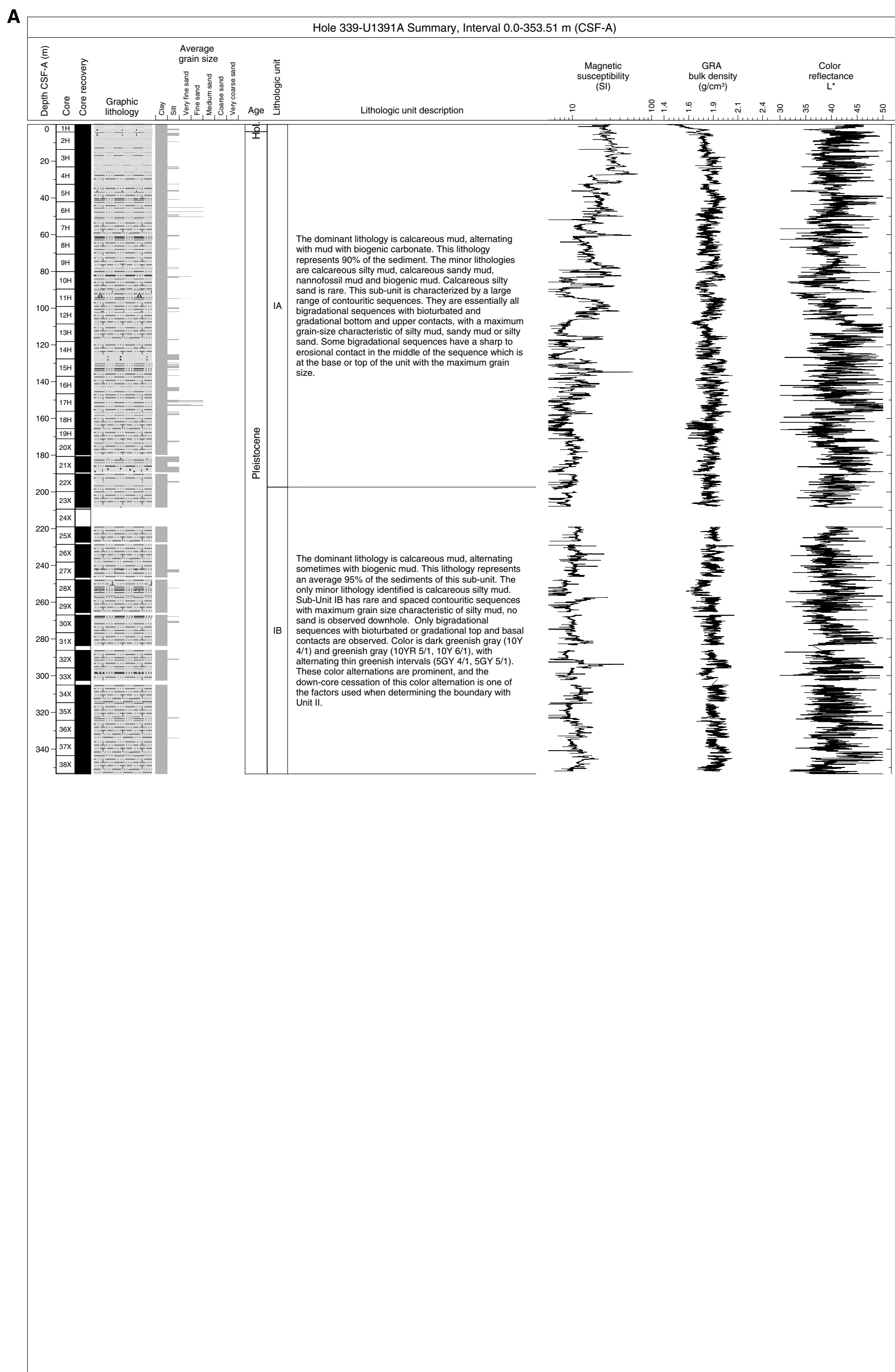


Figure F6 (continued). B. Hole U1391B. (Continued on next page.)

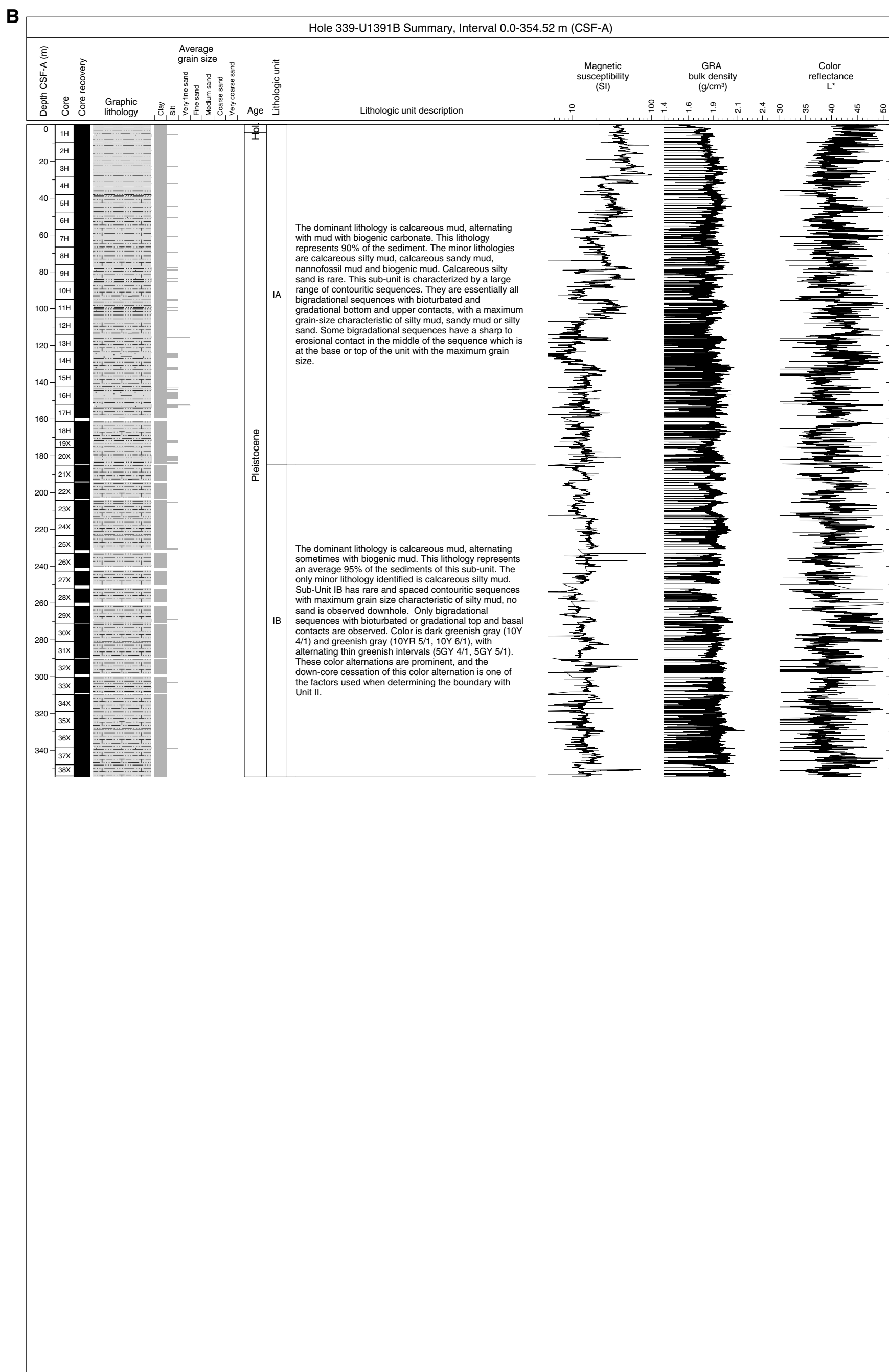


Figure F6 (continued). C. Hole U1391C.

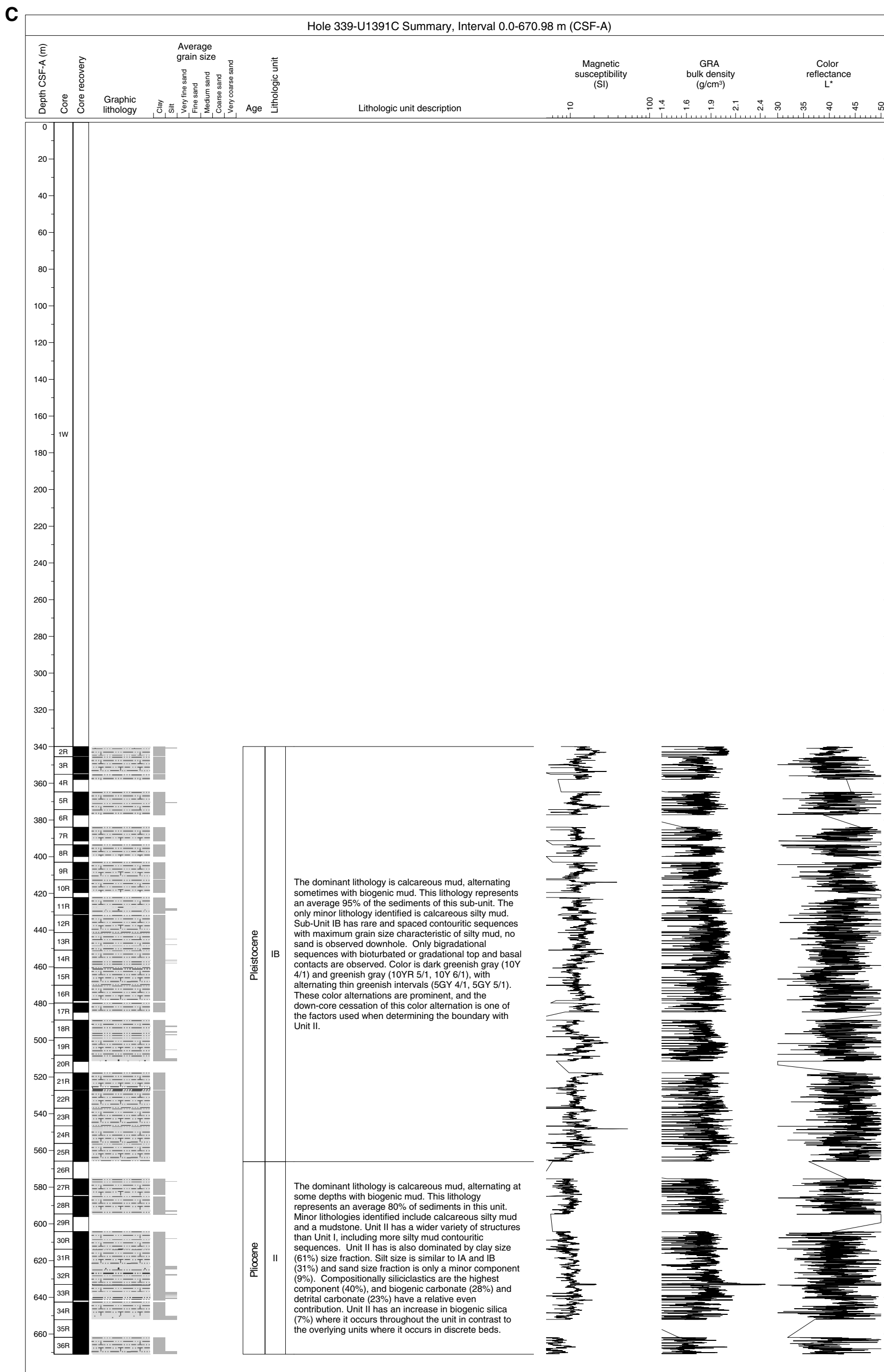


Figure F7. A, B. XRD patterns of bulk (black) and ethylene-glycolated (red) sediment samples, Site U1387. (Continued on next page.)

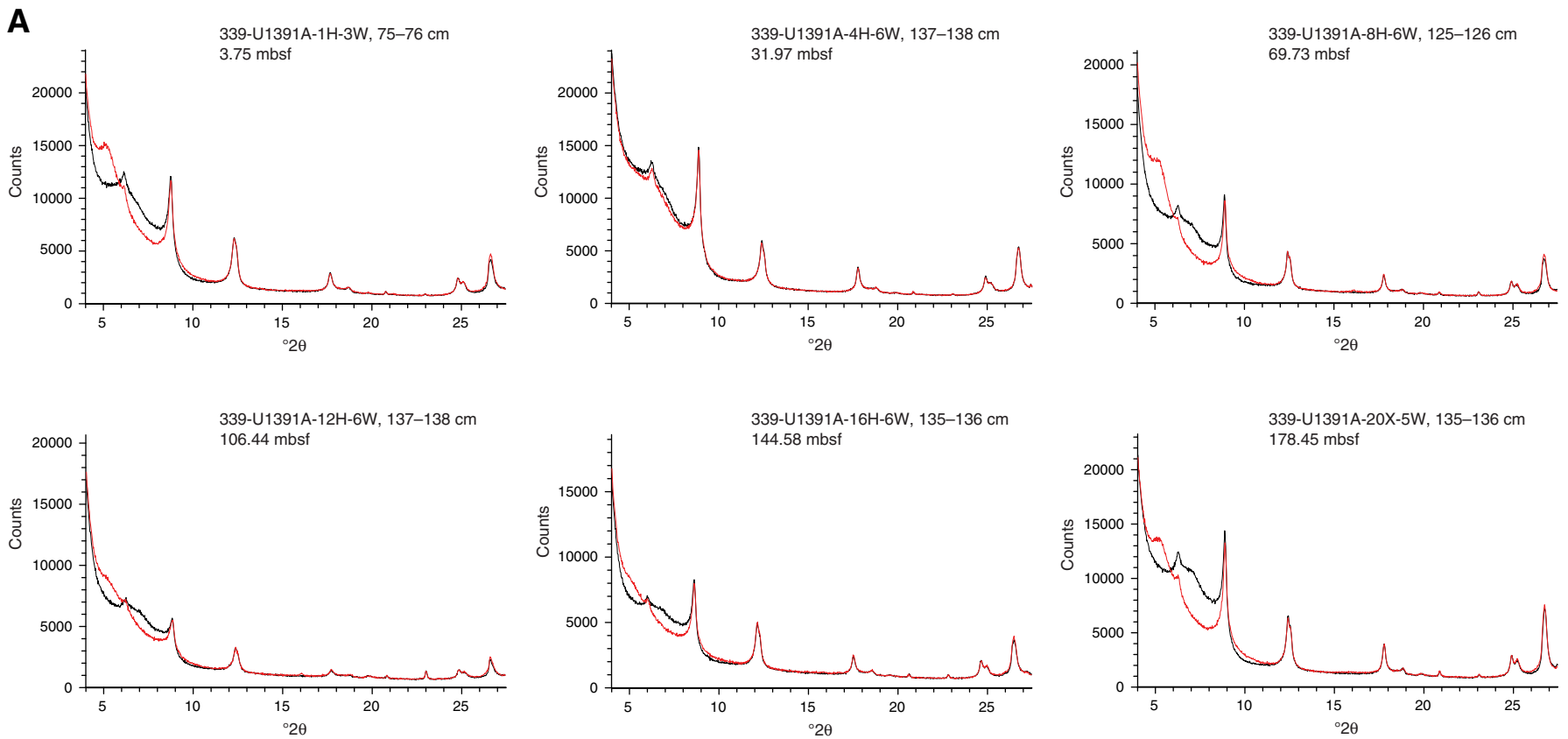


Figure F7 (continued).

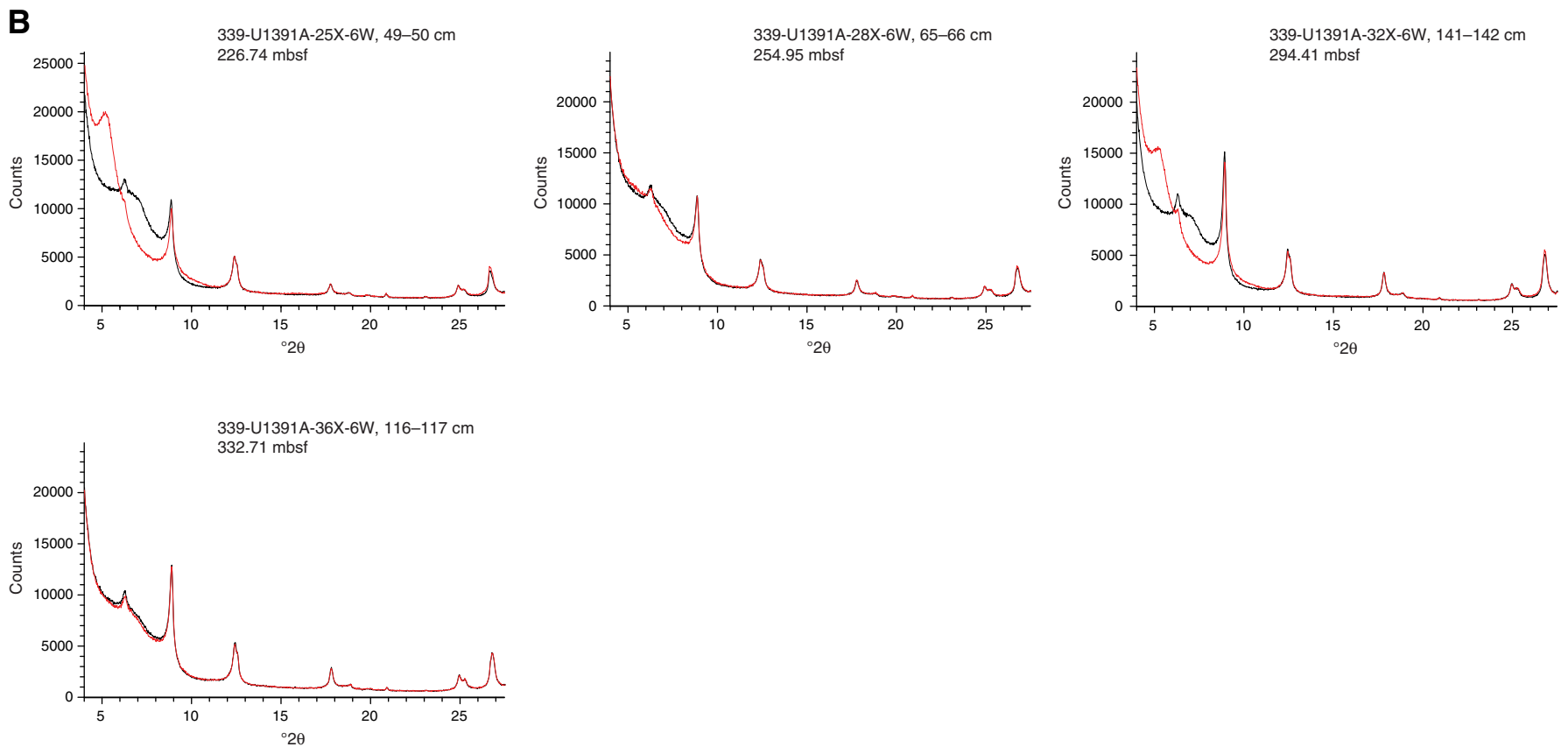


Figure F8. Core image of bi-gradational sequence and internal contact with a foraminifer-rich sand (Section 339-U1391A-6H-6A).

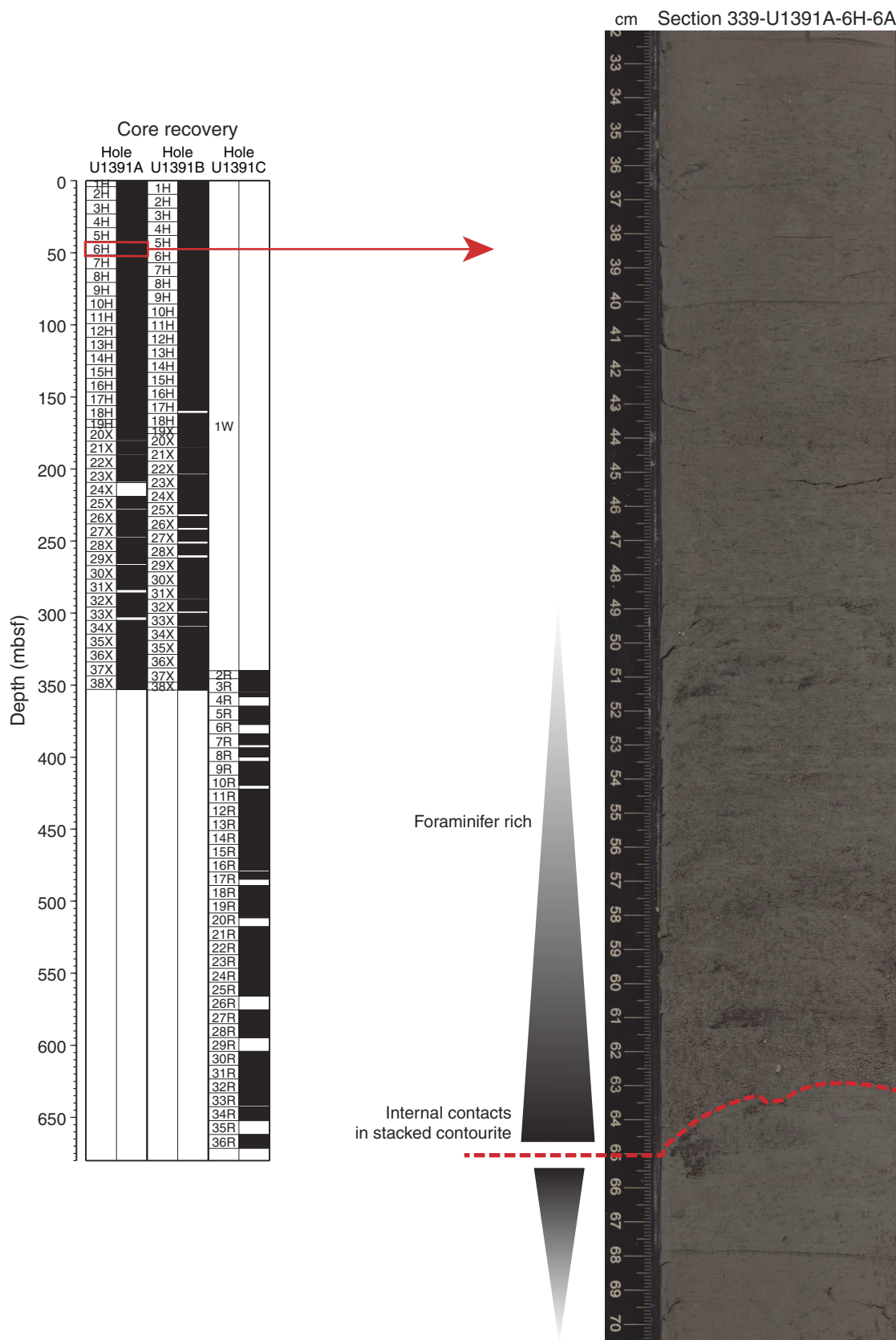


Figure F9. Core image of bi-gradiational sequence with sharp internal contact (Section 339-U1391A-9H-6A).

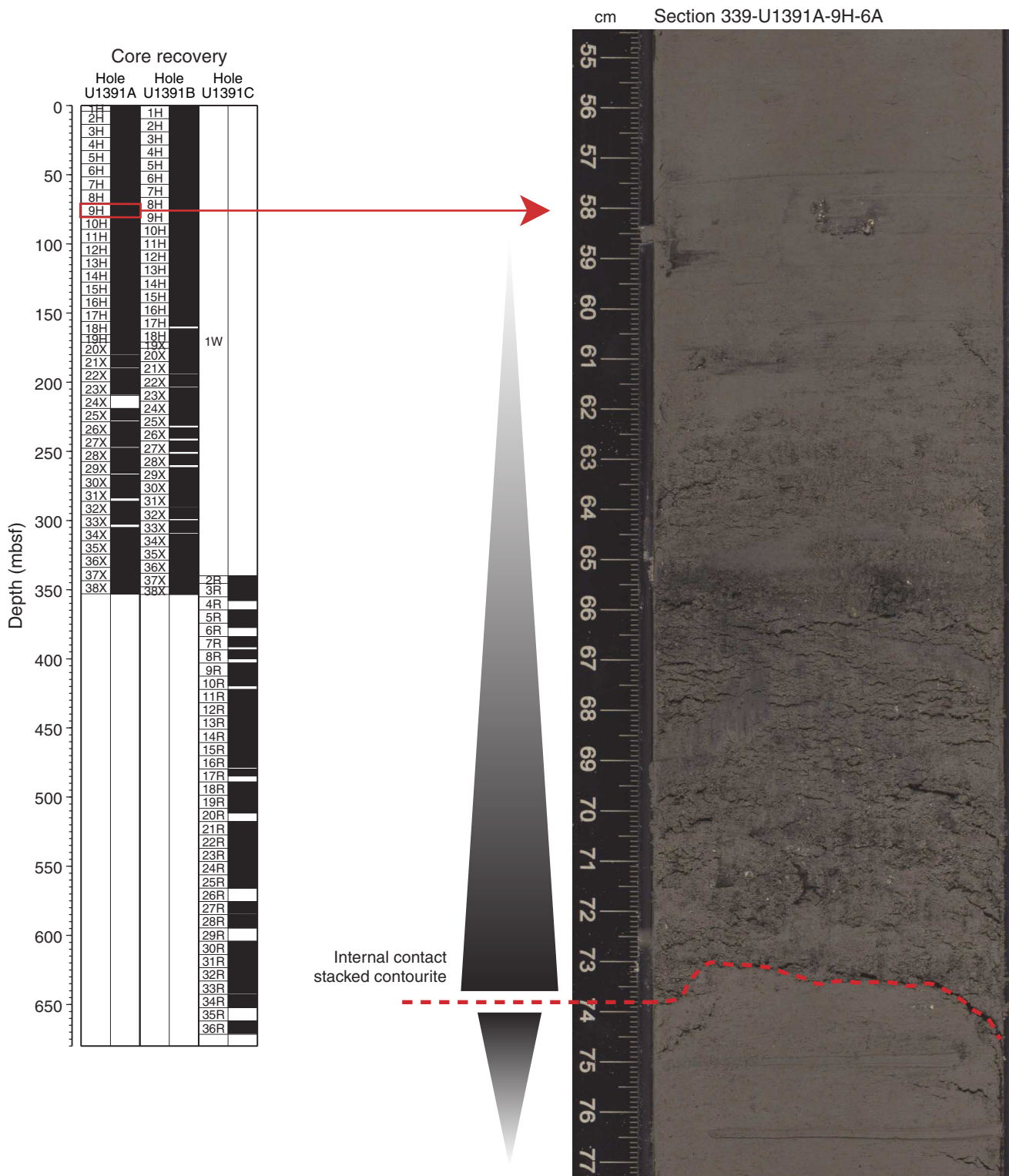


Figure F10. Core image of bi-gradational sequence and sharp internal contact with a foraminifer-rich sand (Section 339-U1391A-6H-4A).

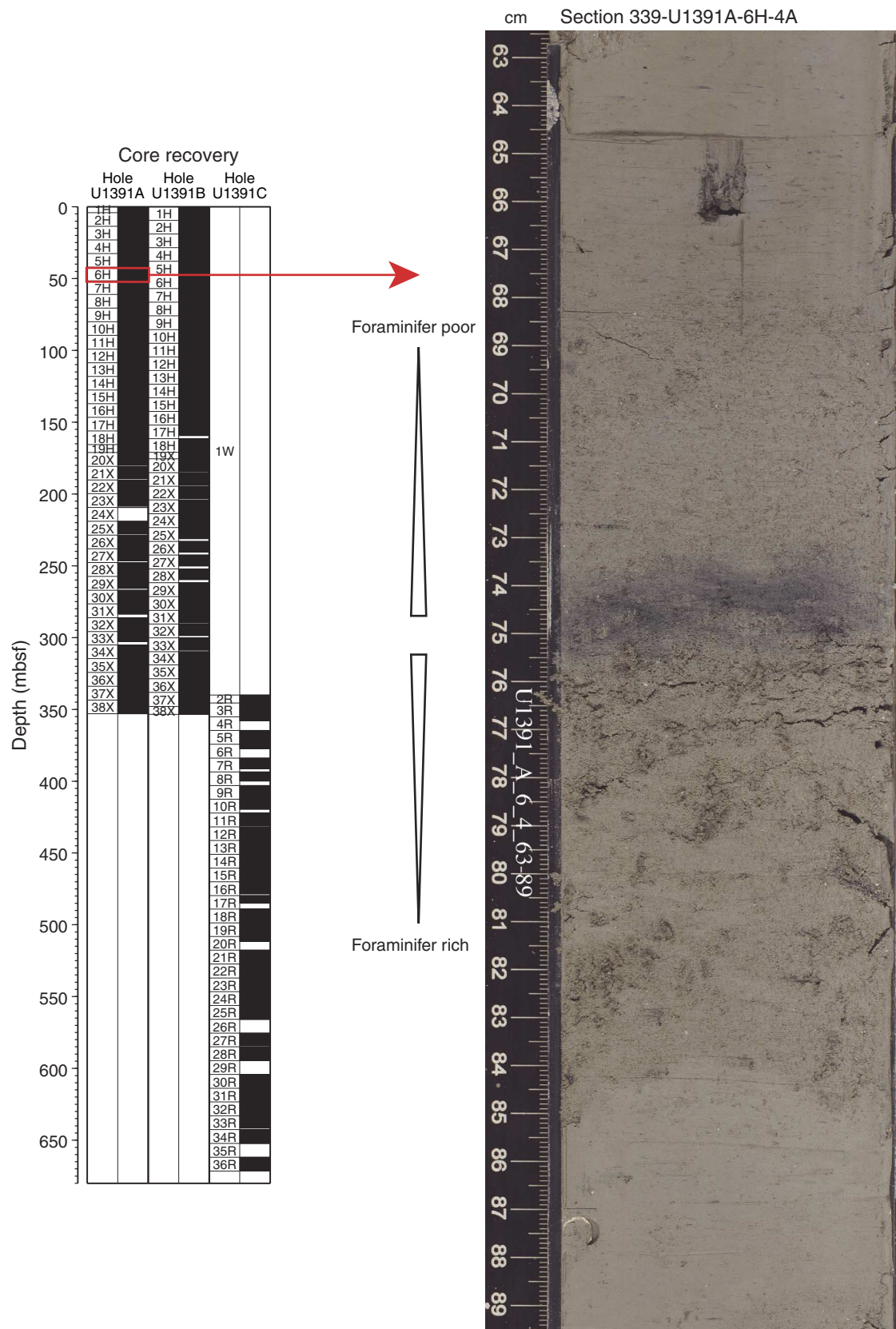


Figure F11. Core image of red-mottled mud (Section 339-U1391A-9H-5A).

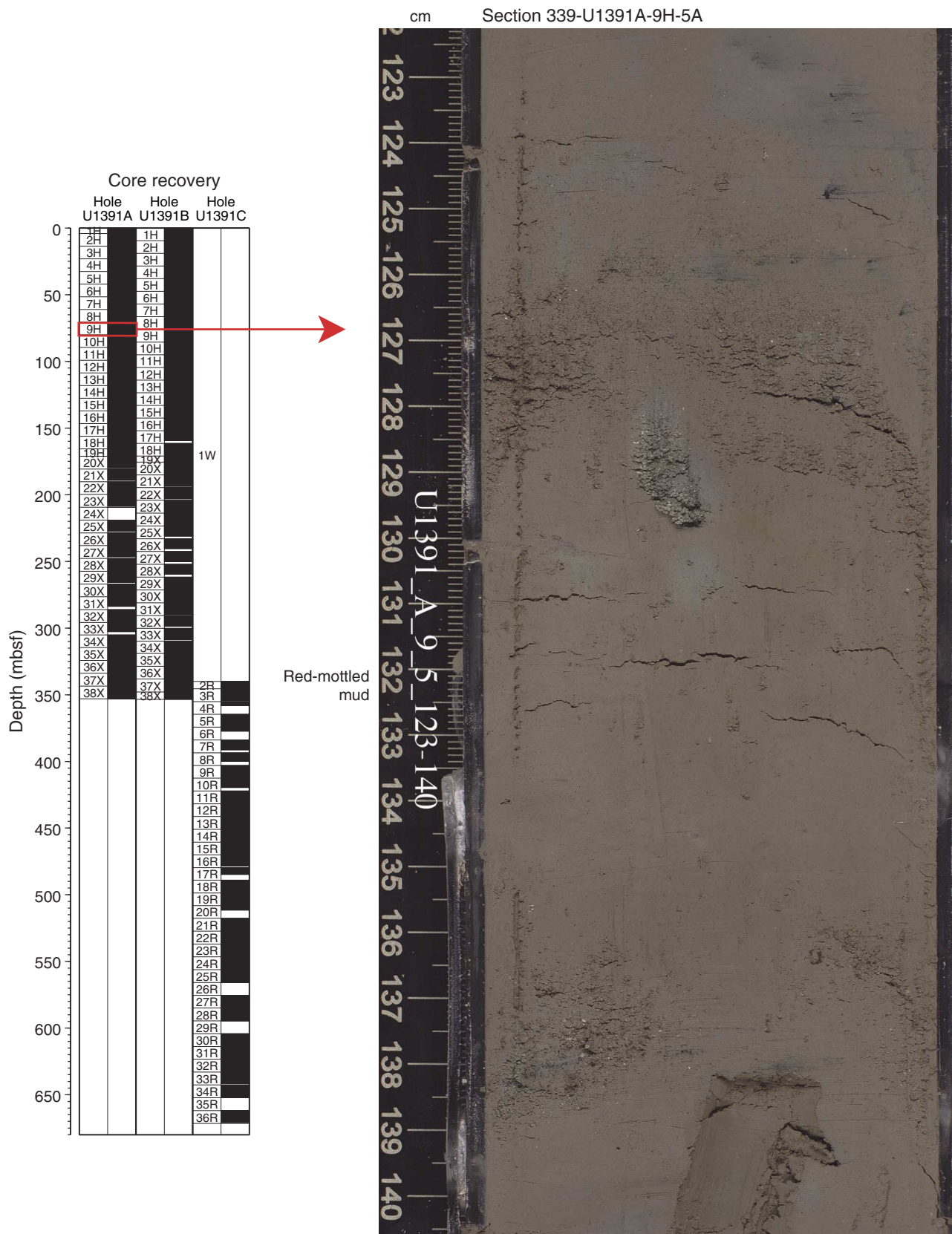


Figure F12. Core images of cross-laminated calcareous silt (Section 339-U1391C-15R-1A).

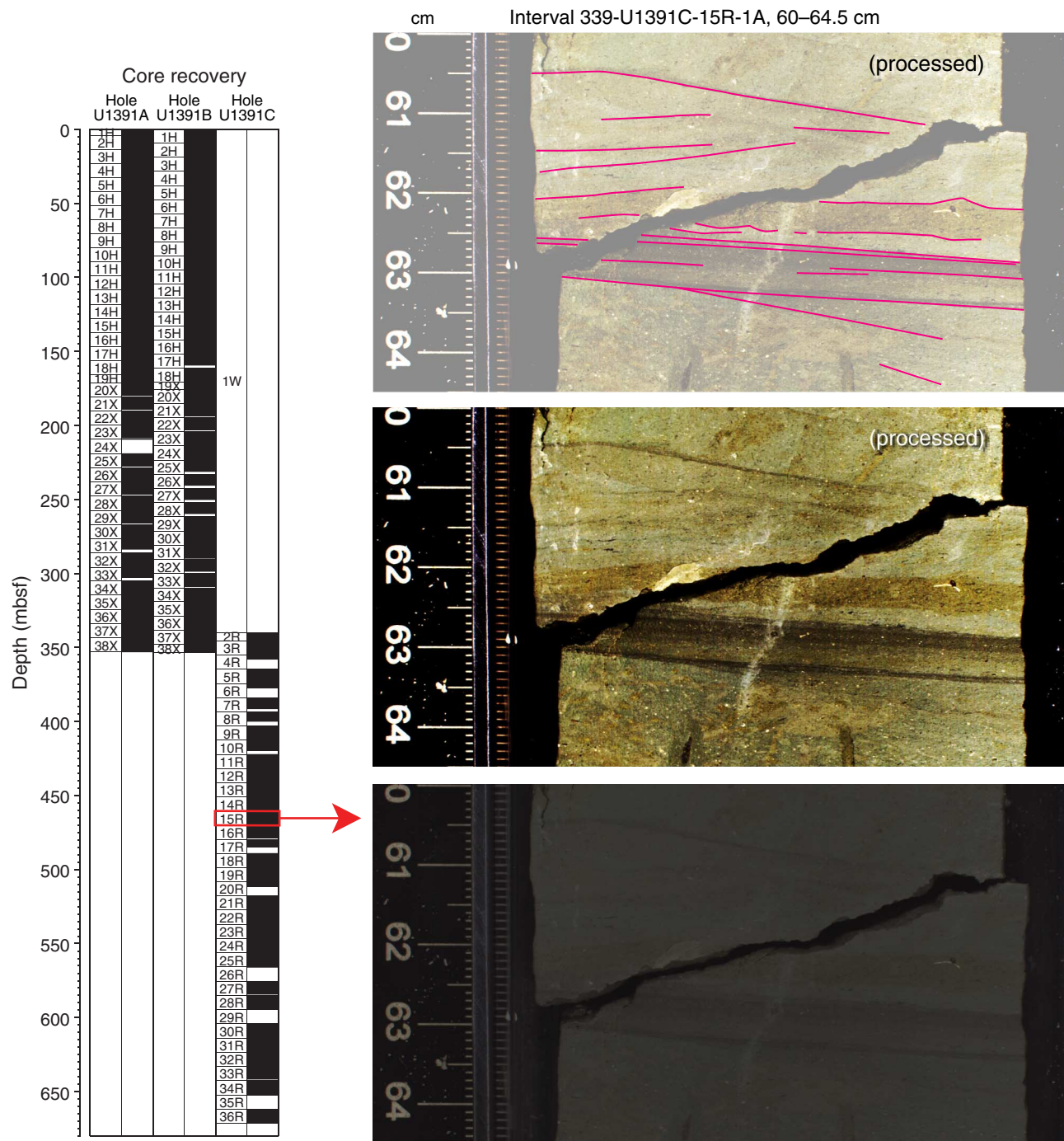


Figure F13. Core images of subparallel lamination in calcareous silt/mud (Section 339-U1391C-17R-4A).

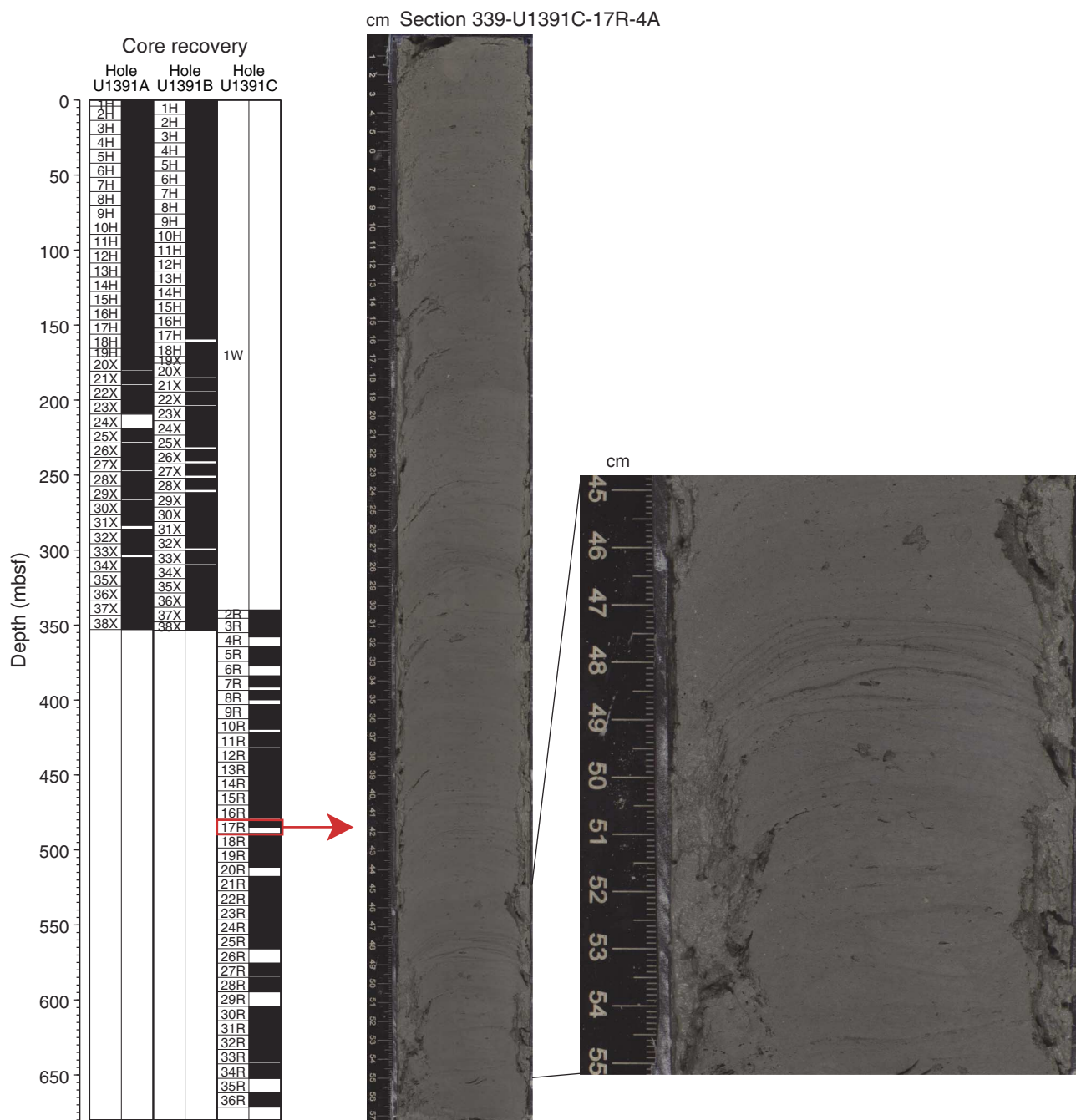


Figure F14. Core images of greenish gray to green color cycles (Section 339-U1391C-21R-1A).

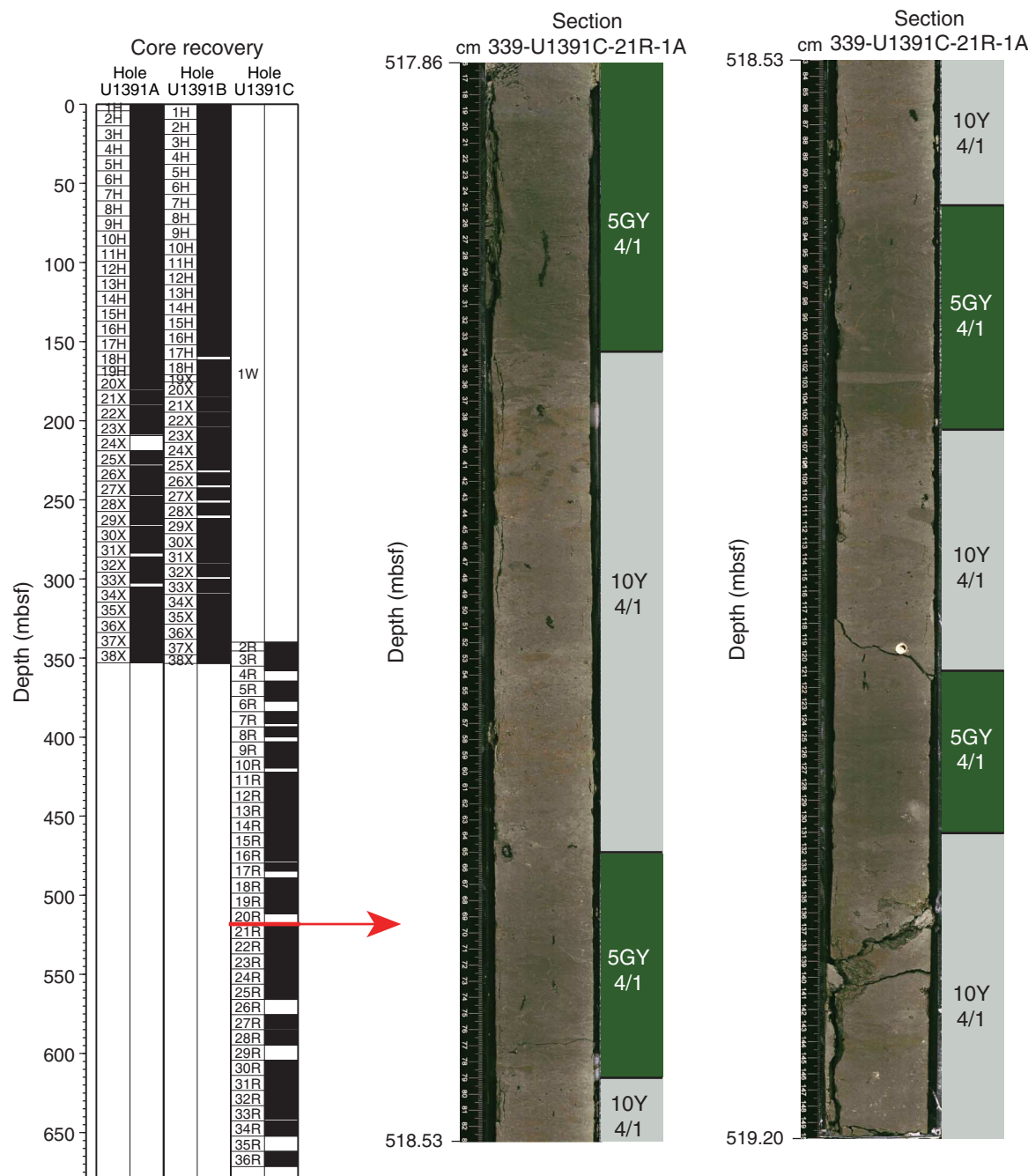


Figure F15. Core image of debrite (interval 339-U1391C-30R-1A, 0–38 cm).

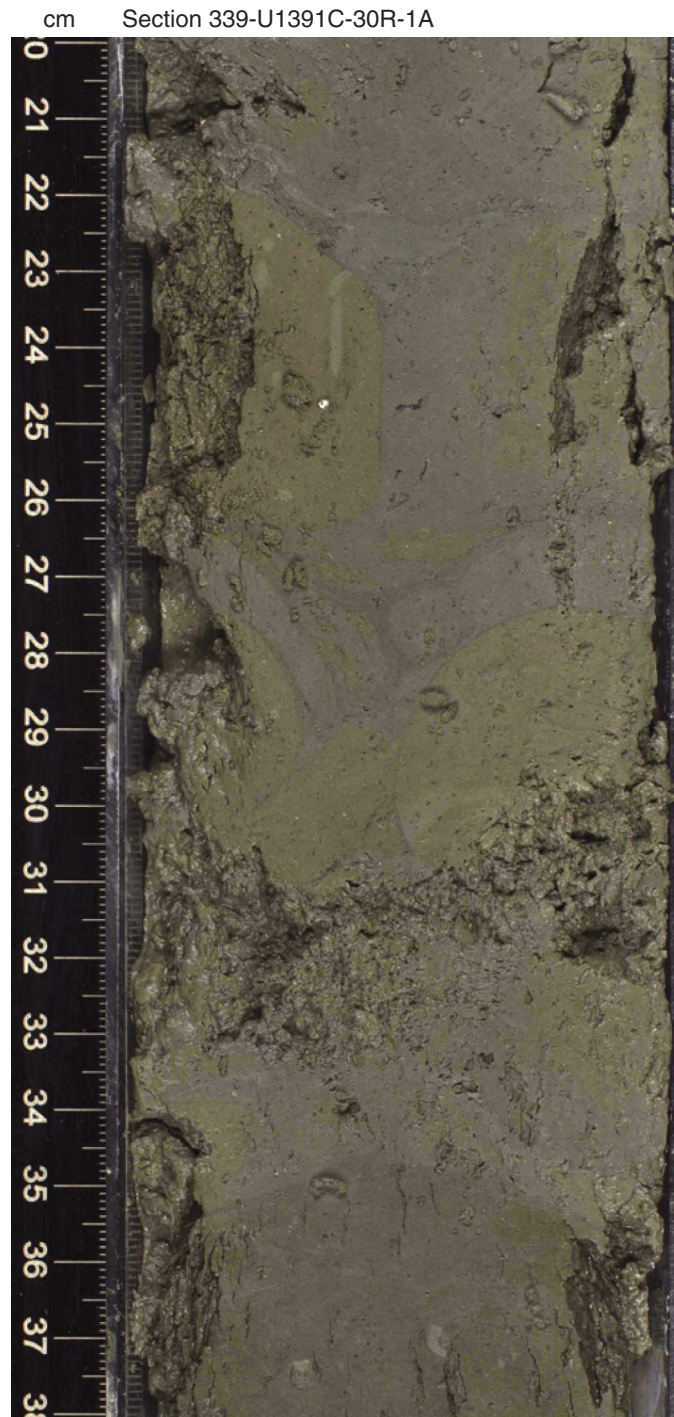


Figure F16. Core image and photomicrographs of dolomitic mudstone (interval 339-U1391C-32R-7A, 20–76 cm). Top photomicrograph taken under plane-polarized light; bottom photomicrograph taken under cross-polarized light.

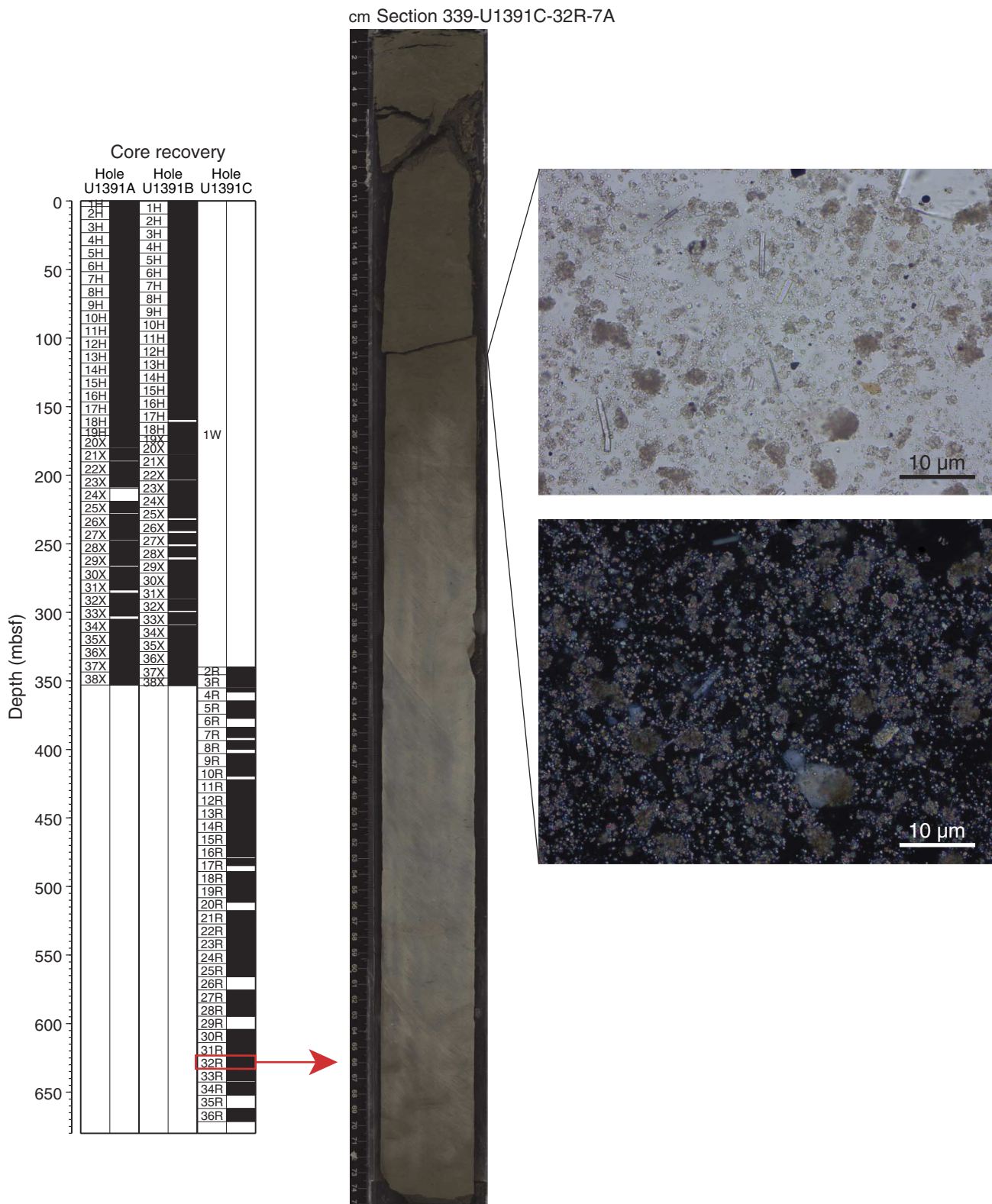


Figure F17. Core images of a microfault (interval 339-U1391C-34R-6, 29–53 cm).

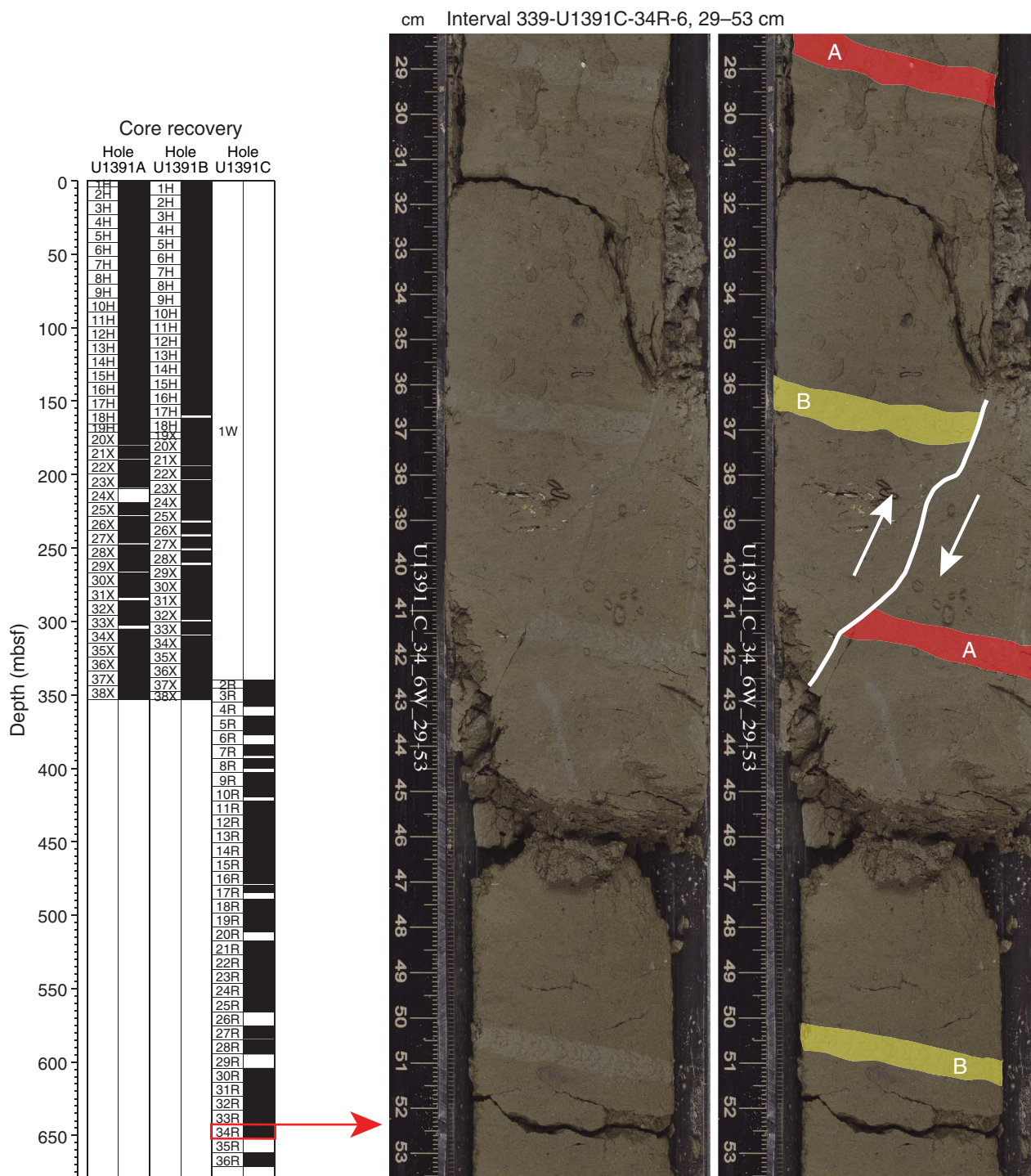


Figure F18. Biostratigraphic events vs. depth, Site U1391. Events are plotted at their mean depth (Table T4).

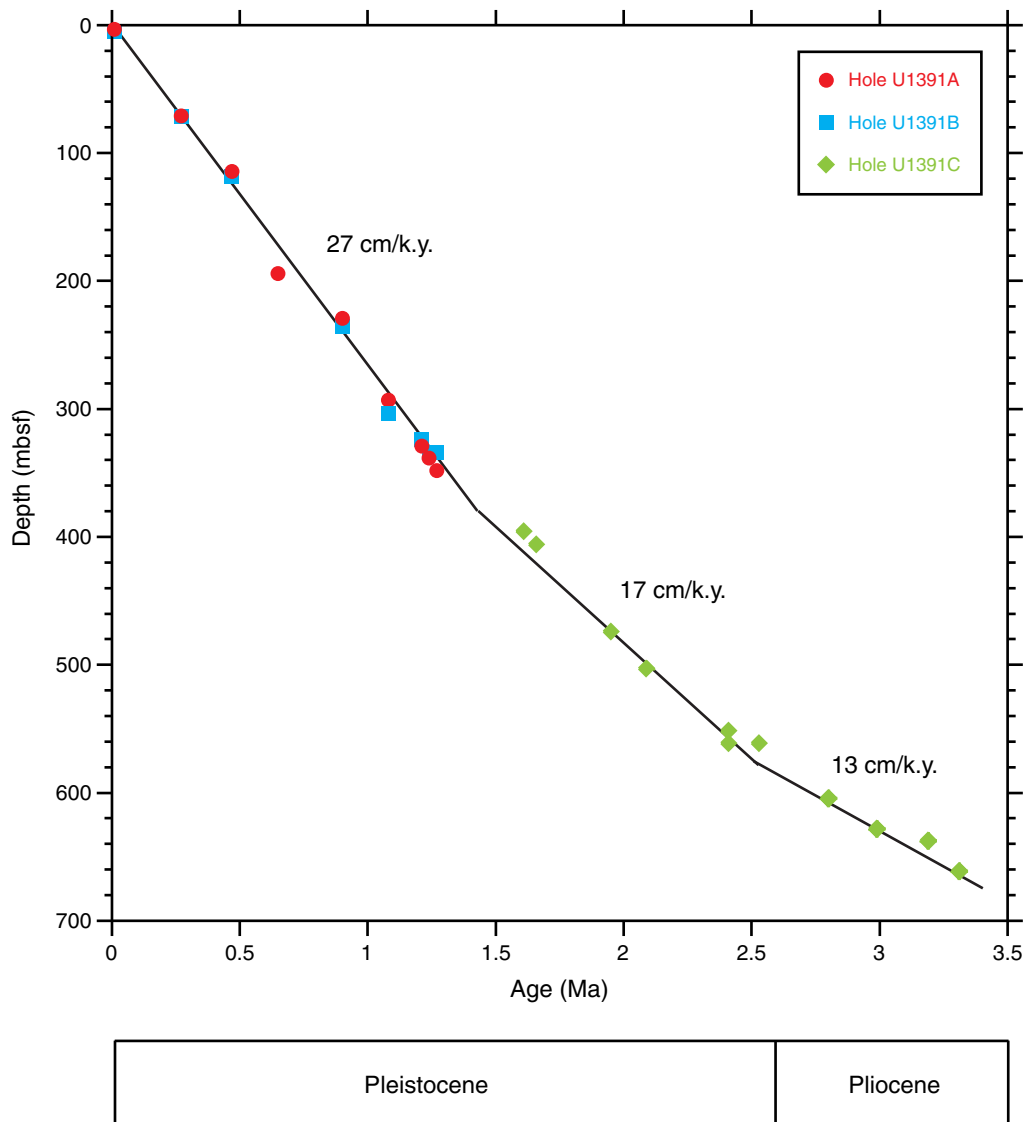


Figure F19. Preliminary pollen results from the analysis of eight samples from Site U1391. Mediterranean forest is mainly deciduous and evergreen *Quercus* and *Olea*. Dashed lines indicate 10 \times magnification of concentrations. TPS = total pollen and spores. Preservation: G = good, M = moderate, P = poor.

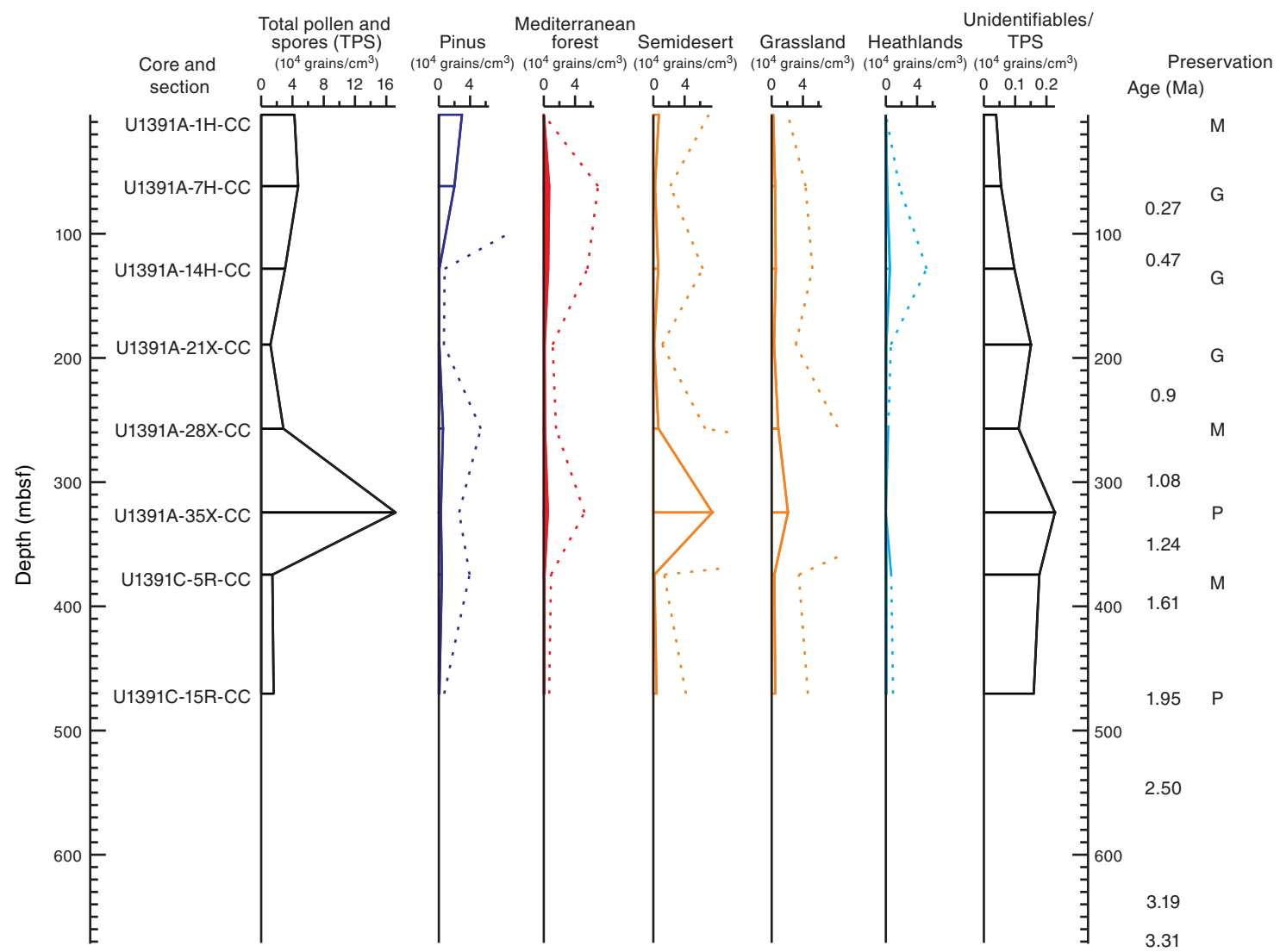


Figure F20. Paleomagnetism after 20 mT peak field AF demagnetization, Site U1391. In the Chron column, black = normal polarity, white = reversed polarity, and gray = zones or polarity boundaries without a clear magnetostratigraphic interpretation. In Inclination column, blue dashed lines = expected geocentric axial dipole inclinations at the site latitude during reversed (left) and normal (right) polarities. In Declination column, light blue circles = measured declinations and dark blue circles = FlexIt tool–corrected declinations. In Susceptibility column, gray lines represent SHMSL susceptibility plus 25×10^{-5} volume SI to better show the comparison with WRMSL susceptibility (black lines). (Figure shown on next three pages.)

Figure F20 (continued). A. Hole U1397A. (Caption shown on previous page.) (Continued on next page.)

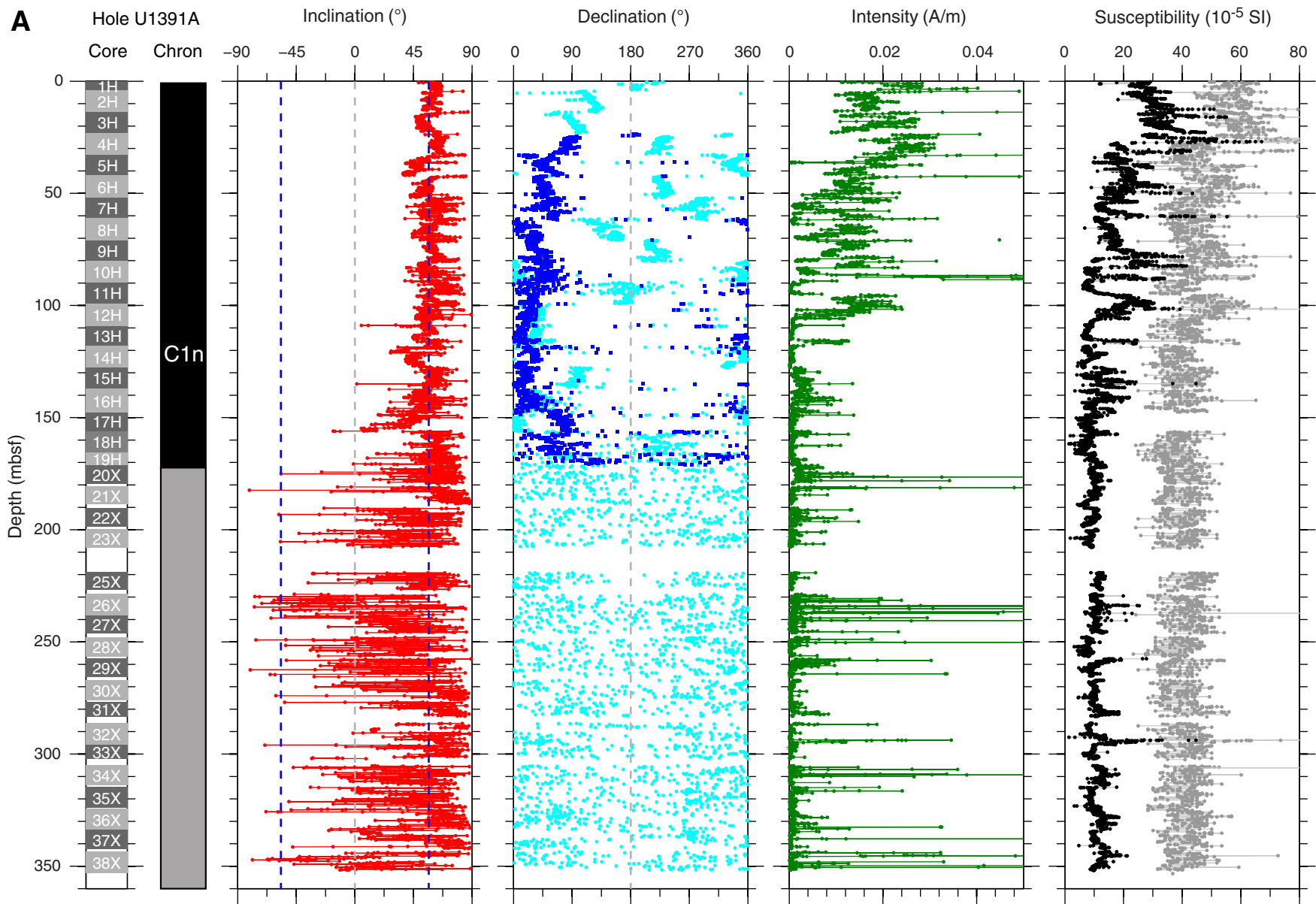


Figure F20 (continued). B. Hole U1391B. (Continued on next page.)

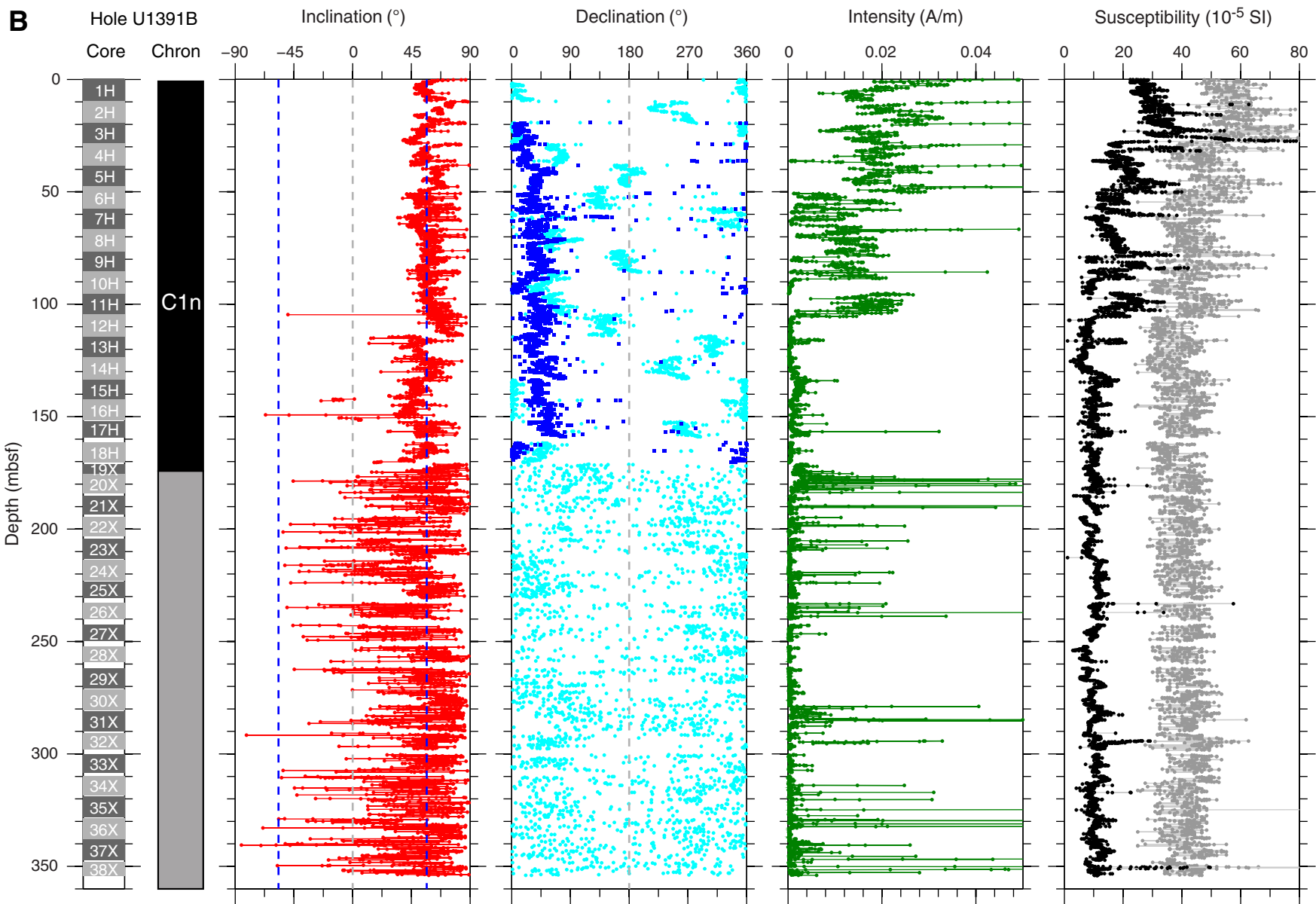


Figure F20 (continued). C. Hole U1391C.

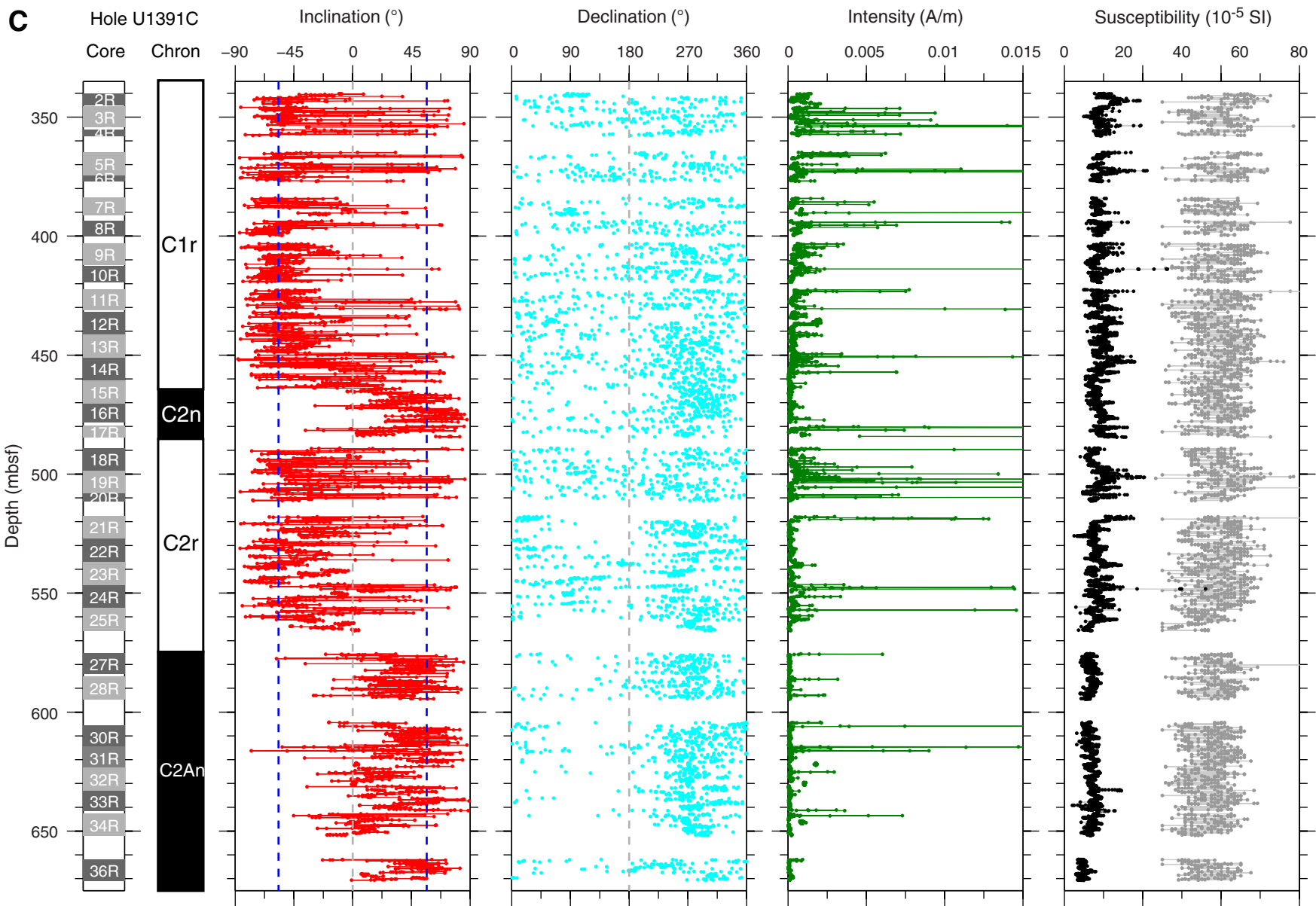


Figure F21. Plots of *P*-wave velocity (PWV) measured on the Whole Round Multisensor Logger (WRMSL; green line) and Section-Half Measurement Gantry (discrete samples) set to automatic (solid circles) and manual (open circles) mode, wet bulk density obtained on discrete samples (red diamonds), gamma ray attenuation density measured on the WRMSL (black lines), and magnetic susceptibility (MS) measured on the WRMSL (black lines) and on split cores (green points). Note that records were cleaned for outliers and bad data at sections ends. PP = physical property. A. Hole U1391A. (Continued on next page.)

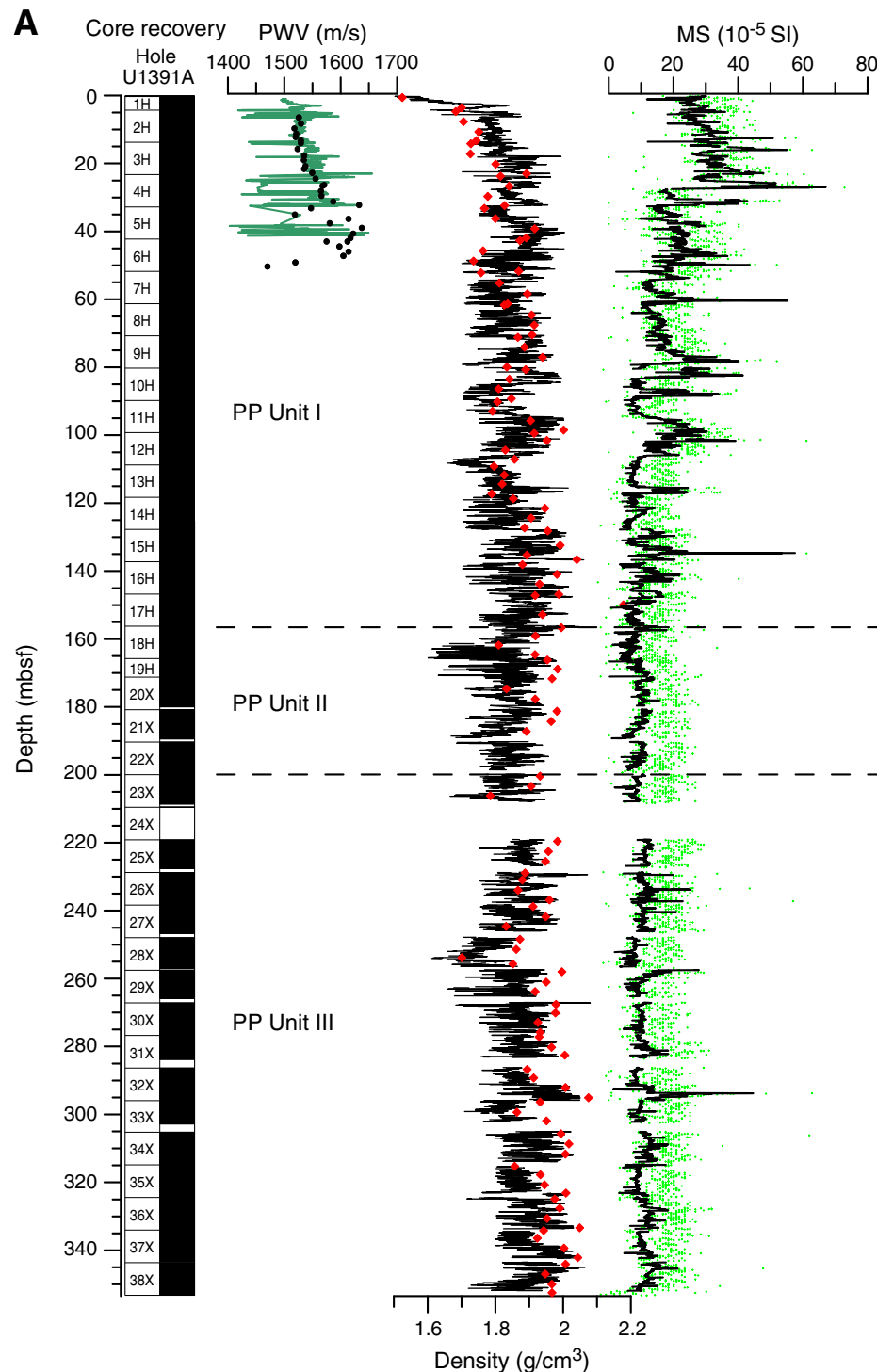


Figure F21 (continued). B. Hole U1391C.

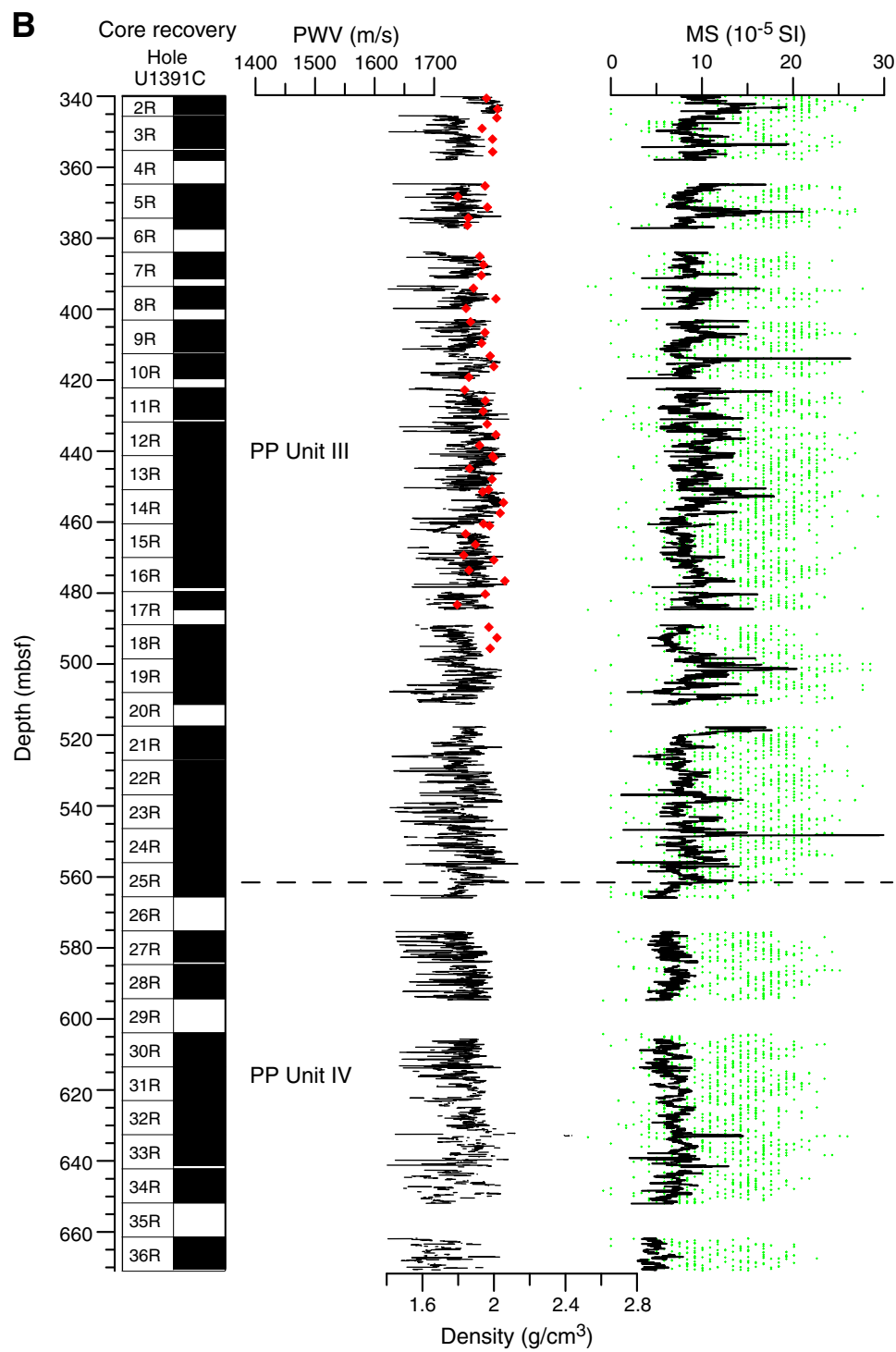


Figure F22. Plots of color reflectance (L^* , a^*) and natural gamma ray (NGR) measurements. Note that data were cleared for outliers and bad data at section ends. Reflectance data were smoothed with a 10-point running mean. PP = physical property. A. Hole U1391A. (Continued on next page.)

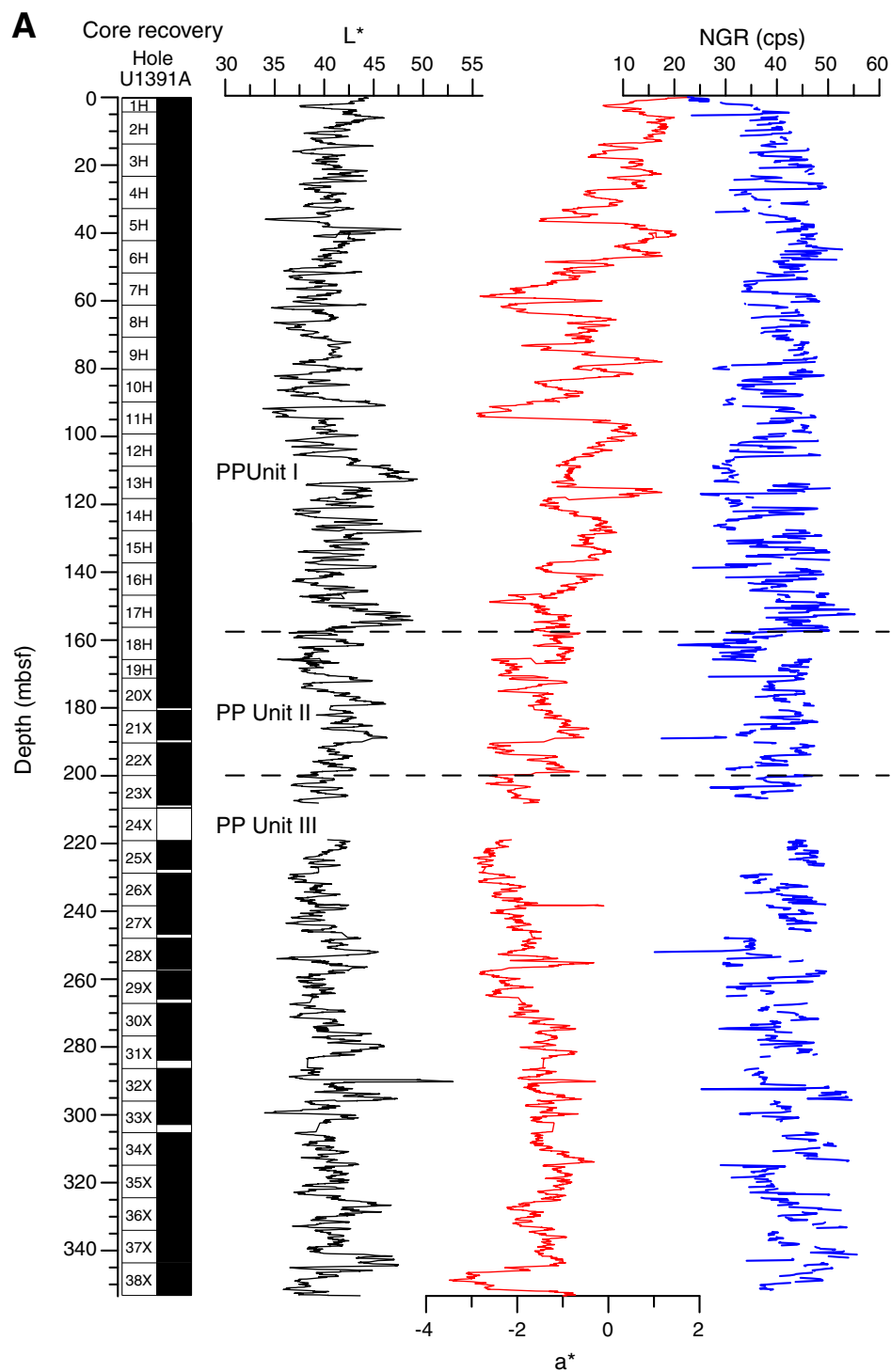


Figure F22 (continued). B. Hole U1391C.

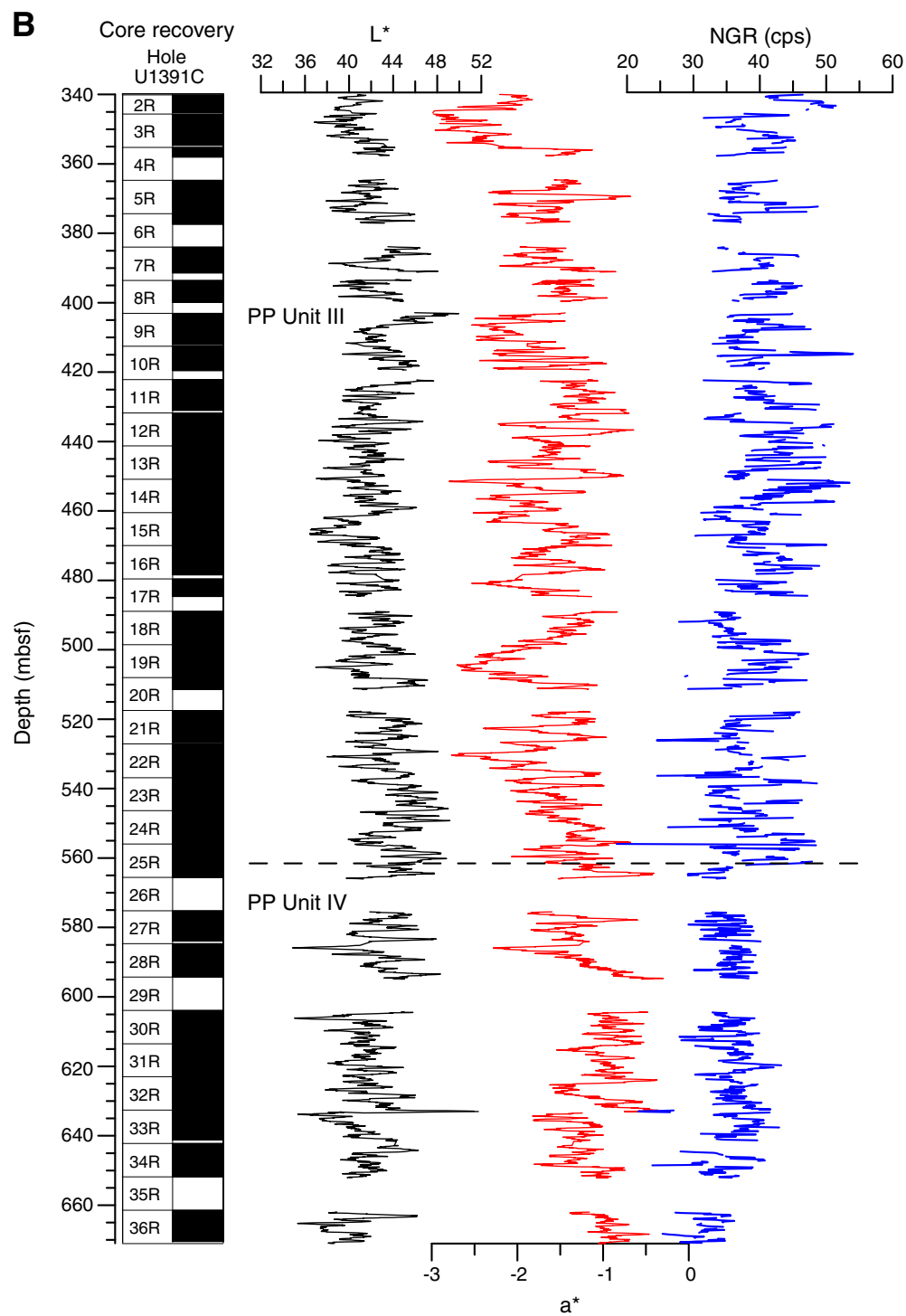


Figure F23. Plots of downhole distribution of discrete measurements of grain density, moisture content, and porosity. PP = physical property. A. Hole U1391A. (Continued on next page.)

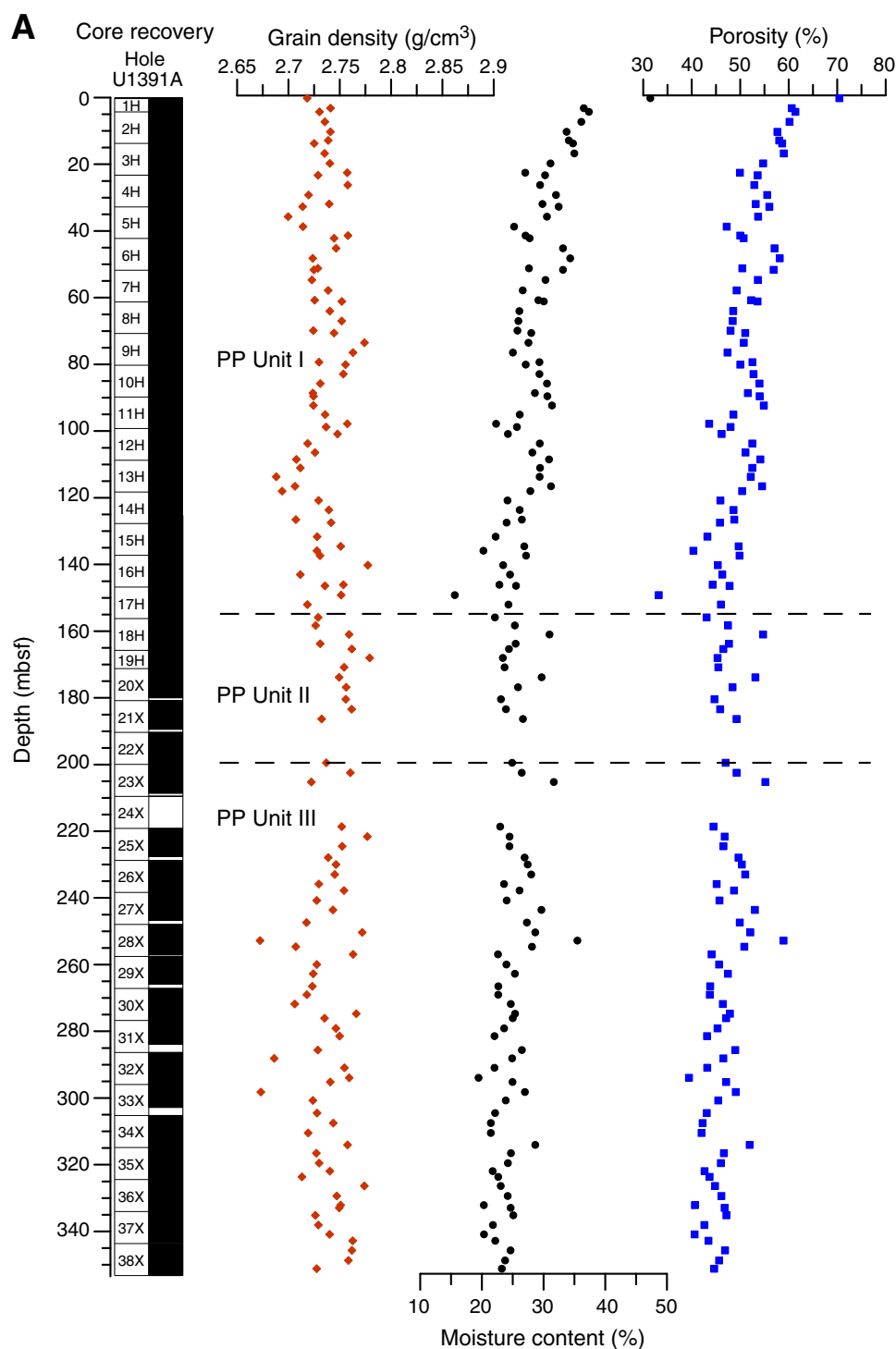


Figure F23 (continued). B. Hole U1391C.

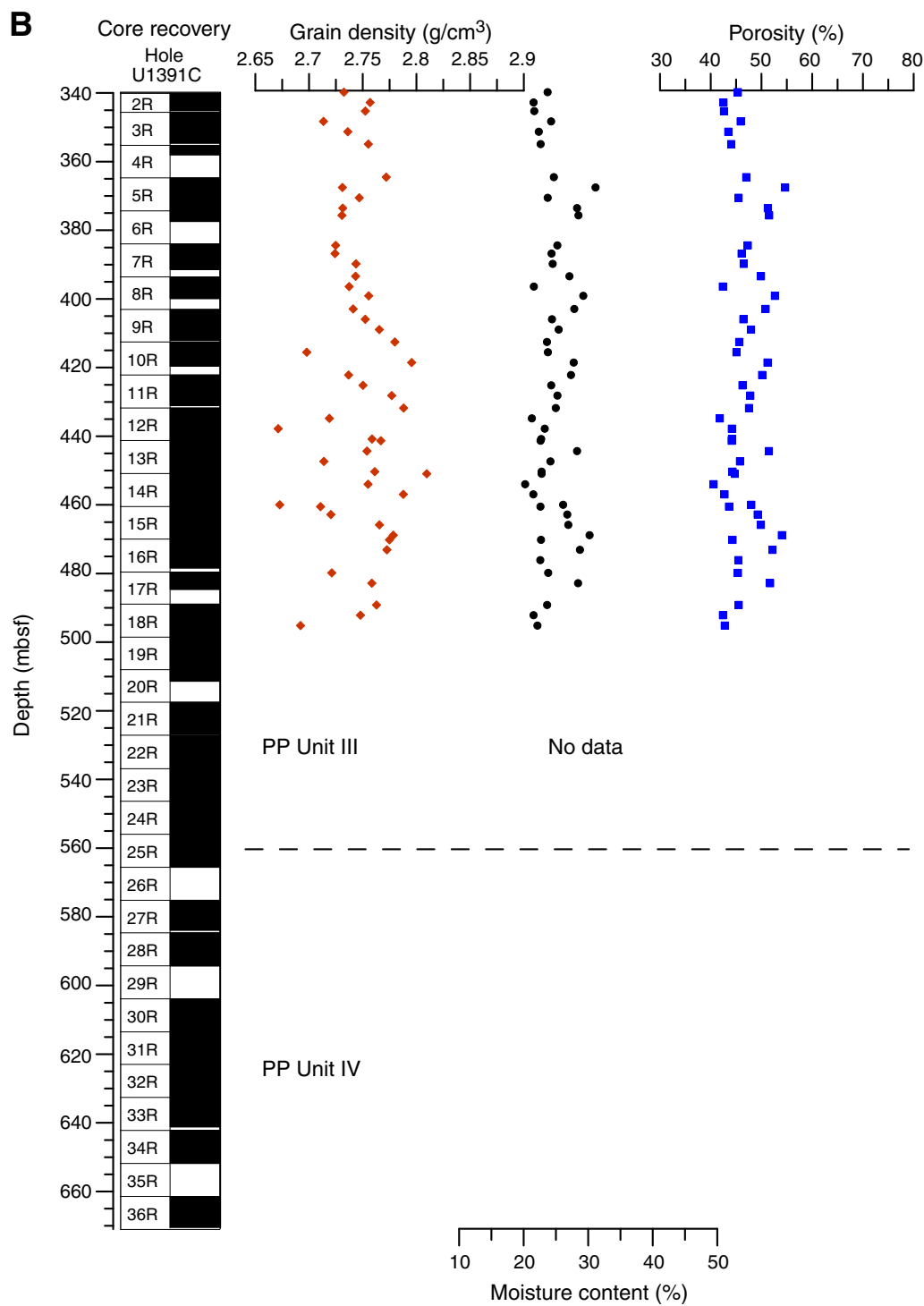


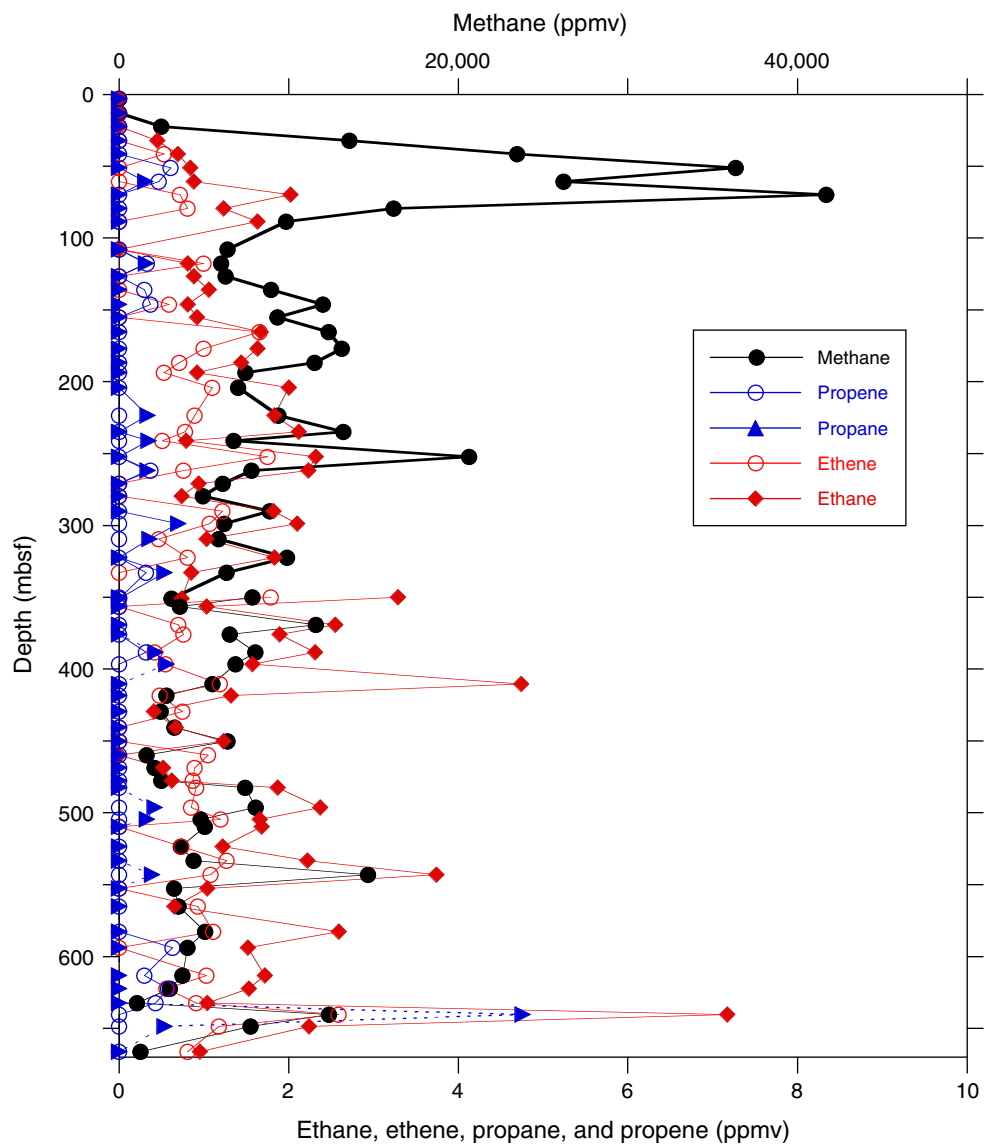
Figure F24. Plot of headspace gas analyses for volatile hydrocarbons, Holes U1391A and U1391C.

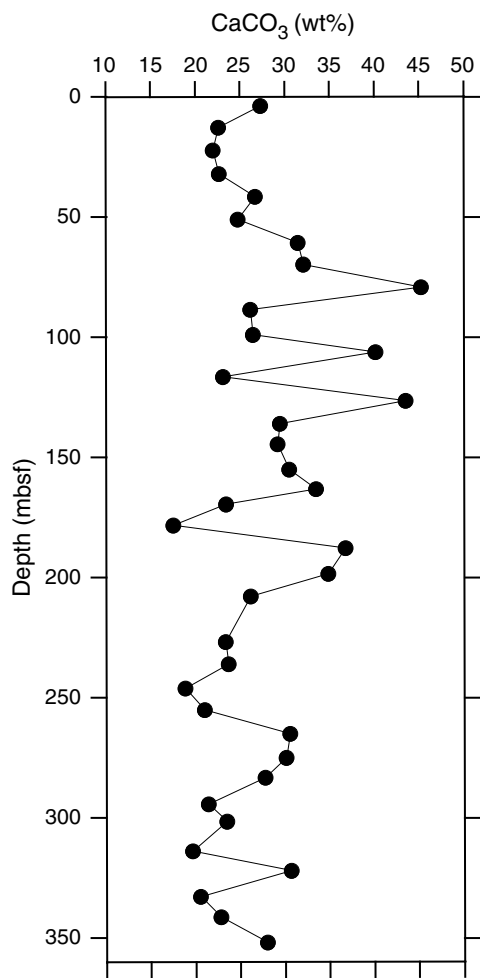
Figure F25. Plot of calcium carbonate, Hole U1391A.

Figure F26. A–C. Plots of calculated total organic carbon (TOC), total nitrogen (TN), and C/N ratio, Hole U1391A.

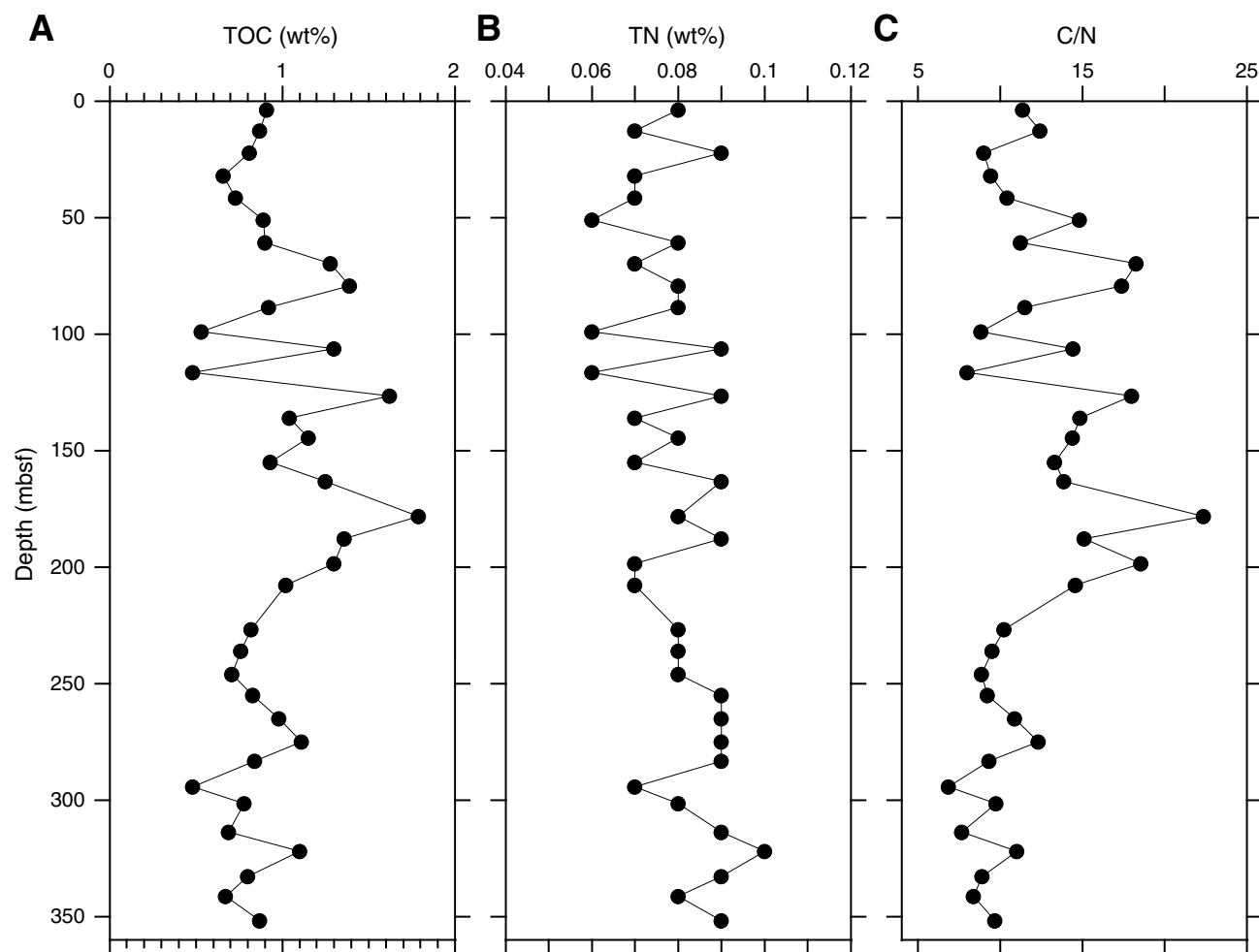


Figure F27. A–C. Plots of interstitial water sulfate, ammonium, and alkalinity, Site U1391.

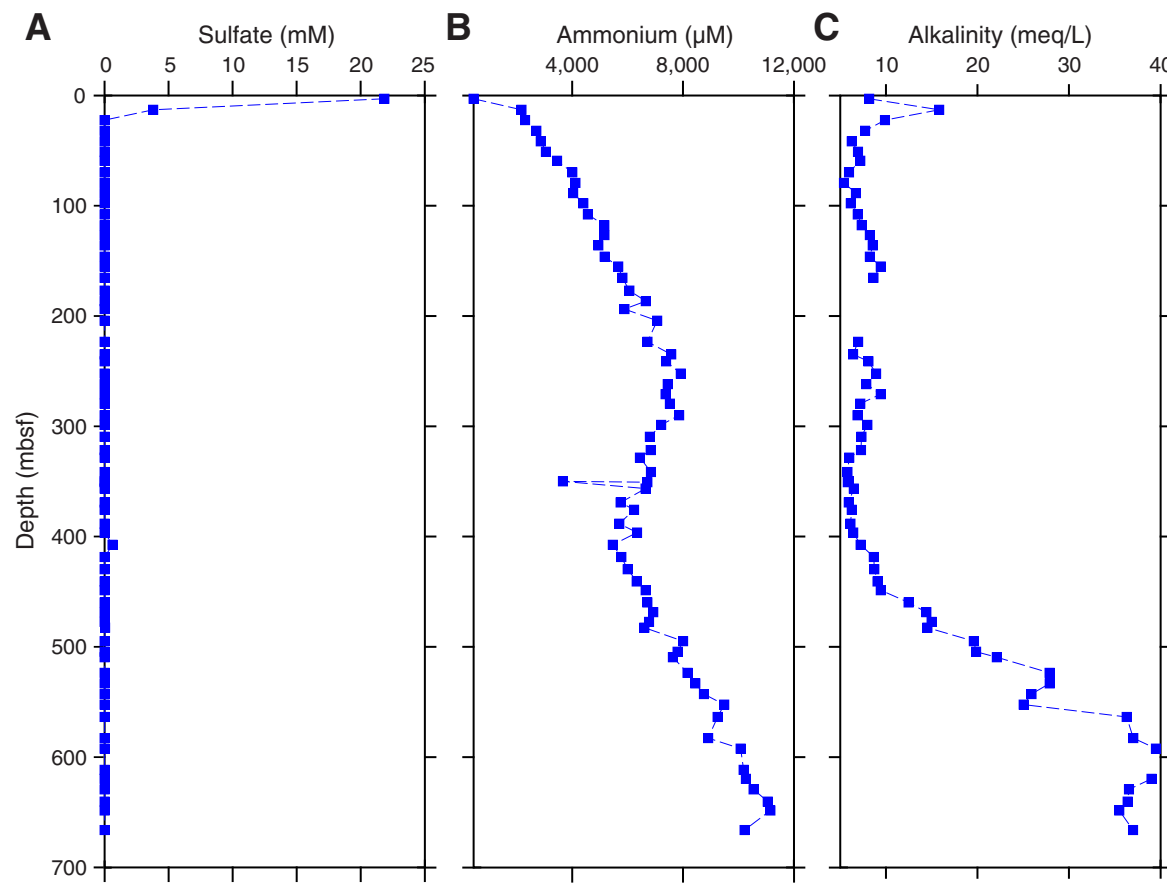


Figure F28. A–C. Plots of interstitial water calcium, magnesium, and potassium, Site U1391.

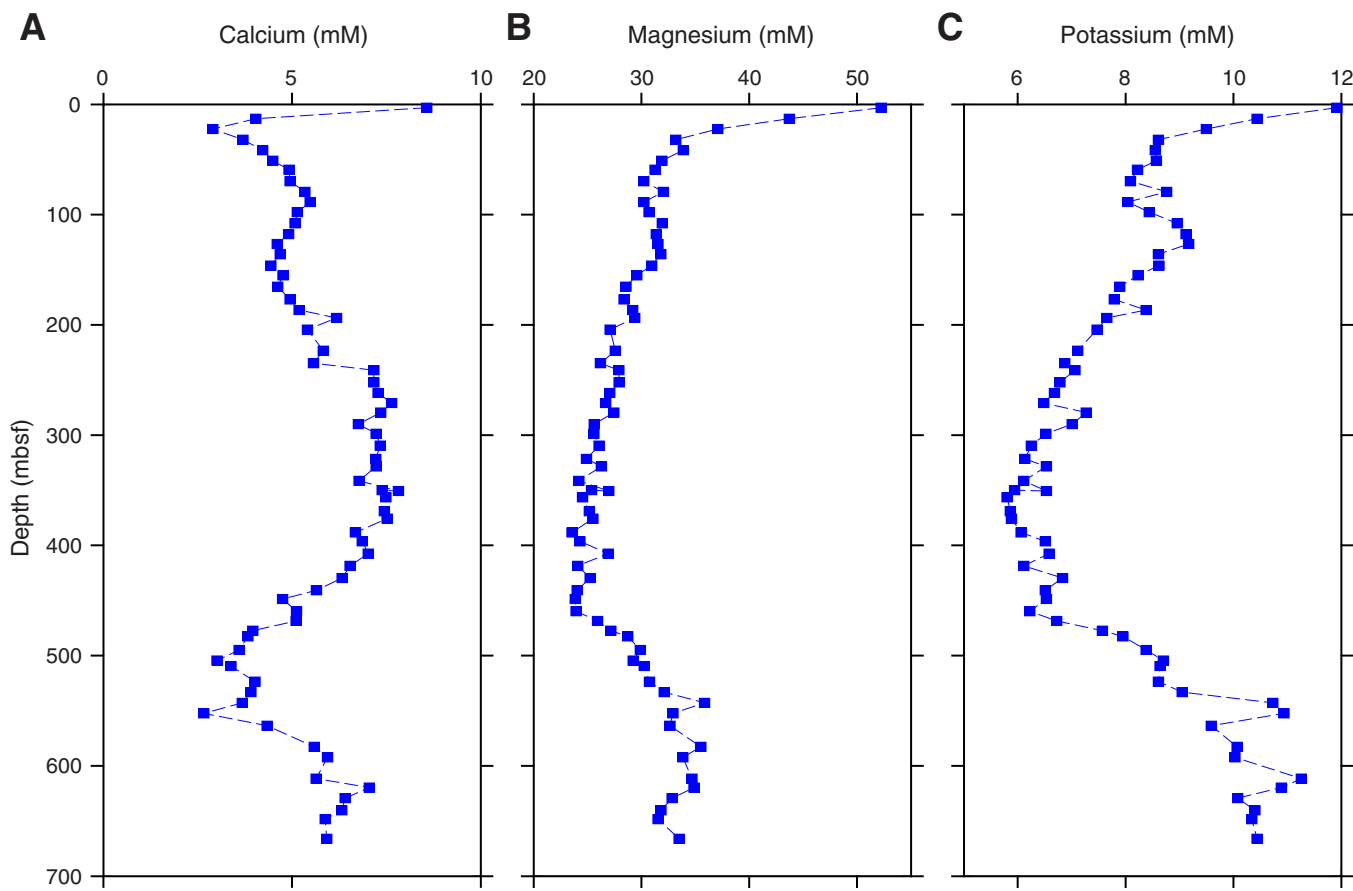


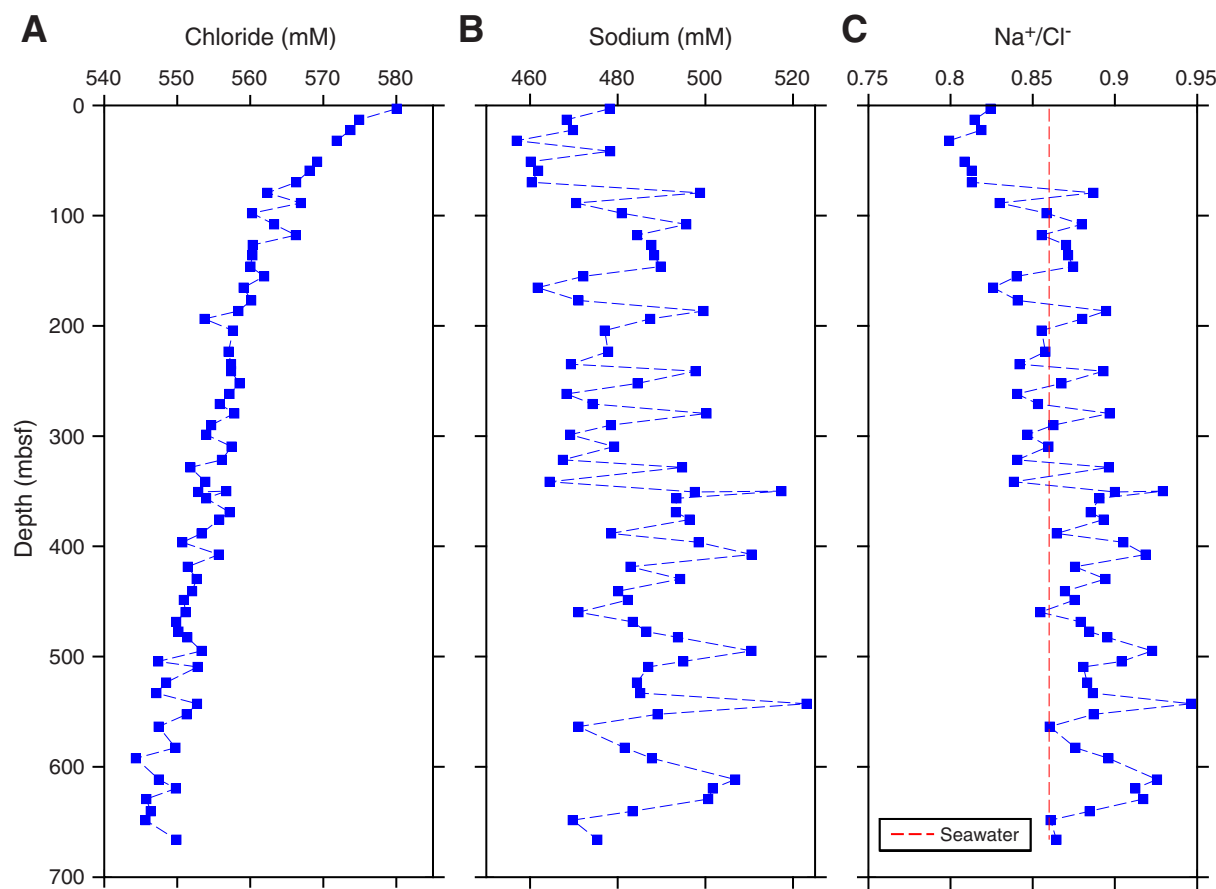
Figure F29. A–C. Plots of interstitial water chloride, sodium, and Na^+/Cl^- ratio, Site U1391.

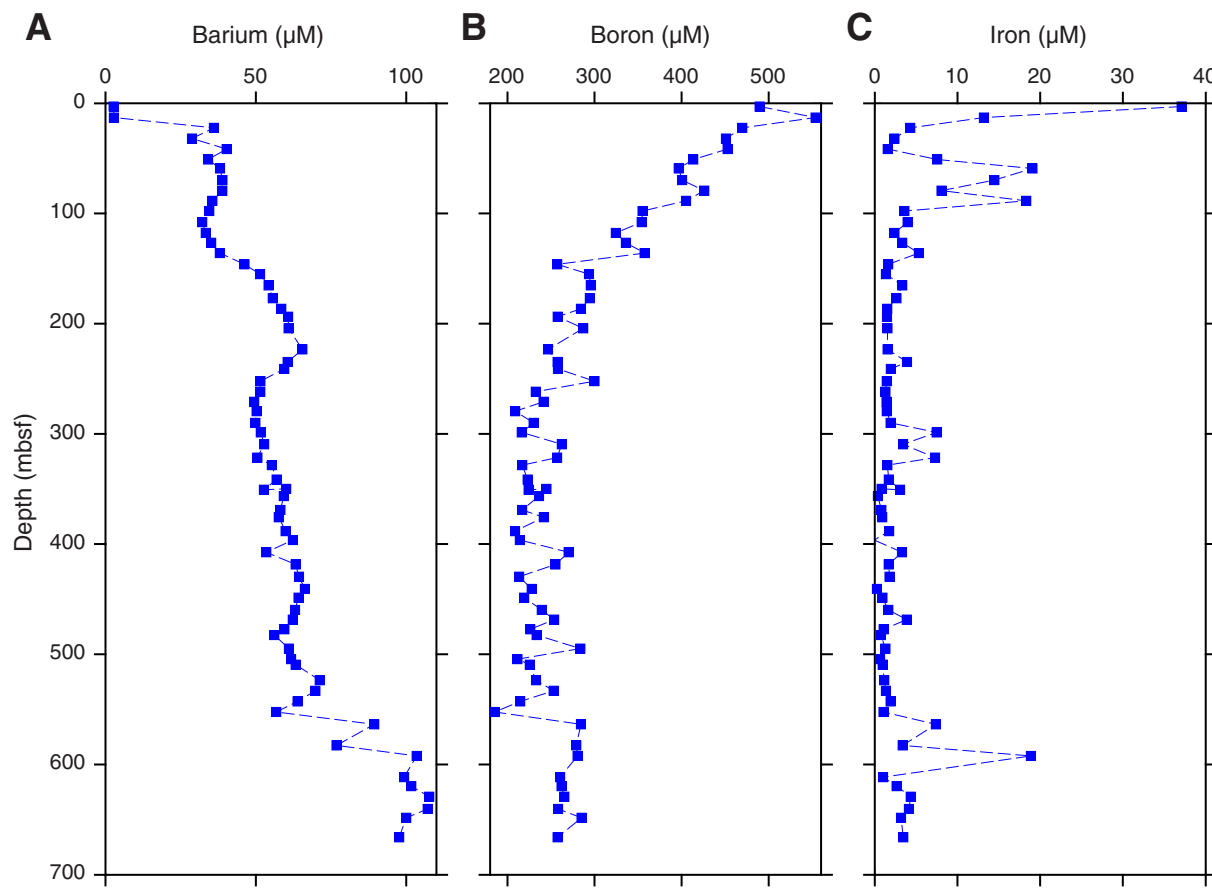
Figure F30. A–C. Plots of interstitial water barium, boron, and iron, Site U1391.

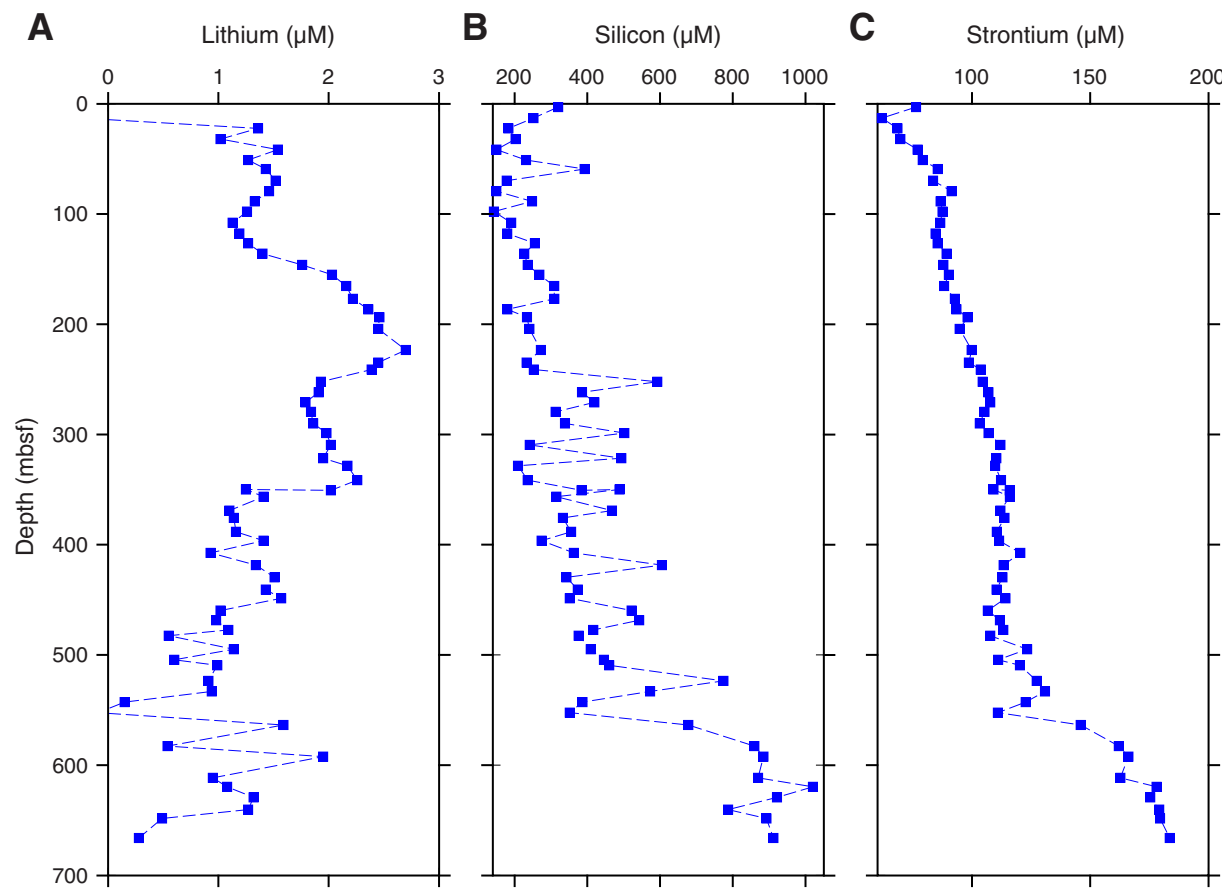
Figure F31. A–C. Plots of interstitial water lithium, silicon, and strontium, Site U1391.

Figure F32. Plots of interstitial water stable isotopes, Site U1391. VSMOW = Vienna standard mean ocean water.

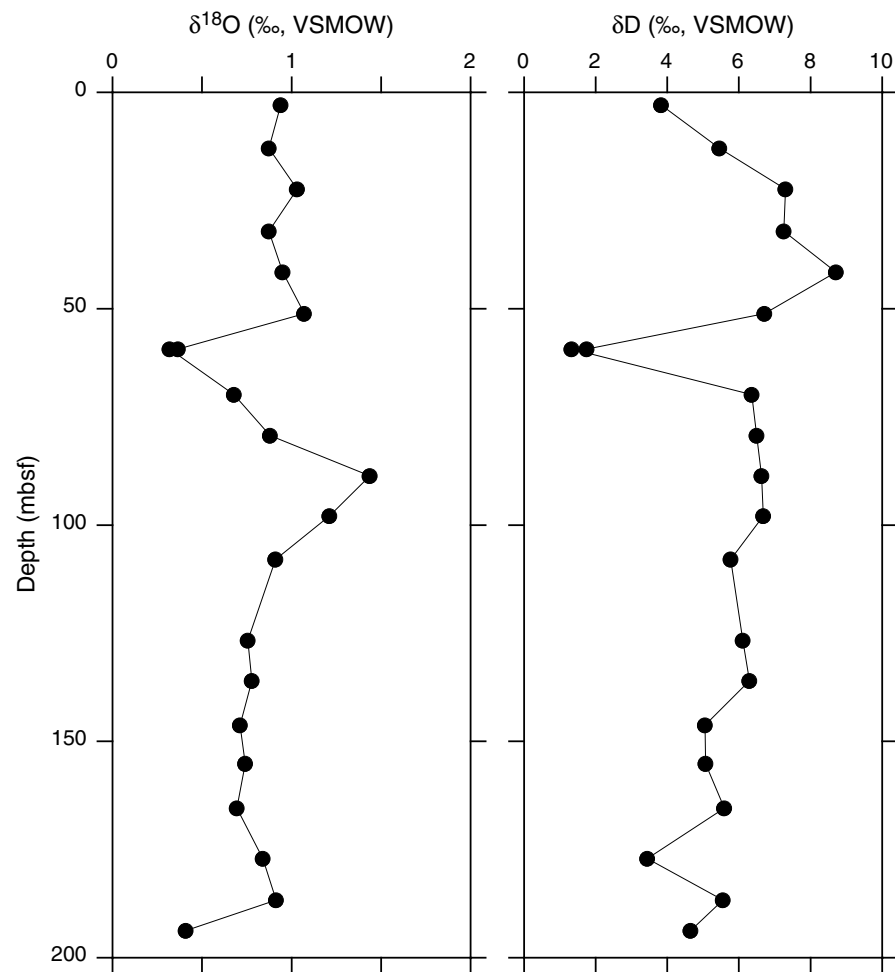


Figure F33. Plot of $\delta^{18}\text{O}$ vs. δD , Site U1391. VSMOW = Vienna standard mean ocean water.

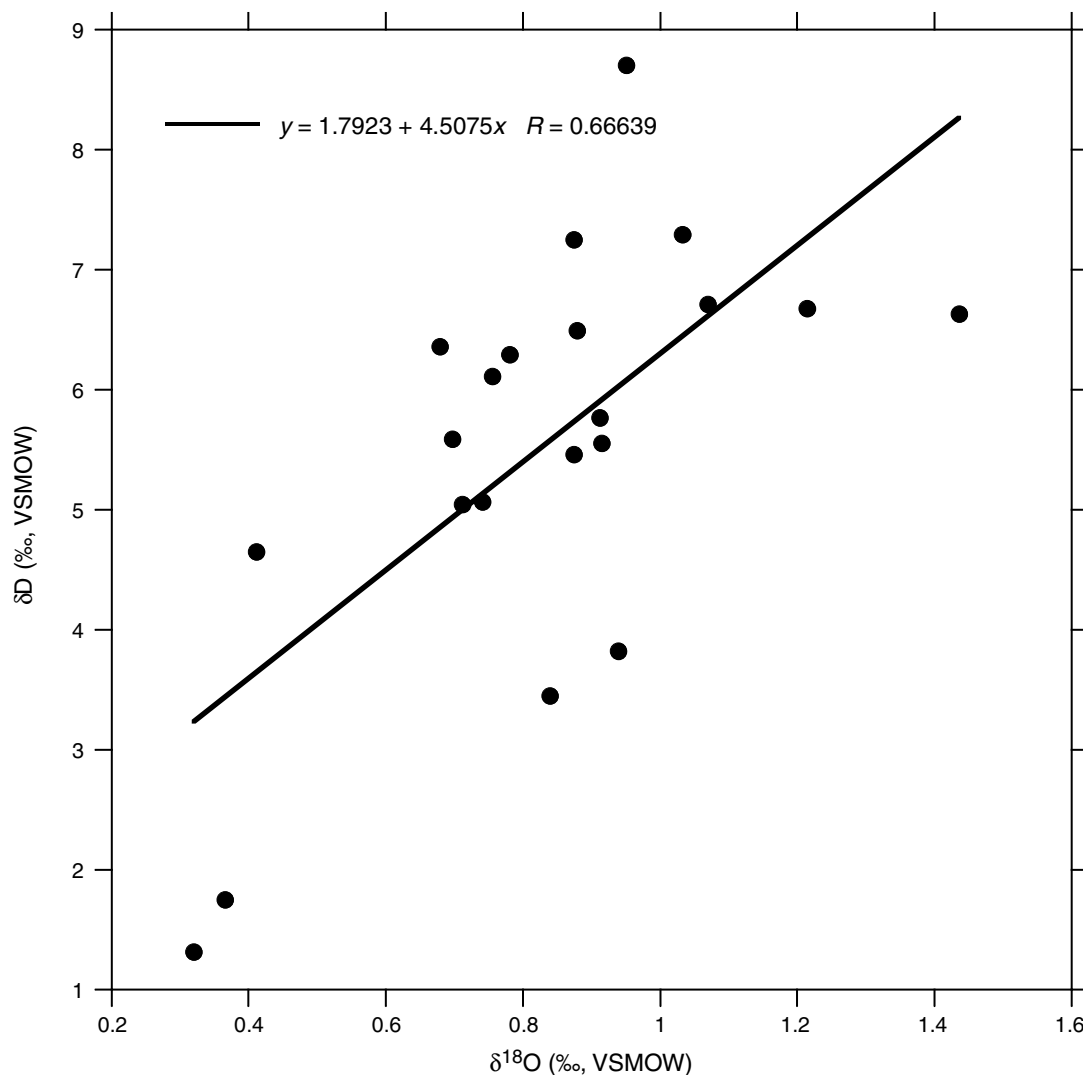


Figure F34. Logging operations summary diagram, Hole U1391C. FMS = Formation MicroScanner.

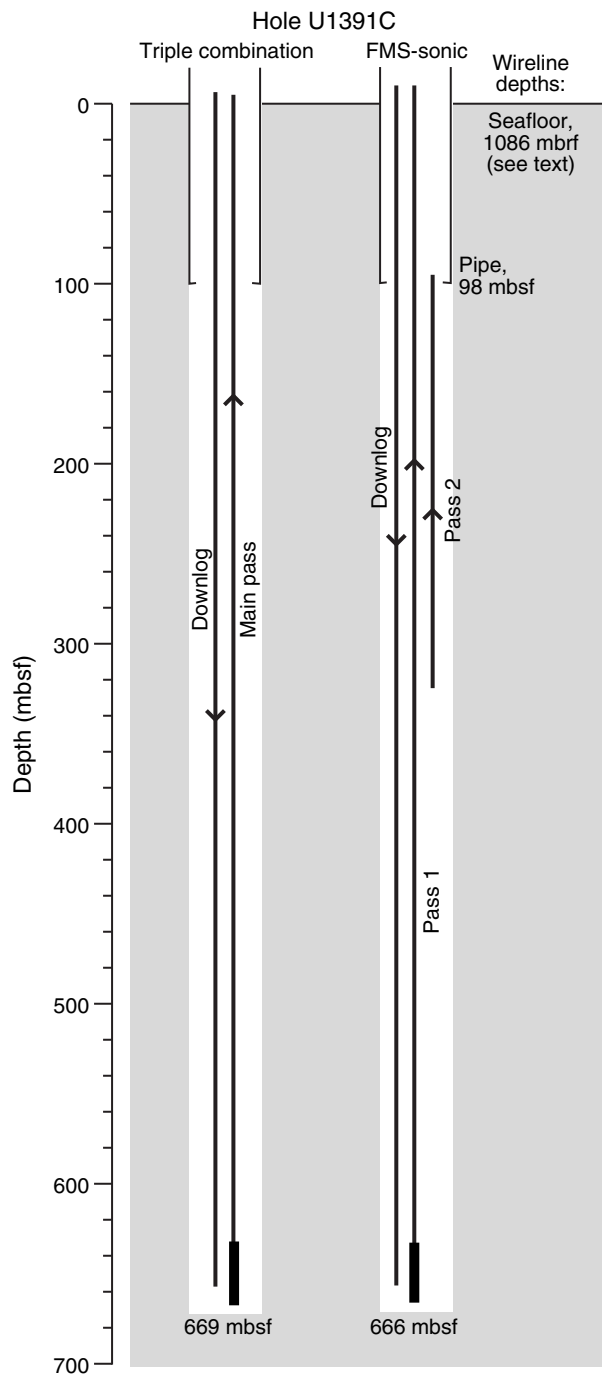


Figure F35. Plots of tides and ship heave, Site U1391. Tides were calculated using Tide Model Driver, a Matlab front-end for the Oregon State University Tidal Data Inversion (Egbert and Erofeeva, 2002). Ship heave was derived from acceleration measured by the motion reference unit in the moon pool area. FMS = Formation Micro-Scanner, APCT-3 = advanced piston corer temperature tool. RMS = root-mean square.

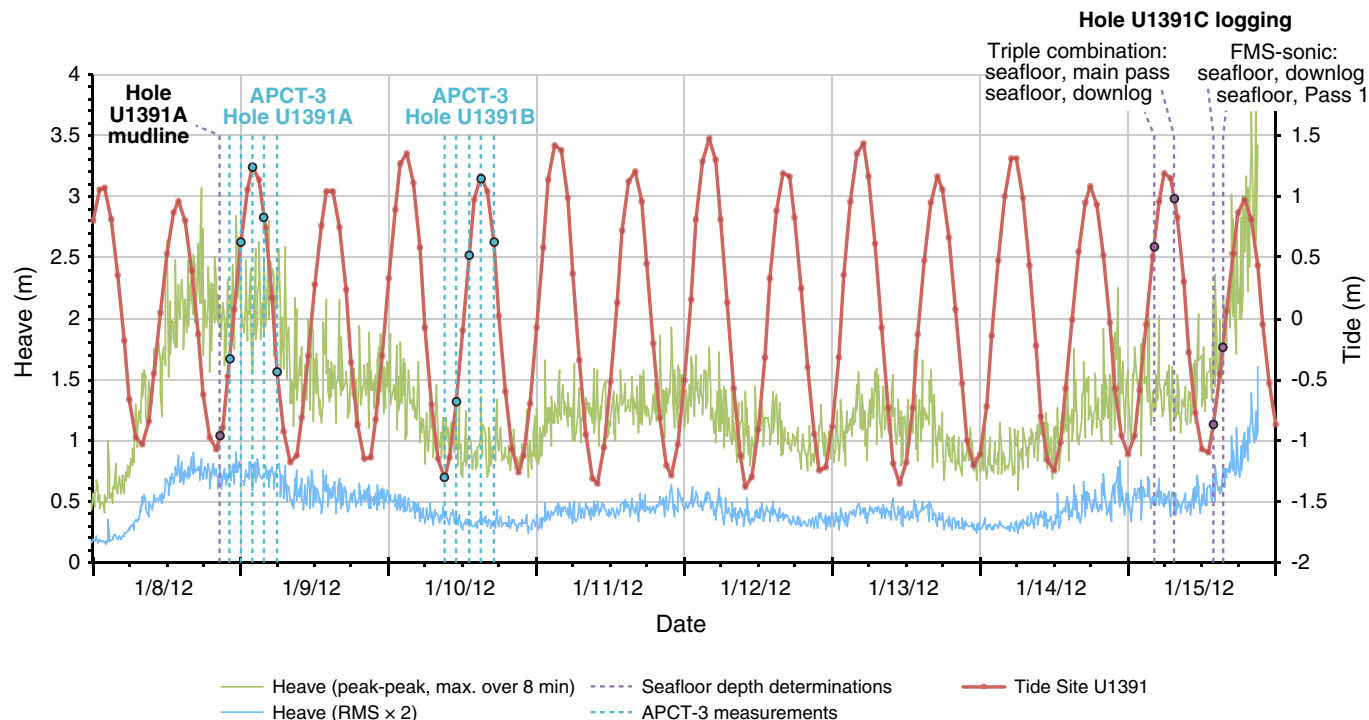


Figure F36. Downhole logs, lithologic units, and logging units, Hole U1391C. HSGR = standard (total) gamma radiation, NGR = natural gamma radiation, MAD = moisture and density, RHOM = bulk density, RLA5 = apparent resistivity from computed focusing mode 5, PWL = *P*-wave logger.

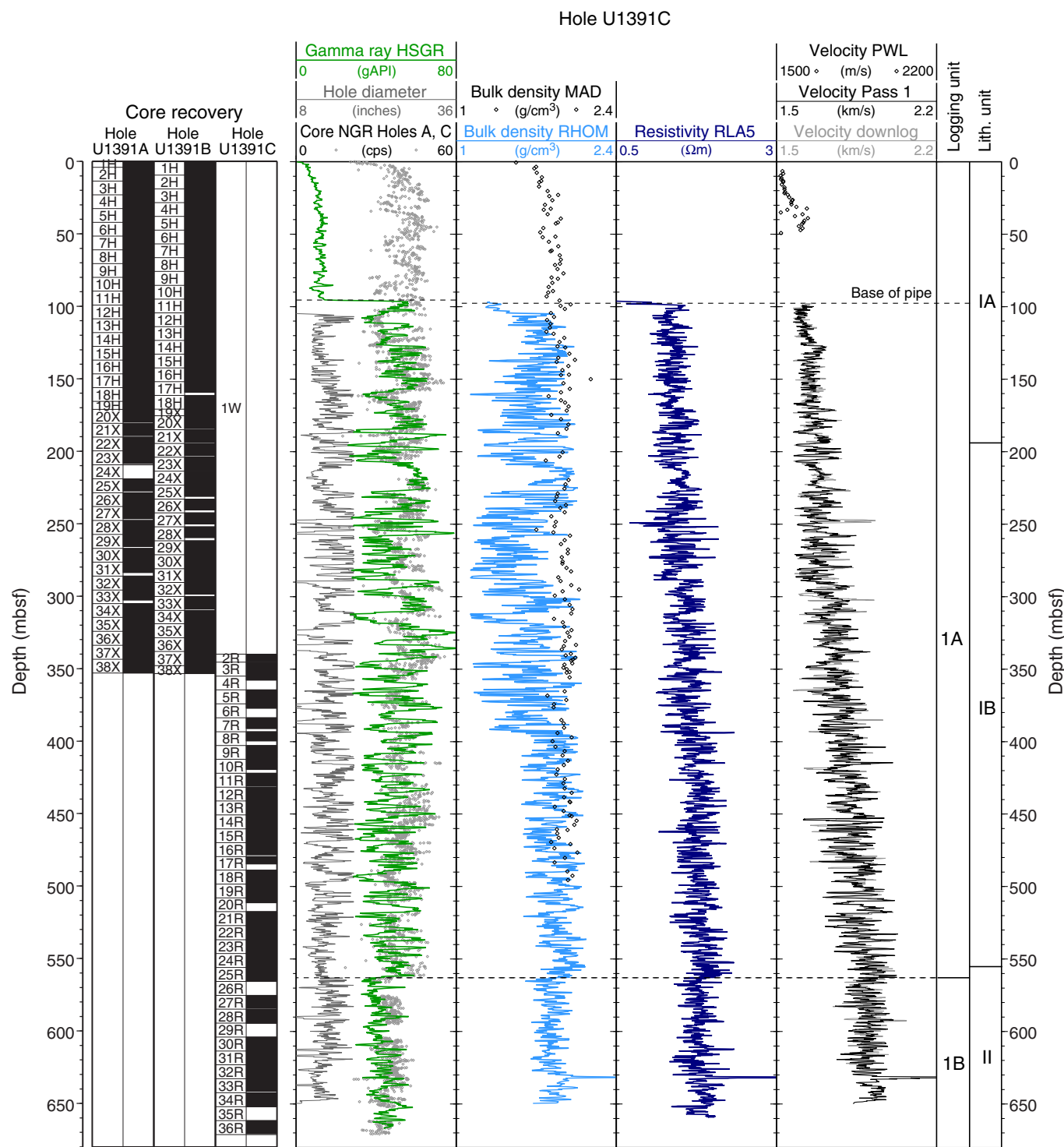


Figure F37. Natural gamma radiation (NGR) logs, lithologic units, and logging units, Hole U1391C. HSGR = standard (total) gamma radiation.

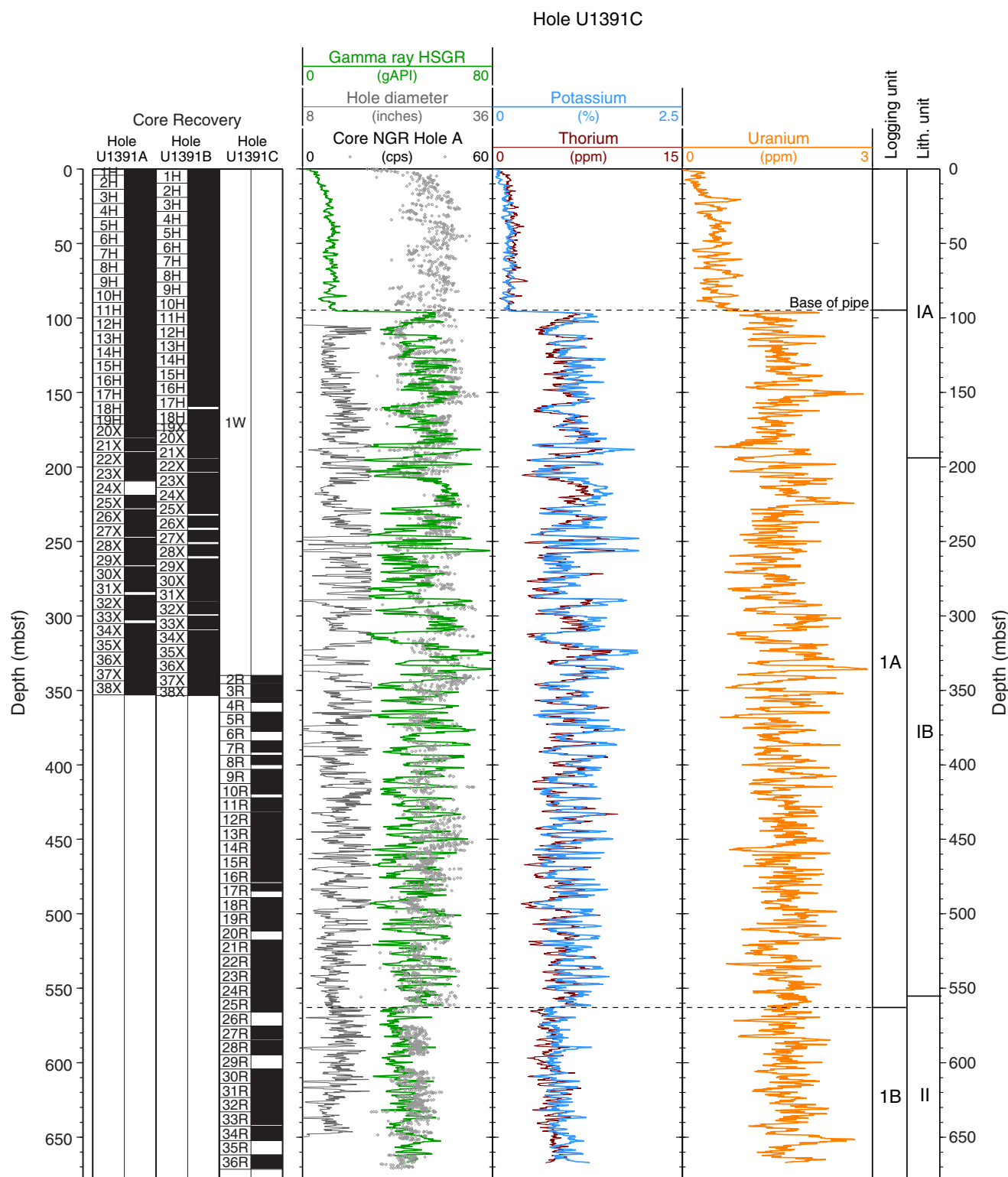


Figure F38. Plot of advanced piston corer temperature tool (APCT-3) temperature-time series with extrapolated formation temperature estimates, Site U1391. APC = advanced piston corer.

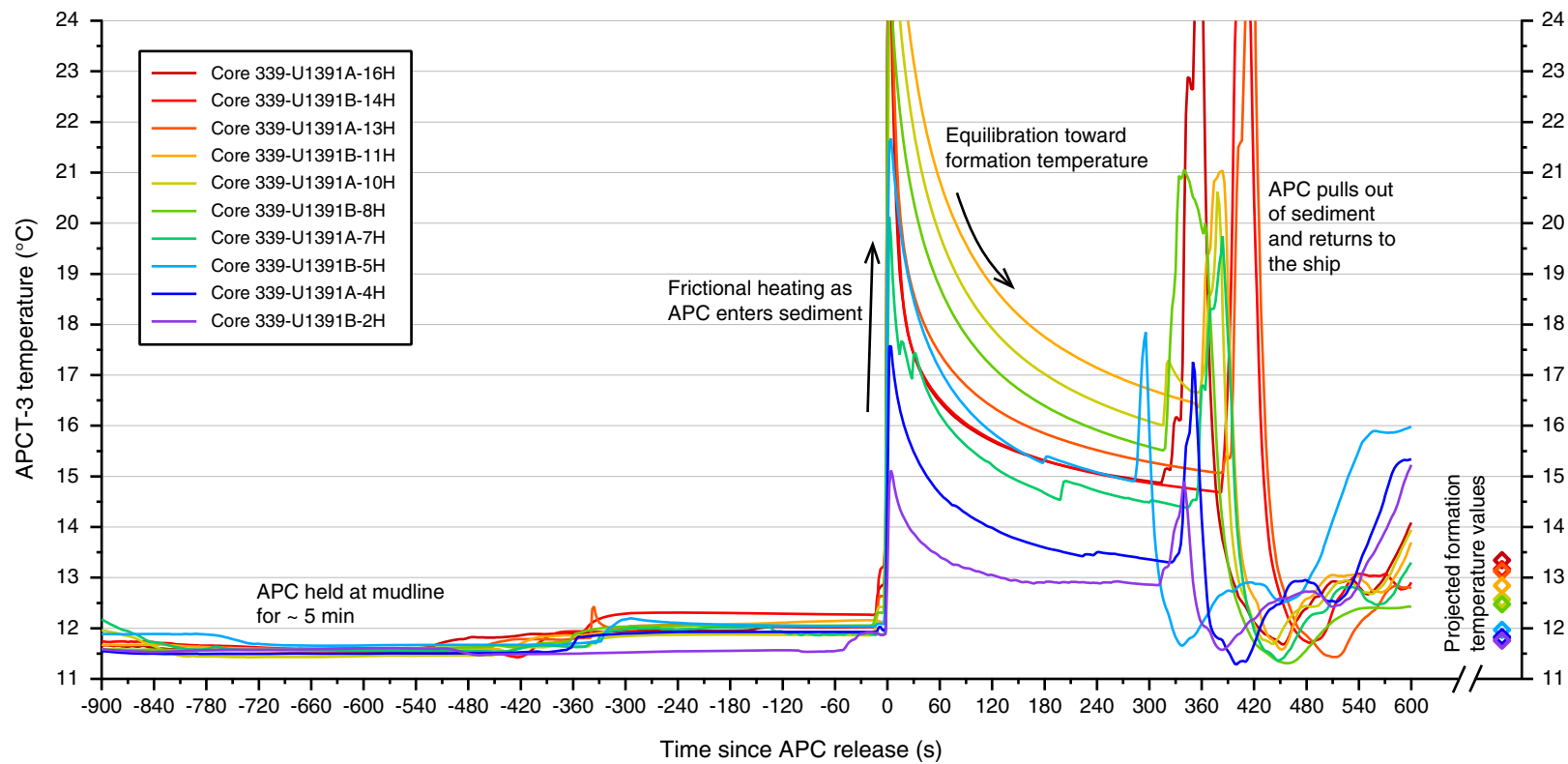


Figure F39. Plots of heat flow calculations, Site U1391. A. Sediment temperatures in Holes U1391A and U1391B (squares). B. Thermal conductivity data from Hole U1391C (circles) with calculated thermal resistance (solid line). C. Bullard plot of heat flow calculated from a linear fit of the temperature data.

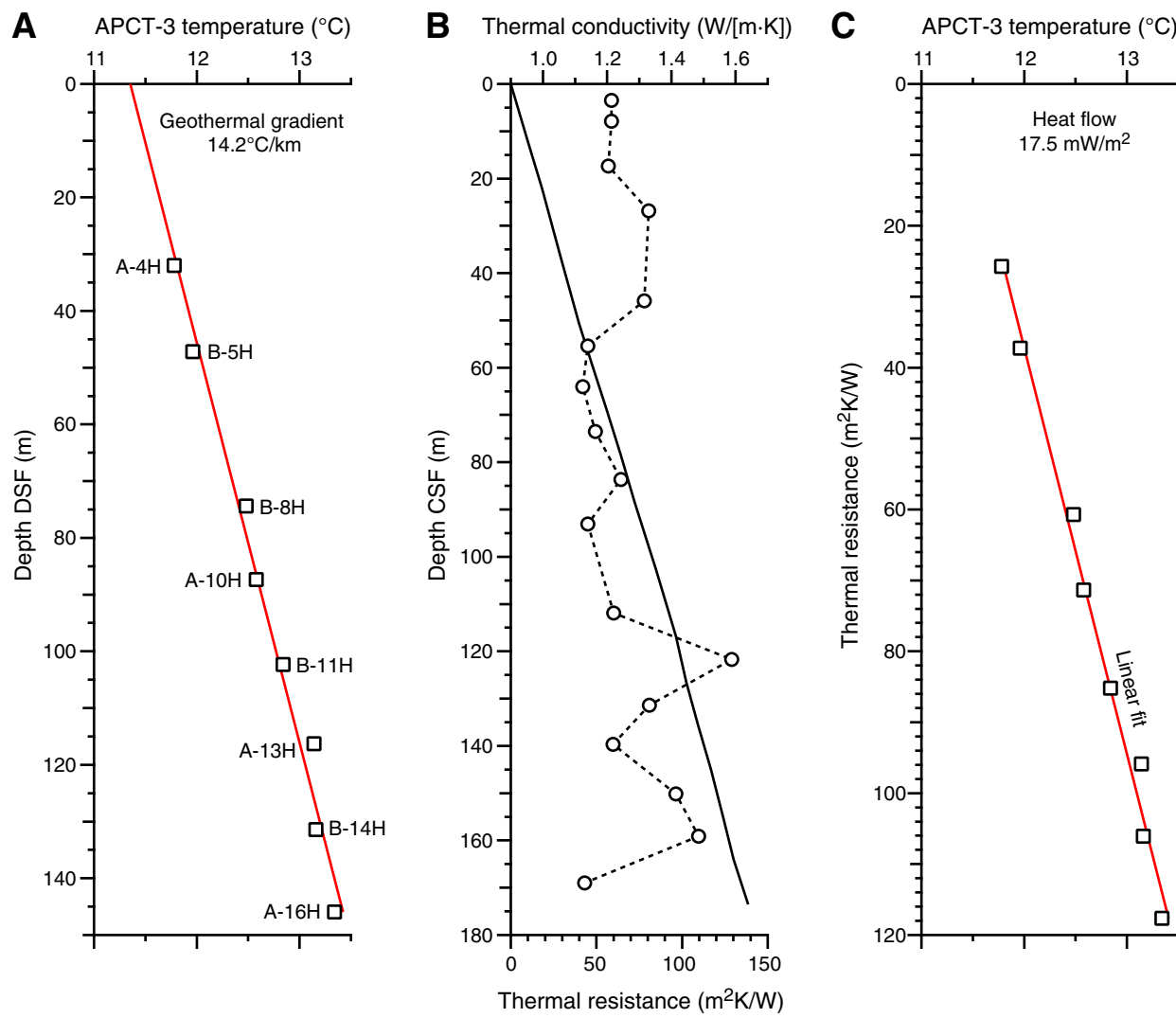


Figure F40. Plots of magnetic susceptibility vs. composite depth, Site U1391. In the lower panel, susceptibility values for Holes U1391B and U1391C are shifted for display purposes. A. 0–40 mcd. (Continued on next 10 pages.)

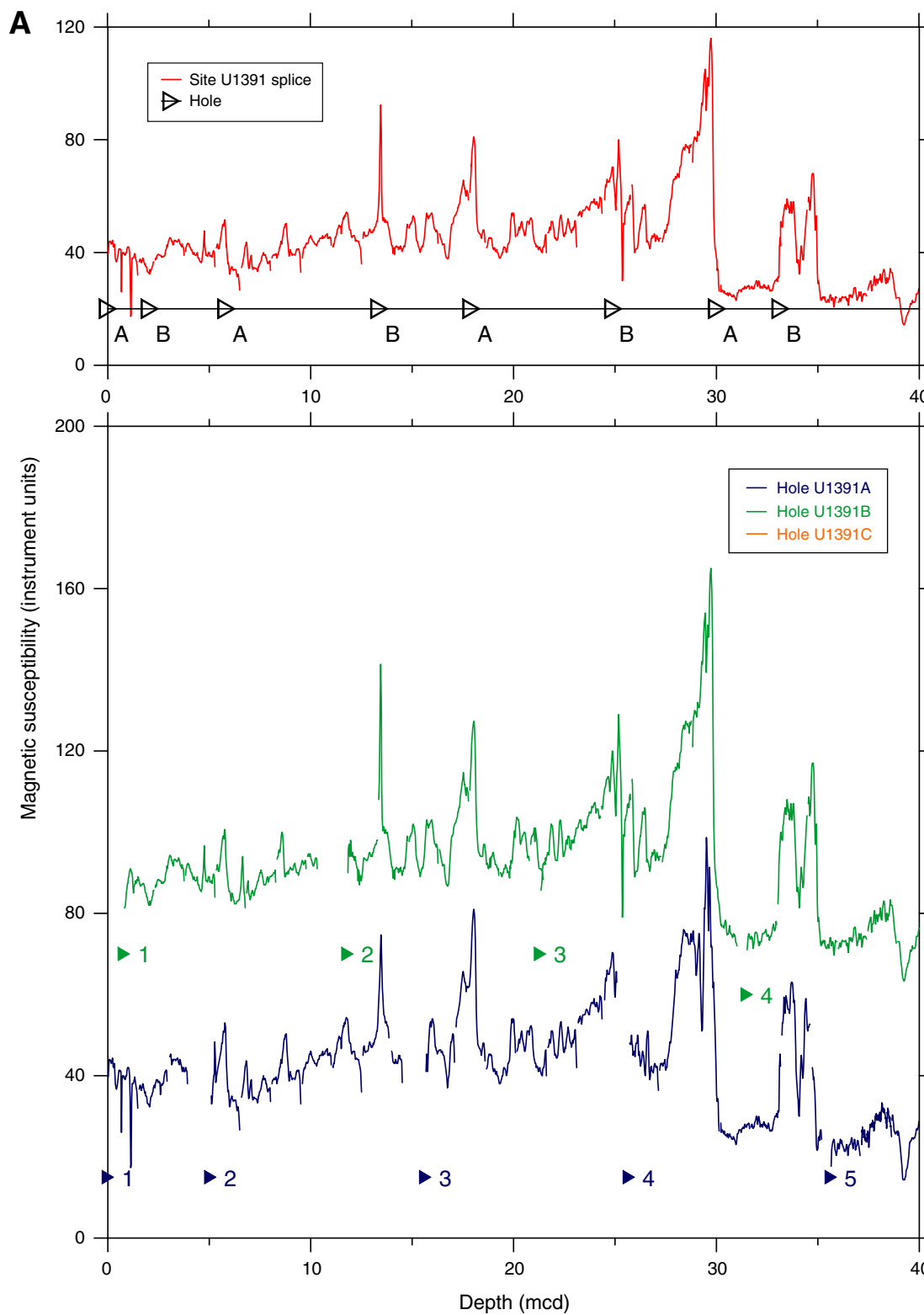


Figure F40 (continued). B. 40–80 mcd. (Continued on next page.)

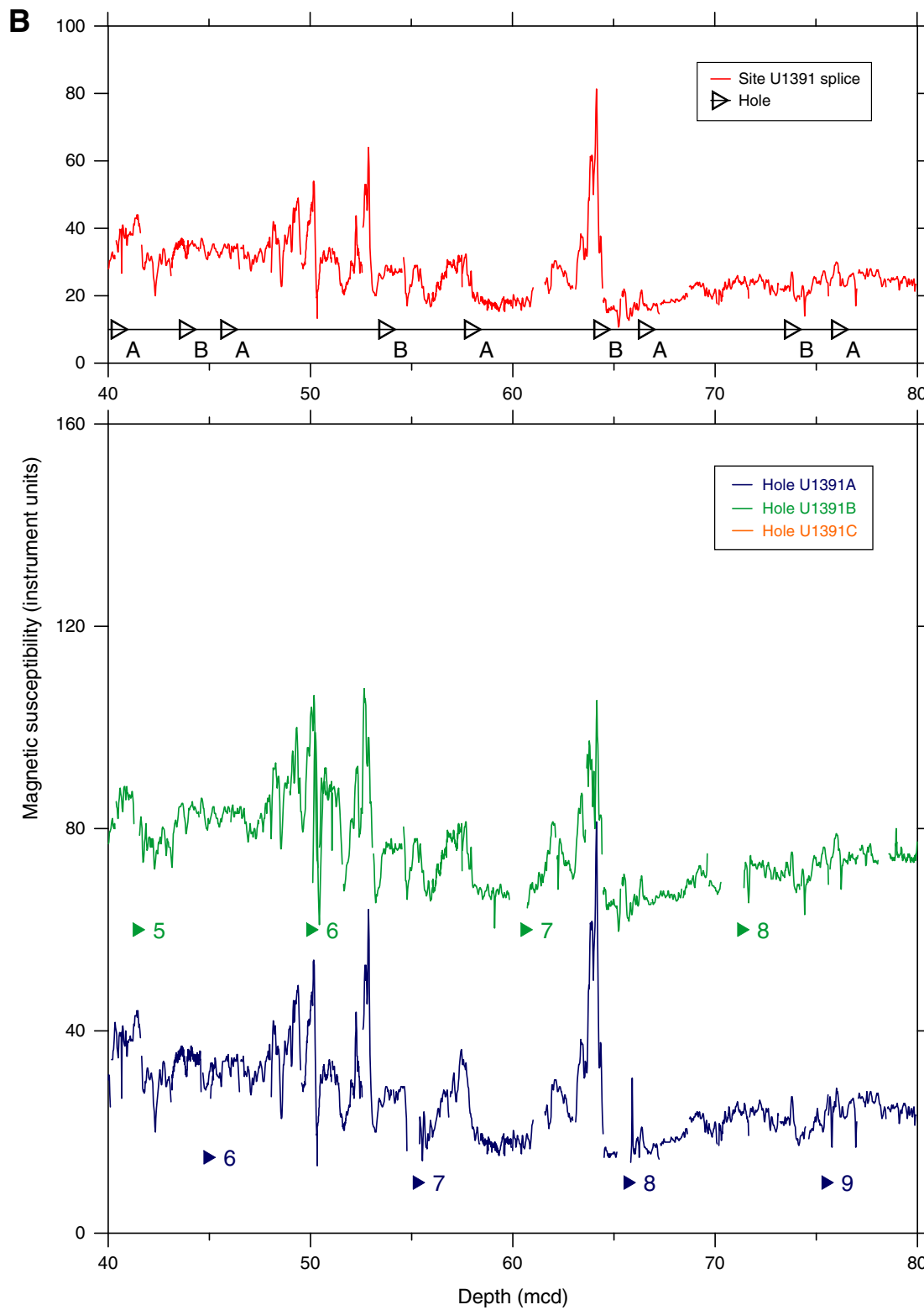


Figure F40 (continued). C. 80–120 mcd. (Continued on next page.)

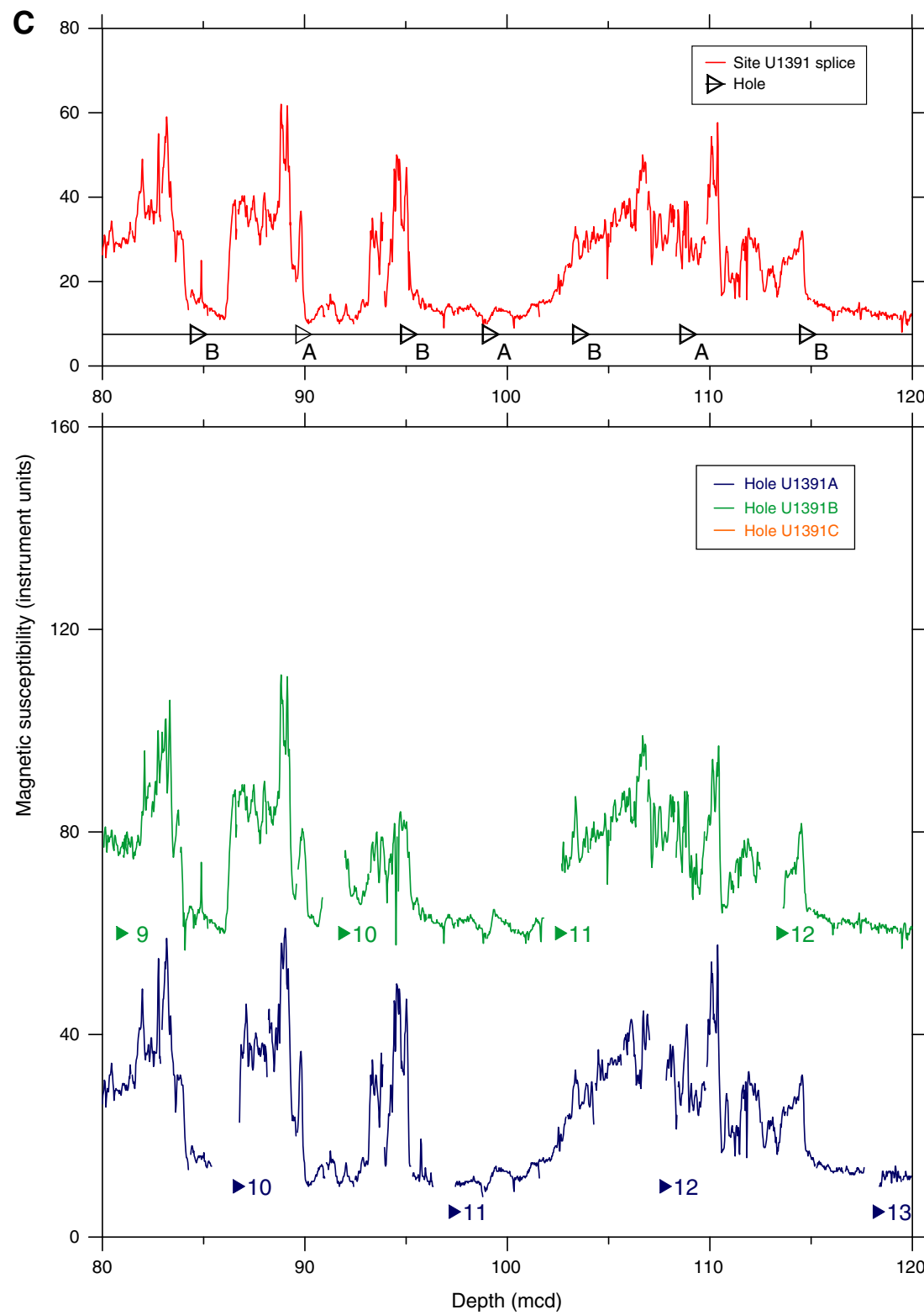


Figure F40 (continued). D. 120–160 mcd. (Continued on next page.)

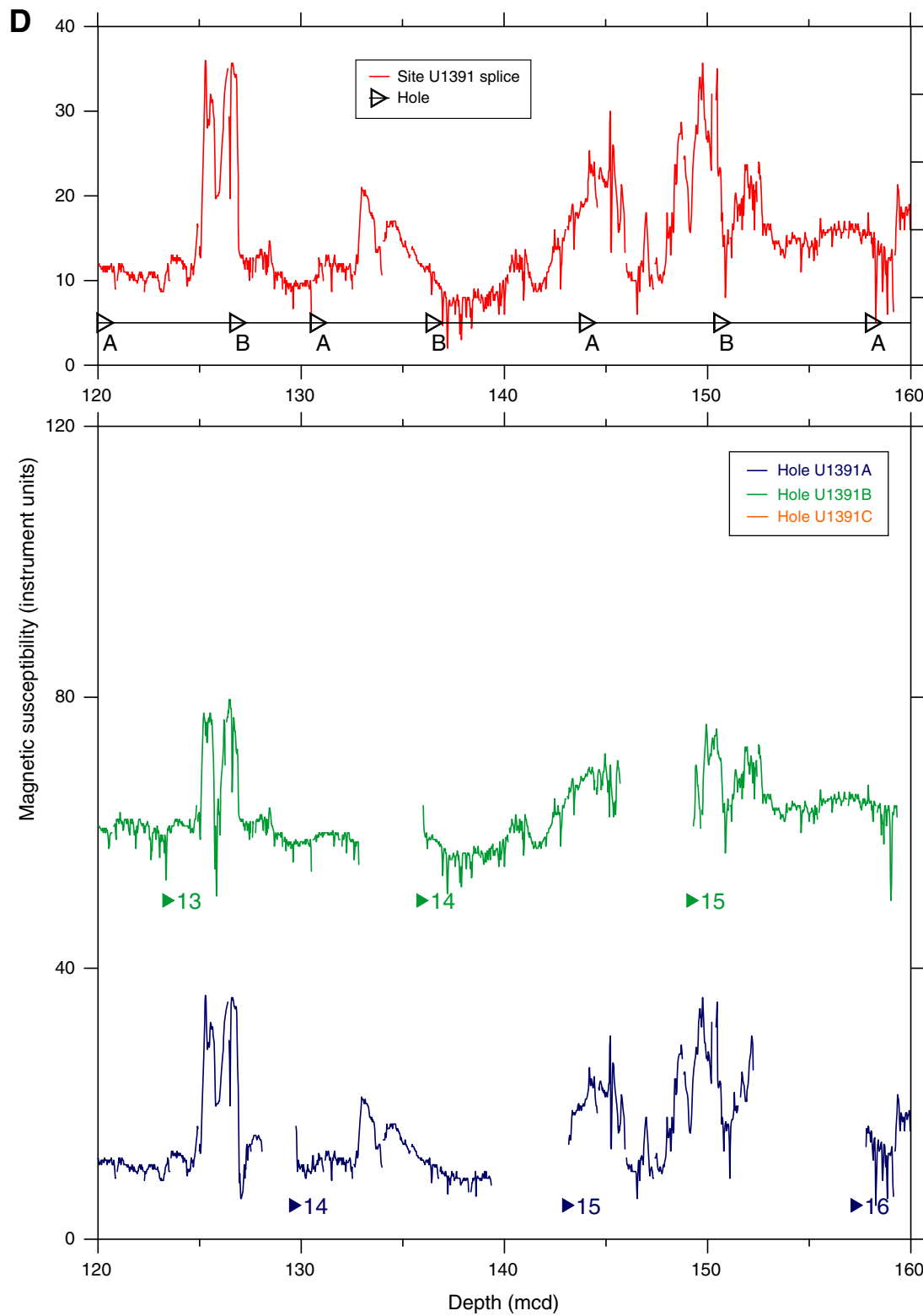


Figure F40 (continued). E. 160–200 mcd. (Continued on next page.)

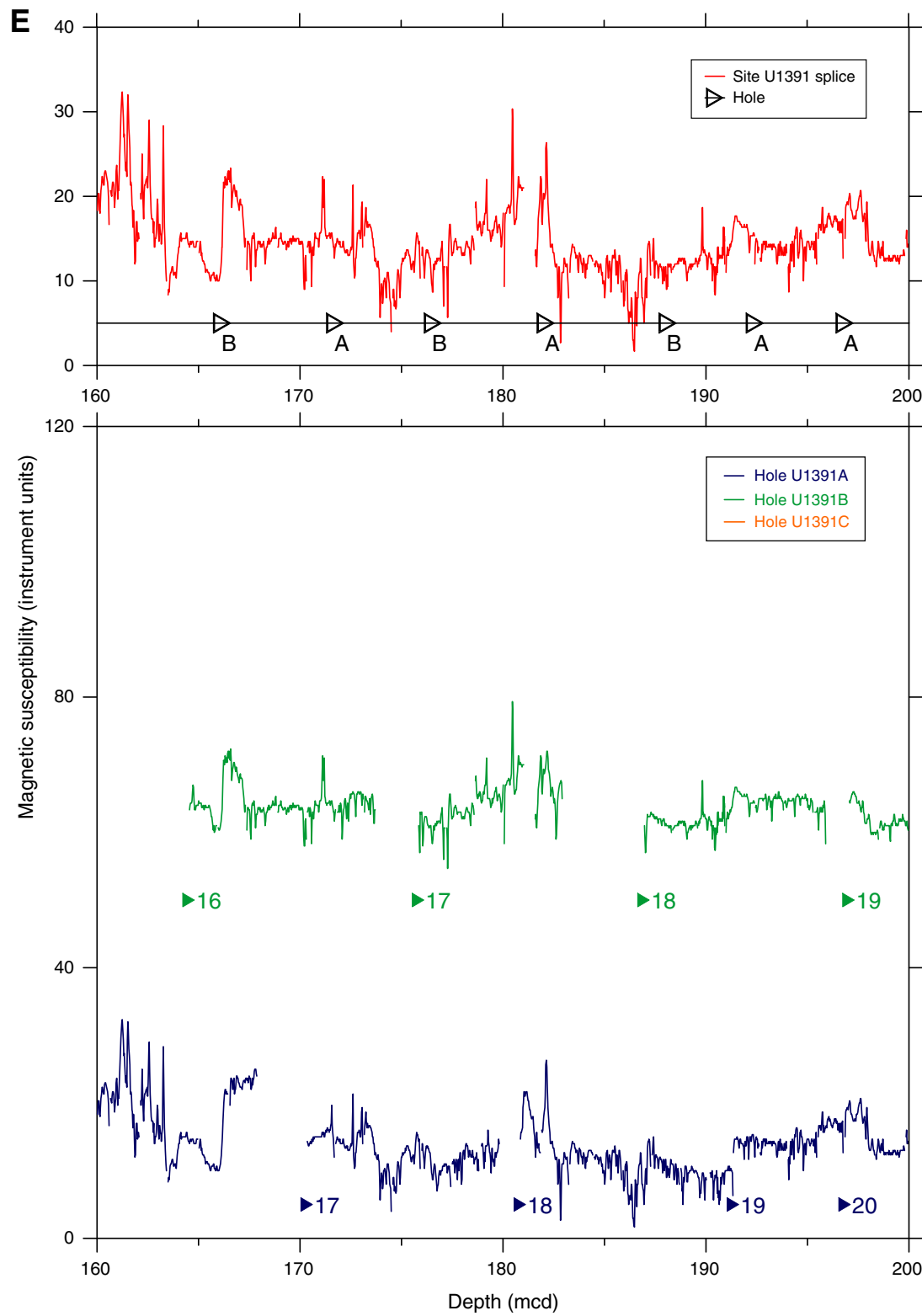


Figure F40 (continued). F. 200–240 mcd. (Continued on next page.)

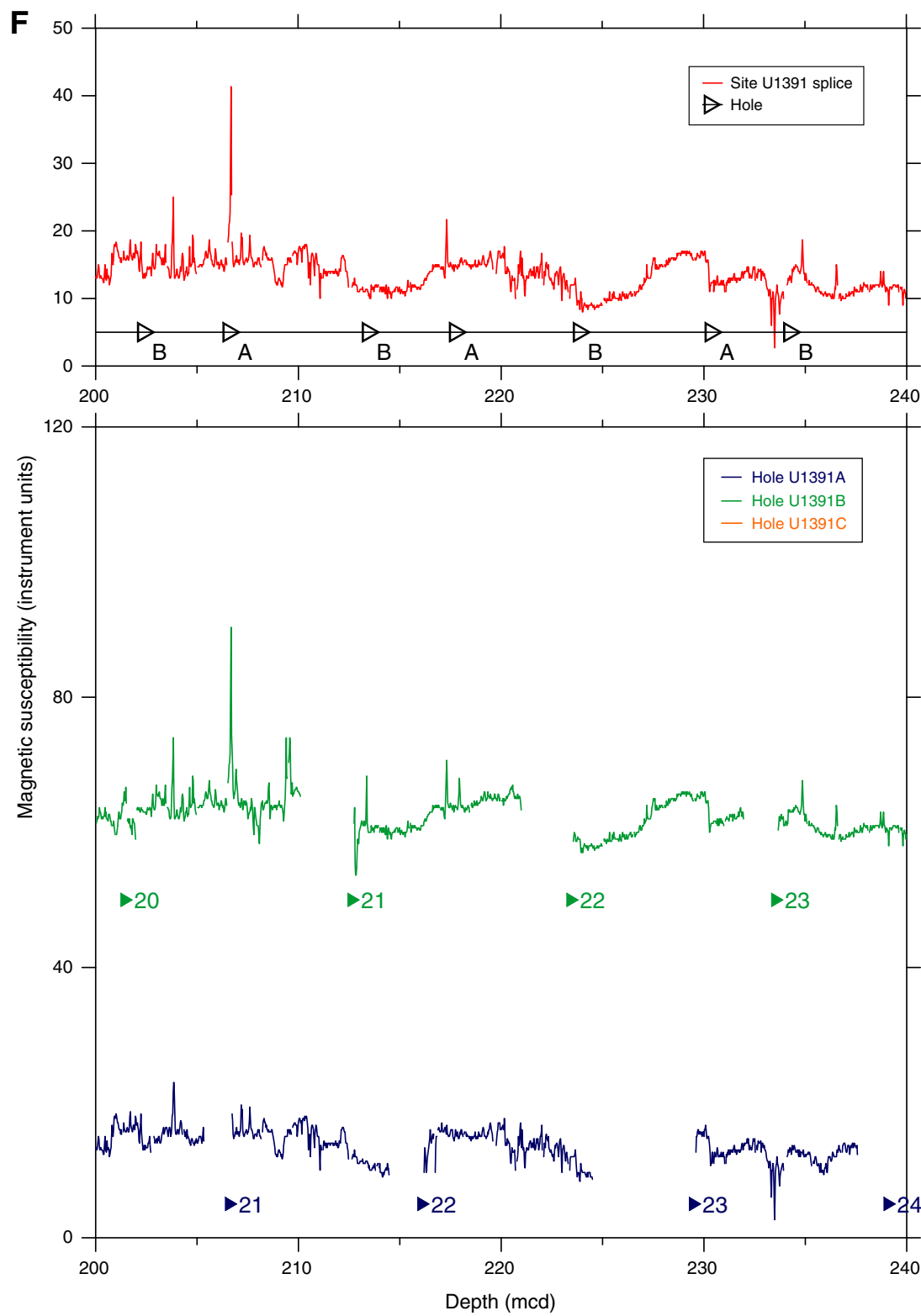


Figure F40 (continued). G. 240–280 mcd. (Continued on next page.)

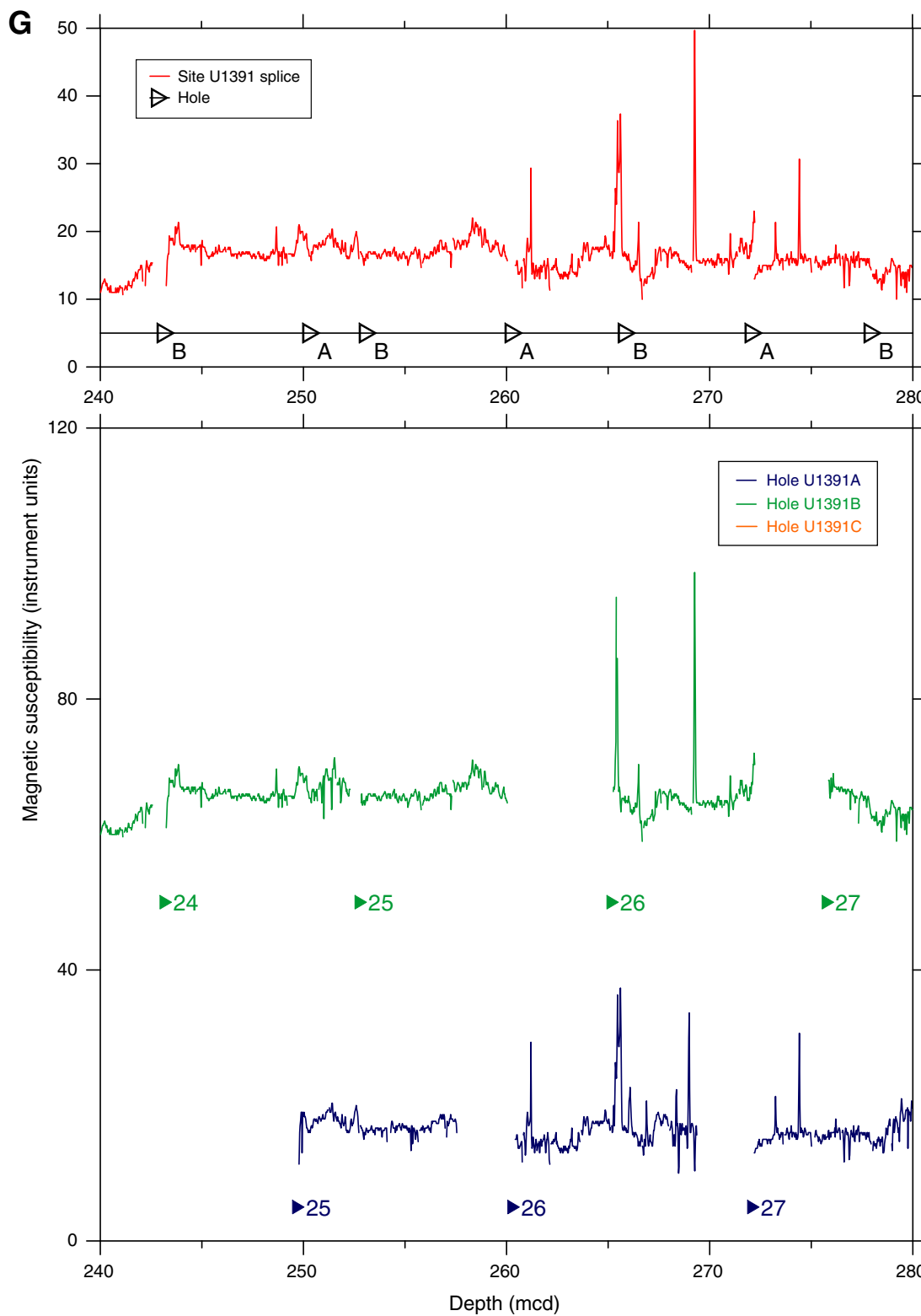


Figure F40 (continued). H. 280–320 mcd. (Continued on next page.)

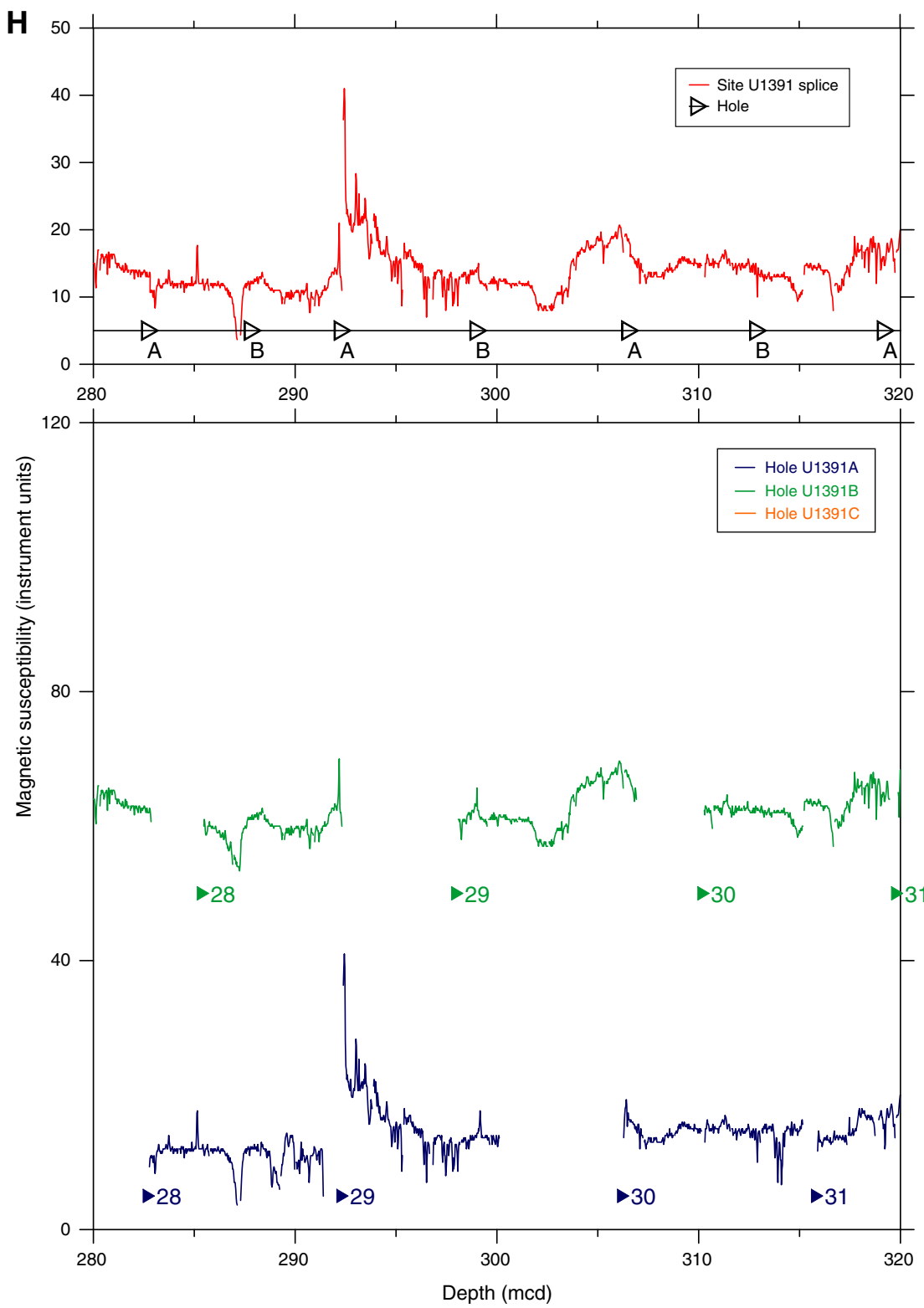


Figure F40 (continued). I. 320–360 mcd. (Continued on next page.)

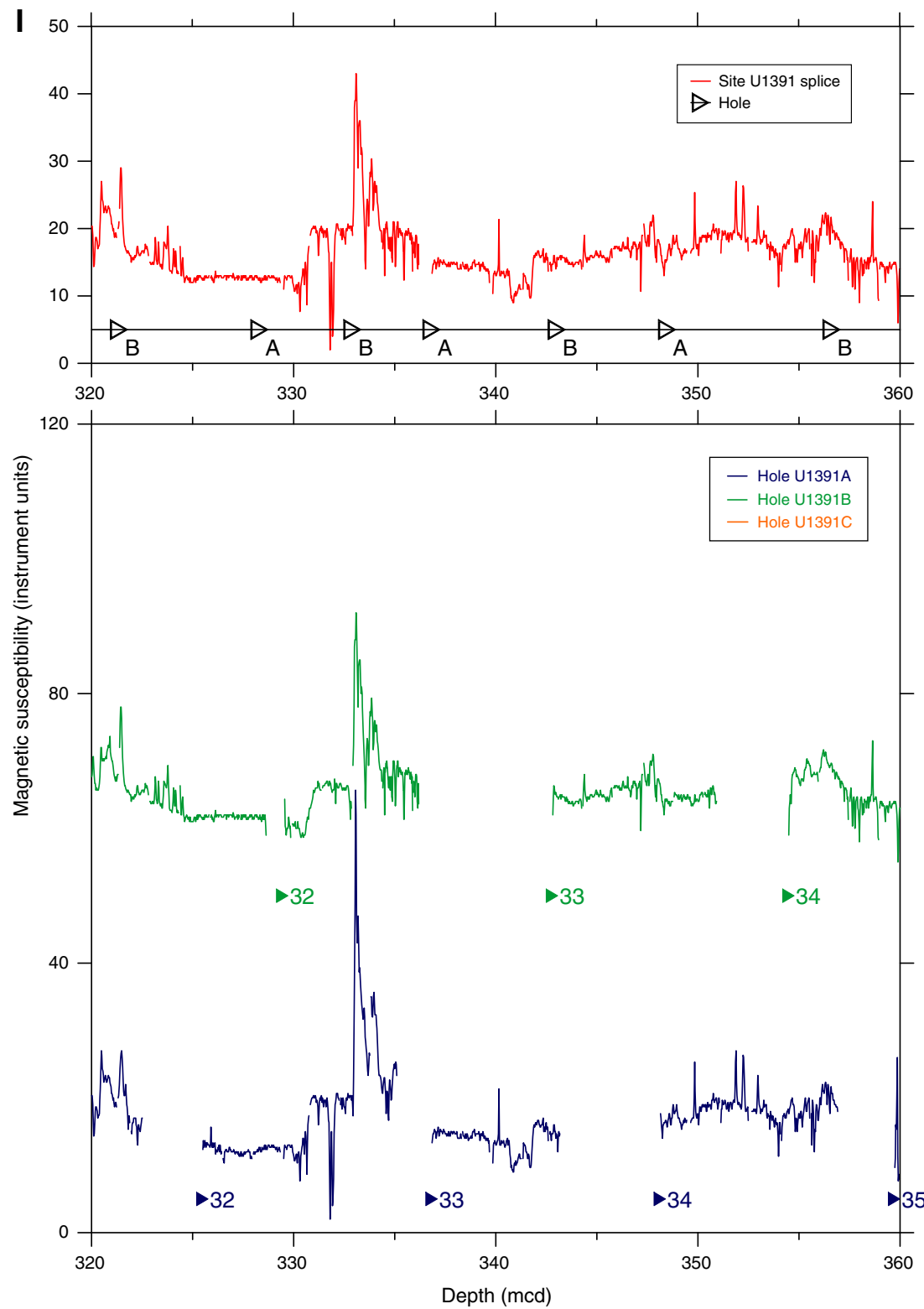


Figure F40 (continued). J. 360–400 mcd. (Continued on next page.)

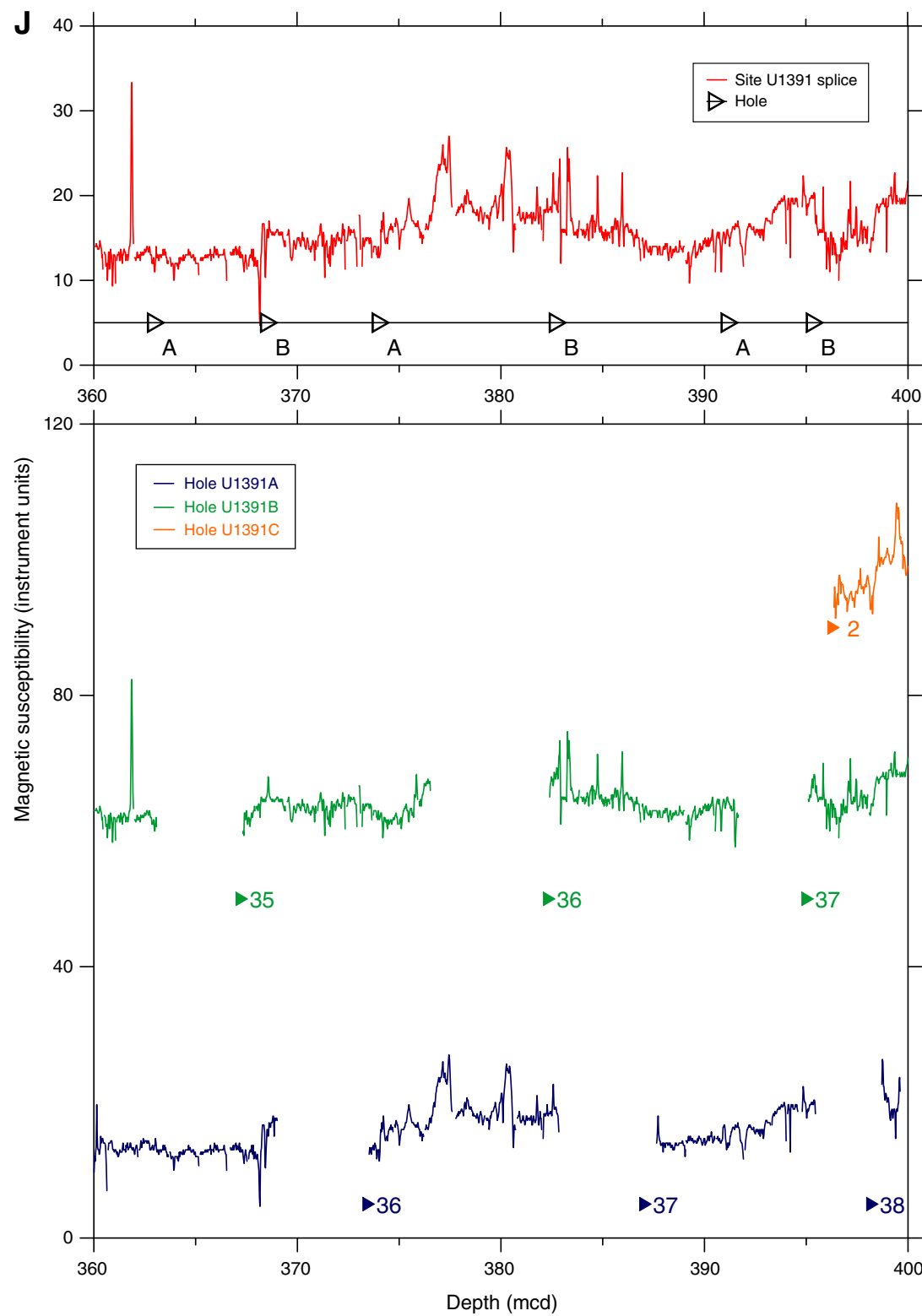


Figure F40 (continued). K. 400–440 mcd.

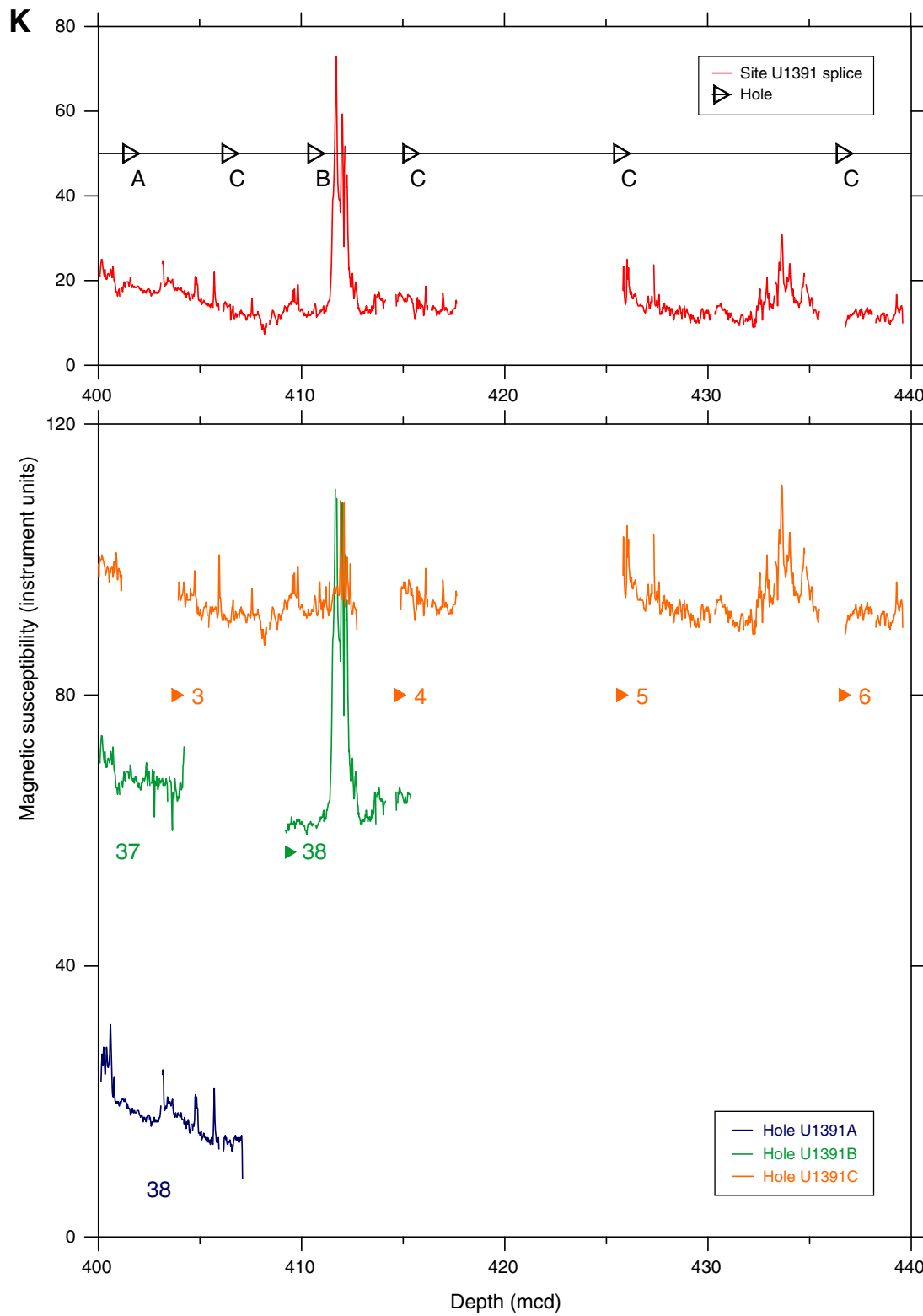


Figure F41. Plot of Site U1391 core top depths for mbsf vs. mcd. The slope of the best-fit line through the core top depths, which is 1.144, gives an estimate of the average amount the mcd scale is expanded relative to the mbsf scales of the three holes.

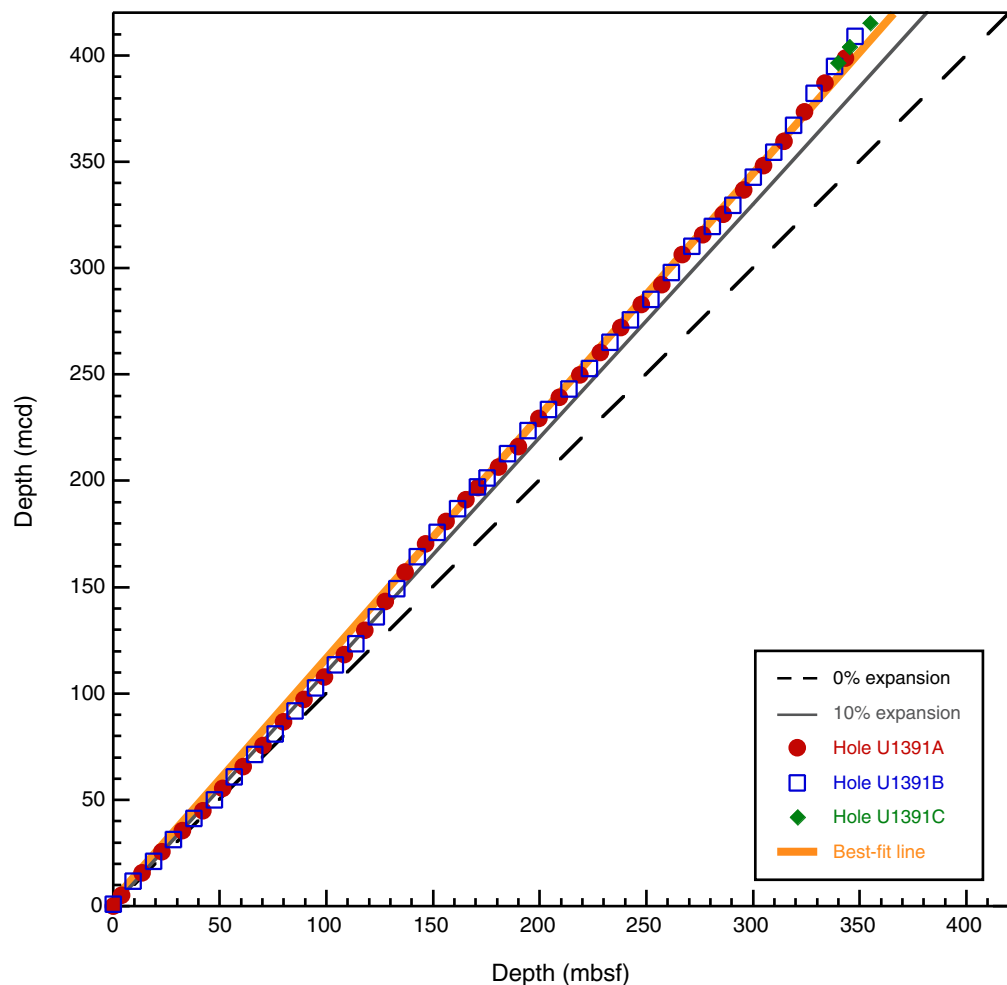


Figure F42. Plot of comparison of natural gamma ray (NGR) data in Holes U1391A–U1391C after data have been placed in the mbsf* depth scale ($\text{mbsf}^* = \text{mcd}/1.144$).

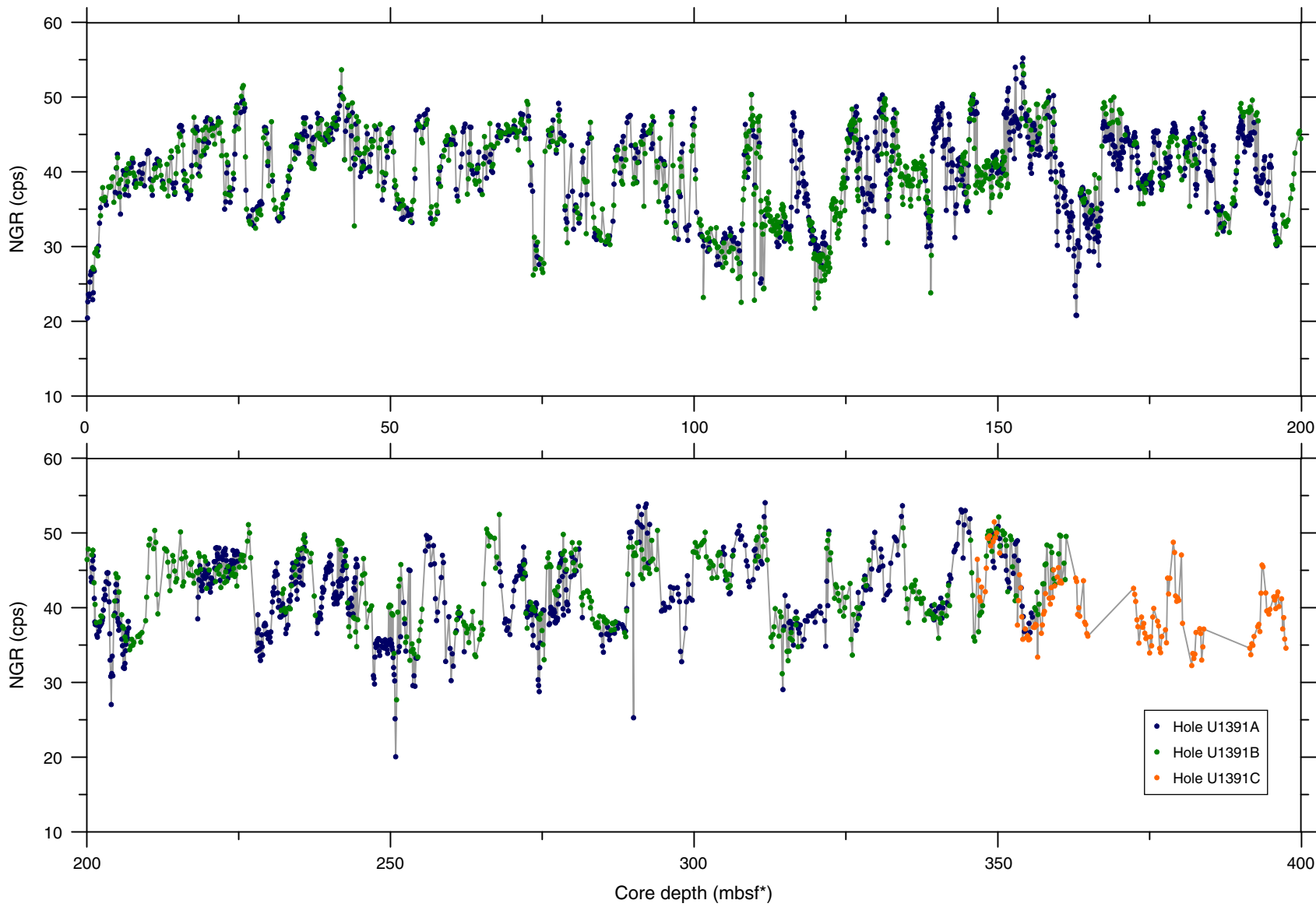


Table T1. Coring summary, Site U1391. (Continued on next two pages.)**Hole U1391A**

Latitude: 37°21.5392'N
 Longitude: 9°24.6601'W
 Time on hole (d): 1.7
 Seafloor (drill pipe measurement below rig floor, m DRF): 1085.4
 Distance between rig floor and sea level (m): 11.7
 Water depth (drill pipe measurement from sea level, mbsl): 1073.7
 Total penetration (drilling depth below seafloor, m DSF): 353.1
 Total length of cored section (m): 353.1
 Total core recovered (m): 342.62
 Core recovery (%): 97.03
 Total number of cores: 38

Hole U1391B

Latitude: 37°21.5288'N
 Longitude: 9°24.6604'W
 Time on hole (d): 1.6
 Seafloor (drill pipe measurement below rig floor, m DRF): 1085.0
 Distance between rig floor and sea level (m): 11.7
 Water depth (drill pipe measurement from sea level, mbsl): 1073.3
 Total penetration (drilling depth below seafloor, m DSF): 353.5
 Total length of cored section (m): 353.5
 Total core recovered (m): 346.93
 Core recovery (%): 98.14
 Total number of cores: 38

Hole U1391C

Latitude: 37°21.5286'N
 Longitude: 9°24.6468'W
 Time on hole (d): 4.3
 Seafloor (drill pipe measurement below rig floor, m DRF): 1085.0
 Distance between rig floor and sea level (m): 11.7
 Water depth (drill pipe measurement from sea level, mbsl): 1073.3
 Total penetration (drilling depth below seafloor, m DSF): 671.5
 Total length of cored section (m): 331.5
 Total core recovered (m): 269.02
 Core recovery (%): 81.15
 Total number of cores: 35

Site U1391 totals

Number of cores: 111
 Penetration (m): 1378.1
 Cored (m): 1038.1
 Recovered (m): 958.57 (92.3%)

Core	Date (2012)	Time (h)	Depth DSF (m)			Depth CSF (m)			Length of core recovered (m)	Curated length (m)	Recovery (%)
			Top of cored interval	Bottom of cored interval	Interval advanced (m)	Top of recovered core	Bottom of recovered core				
339-U1391A-											
1H	8 Jan	2045	0.0	4.1	4.1	0.0	4.16	4.16	4.16	4.16	101
2H	8 Jan	2125	4.1	13.6	9.5	4.1	13.85	9.75	9.75	9.75	103
3H	8 Jan	2150	13.6	23.1	9.5	13.6	23.32	9.72	9.72	9.72	102
4H	8 Jan	2230	23.1	32.6	9.5	23.1	32.97	9.87	9.87	9.87	104
5H	8 Jan	2300	32.6	42.1	9.5	32.6	42.37	9.77	9.77	9.77	103
6H	8 Jan	2330	42.1	51.6	9.5	42.1	52.18	10.02	10.08	10.08	105
7H	9 Jan	0025	51.6	61.1	9.5	51.6	61.71	9.98	10.11	10.11	105
8H	9 Jan	0055	61.1	70.6	9.5	61.1	71.18	10.04	10.08	10.08	106
9H	9 Jan	0135	70.6	80.1	9.5	70.6	80.77	10.17	10.17	10.17	107
10H	9 Jan	0215	80.1	89.6	9.5	80.1	90.17	10.07	10.07	10.07	106
11H	9 Jan	0250	89.6	99.1	9.5	89.6	99.52	9.92	9.92	9.92	104
12H	9 Jan	0330	99.1	108.6	9.5	99.1	109.17	10.07	10.07	10.07	106
13H	9 Jan	0415	108.6	118.1	9.5	108.6	119.00	10.40	10.40	10.40	109
14H	9 Jan	0450	118.1	127.6	9.5	118.1	128.20	10.05	10.10	10.10	106
15H	9 Jan	0525	127.6	137.1	9.5	127.6	136.99	9.47	9.39	9.39	100
16H	9 Jan	0610	137.1	146.6	9.5	137.1	148.03	10.93	10.93	10.93	115
17H	9 Jan	0700	146.6	156.1	9.5	146.6	156.60	10.00	10.00	10.00	105
18H	9 Jan	0740	156.1	165.6	9.5	156.1	167.22	11.12	11.12	11.12	117
19H	9 Jan	0825	165.6	171.1	5.5	165.6	171.10	5.50	5.50	5.50	100
20X	9 Jan	1140	171.1	180.7	9.6	171.1	179.87	8.77	8.77	8.77	91
21X	9 Jan	1210	180.7	190.2	9.5	180.7	189.27	8.57	8.57	8.57	90
22X	9 Jan	1245	190.2	199.8	9.6	190.2	199.40	9.20	9.20	9.20	96
23X	9 Jan	1320	199.8	209.4	9.6	199.8	208.47	8.67	8.67	8.67	90



Table T1 (continued). (Continued on next page.)

Core	Date (2012)	Time (h)	Depth DSF (m)			Depth CSF (m)			Curated length (m)	Recovery (%)					
			Top of cored interval	Bottom of cored interval	Interval advanced (m)	Top of recovered core	Bottom of recovered core	Length of core recovered (m)							
24X	9 Jan	1405	209.4	219.0	9.6	209.4	209.40	0.00	0.00	0					
25X	9 Jan	1455	219.0	228.6	9.6	219.0	227.46	8.46	8.46	88					
26X	9 Jan	1555	228.6	238.2	9.6	228.6	238.67	10.07	10.07	105					
27X	9 Jan	1645	238.2	247.8	9.6	238.2	246.58	8.38	8.38	87					
28X	9 Jan	1735	247.8	257.4	9.6	247.8	256.97	9.17	9.17	96					
29X	9 Jan	1835	257.4	267.0	9.6	257.4	265.74	8.34	8.34	87					
30X	9 Jan	1955	267.0	276.6	9.6	267.0	276.52	9.52	9.52	99					
31X	9 Jan	2045	276.6	286.2	9.6	276.6	283.75	7.15	7.15	74					
32X	9 Jan	2135	286.2	295.8	9.6	286.2	296.25	10.05	10.05	105					
33X	9 Jan	2235	295.8	305.1	9.3	295.8	302.70	6.90	6.90	74					
34X	9 Jan	2330	305.1	314.7	9.6	305.1	314.56	9.46	9.46	99					
35X	10 Jan	0025	314.7	324.3	9.6	314.7	324.44	9.74	9.74	101					
36X	10 Jan	0115	324.3	333.9	9.6	324.3	334.10	9.80	9.80	102					
37X	10 Jan	0210	333.9	343.5	9.6	333.9	343.25	9.35	9.35	97					
38X	10 Jan	0315	343.5	353.1	9.6	343.5	353.51	10.01	10.01	104					
			Advanced total:		353.1										
			Total interval cored:		353.1										
339-U1391B-															
1H	10 Jan	0825	0.0	9.5	9.5	0.0	9.66	9.65	9.66	102					
2H	10 Jan	0930	9.5	19.0	9.5	9.5	19.54	10.04	10.04	106					
3H	10 Jan	1000	19.0	28.5	9.5	19.0	28.89	9.89	9.89	104					
4H	10 Jan	1040	28.5	38.0	9.5	28.5	38.58	10.08	10.08	106					
5H	10 Jan	1125	38.0	47.5	9.5	38.0	47.89	9.89	9.89	104					
6H	10 Jan	1205	47.5	57.0	9.5	47.5	57.71	10.05	10.21	106					
7H	10 Jan	1235	57.0	66.5	9.5	57.0	67.07	10.07	10.07	106					
8H	10 Jan	1335	66.5	76.0	9.5	66.5	76.94	10.44	10.44	110					
9H	10 Jan	1405	76.0	85.5	9.5	76.0	86.25	10.24	10.25	108					
10H	10 Jan	1435	85.5	95.0	9.5	85.5	95.69	10.16	10.19	107					
11H	10 Jan	1520	95.0	104.5	9.5	95.0	104.98	9.98	9.98	105					
12H	10 Jan	1600	104.5	114.0	9.5	104.5	114.83	10.44	10.33	110					
13H	10 Jan	1635	114.0	123.5	9.5	114.0	123.75	9.75	9.75	103					
14H	10 Jan	1730	123.5	133.0	9.5	123.5	133.77	10.25	10.27	108					
15H	10 Jan	1820	133.0	142.5	9.5	133.0	143.45	10.43	10.45	110					
16H	10 Jan	1855	142.5	152.0	9.5	142.5	152.17	9.65	9.67	102					
17H	10 Jan	1935	152.0	161.5	9.5	152.0	159.42	7.40	7.42	78					
18H	10 Jan	2025	161.5	171.0	9.5	161.5	170.94	9.43	9.44	99					
19X	10 Jan	2130	171.0	175.5	4.5	171.0	175.71	4.70	4.71	104					
20X	10 Jan	2210	175.5	185.1	9.6	175.5	184.51	9.01	9.01	94					
21X	10 Jan	2305	185.1	194.6	9.5	185.1	193.83	8.73	8.73	92					
22X	10 Jan	2340	194.6	204.2	9.6	194.6	203.12	8.52	8.52	89					
23X	11 Jan	0025	204.2	213.8	9.6	204.2	213.53	9.23	9.33	96					
24X	11 Jan	0120	213.8	223.4	9.6	213.8	223.28	9.48	9.48	99					
25X	11 Jan	0155	223.4	233.0	9.6	223.4	231.21	7.81	7.81	81					
26X	11 Jan	0235	233.0	242.6	9.6	233.0	240.53	7.53	7.53	78					
27X	11 Jan	0320	242.6	252.2	9.6	242.6	250.13	7.53	7.53	78					
28X	11 Jan	0400	252.2	261.8	9.6	252.2	259.70	7.50	7.50	78					
29X	11 Jan	0440	261.8	271.4	9.6	261.8	271.05	9.25	9.25	96					
30X	11 Jan	0520	271.4	281.0	9.6	271.4	280.99	9.59	9.59	100					
31X	11 Jan	0600	281.0	290.6	9.6	281.0	289.87	8.87	8.87	92					
32X	11 Jan	0640	290.6	300.2	9.6	290.6	298.63	8.03	8.03	84					
33X	11 Jan	0725	300.2	309.8	9.6	300.2	308.79	8.59	8.59	89					
34X	11 Jan	0805	309.8	319.0	9.2	309.8	318.90	9.10	9.10	99					
35X	11 Jan	0855	319.0	328.7	9.7	319.0	328.74	9.74	9.74	100					
36X	11 Jan	0950	328.7	338.2	9.5	328.7	338.45	9.75	9.75	103					
37X	11 Jan	1035	338.2	347.9	9.7	338.2	347.71	9.51	9.51	98					
38X	11 Jan	1125	347.9	353.5	5.6	347.9	354.52	6.62	6.62	118					
			Advanced total:		353.5										
			Total interval cored:		353.5										
339-U1391C-															
1W	12 Jan	1425	****Drilled from 0 to 340.0 m DSF without coring****												
2R	12 Jan	1525	340.0	345.5	5.5	340.0	345.05	5.05	5.05	92					
3R	12 Jan	1640	345.5	355.1	9.6	345.5	354.53	9.03	9.03	94					
4R	12 Jan	1810	355.1	364.7	9.6	355.1	357.98	2.88	2.88	30					
5R	12 Jan	1935	364.7	374.3	9.6	364.7	374.53	9.83	9.83	102					
6R	12 Jan	2105	374.3	383.9	9.6	374.3	377.37	3.07	3.07	32					
7R	12 Jan	2220	383.9	393.5	9.6	383.9	391.49	7.59	7.59	79					
8R	12 Jan	2335	393.5	403.0	9.5	393.5	399.94	6.44	6.44	68					



Table T1 (continued).

Core	Date (2012)	Time (h)	Depth DSF (m)			Depth CSF (m)			Curated length (m)	Recovery (%)
			Top of cored interval	Bottom of cored interval	Interval advanced (m)	Top of recovered core	Bottom of recovered core	Length of core recovered (m)		
9R	13 Jan	0050	403.0	412.6	9.6	403.0	412.14	9.14	9.14	95
10R	13 Jan	0205	412.6	422.2	9.6	412.6	419.60	7.00	7.00	73
11R	13 Jan	0335	422.2	431.8	9.6	422.2	431.16	8.96	8.96	93
12R	13 Jan	0515	431.8	441.3	9.5	431.8	441.65	9.85	9.85	104
13R	13 Jan	0635	441.3	450.9	9.6	441.3	451.17	9.87	9.87	103
14R	13 Jan	0810	450.9	460.5	9.6	450.9	460.84	9.94	9.94	104
15R	13 Jan	0930	460.5	470.0	9.5	460.5	470.36	9.86	9.94	104
16R	13 Jan	1040	470.0	479.7	9.7	470.0	478.52	8.52	8.52	88
17R	13 Jan	1200	479.7	489.0	9.3	479.7	484.79	5.09	5.09	55
18R	13 Jan	1335	489.0	498.6	9.6	489.0	498.75	9.75	9.75	102
19R	13 Jan	1445	498.6	508.1	9.5	498.6	507.95	9.35	9.35	98
20R	13 Jan	1620	508.1	517.7	9.6	508.1	511.52	3.42	3.42	36
21R	13 Jan	1810	517.7	527.3	9.6	517.7	527.01	9.31	9.31	97
22R	13 Jan	1955	527.3	537.0	9.7	527.3	537.22	9.92	9.92	102
23R	13 Jan	2130	537.0	546.6	9.6	537.0	546.94	9.94	9.94	104
24R	13 Jan	2255	546.6	556.2	9.6	546.6	556.62	10.02	10.02	104
25R	14 Jan	0025	556.2	565.8	9.6	556.2	566.10	9.90	9.90	103
26R	14 Jan	0140	565.8	575.4	9.6	565.8	565.80	0.00	0.00	0
27R	14 Jan	0330	575.4	585.0	9.6	575.4	584.19	8.79	8.79	92
28R	14 Jan	0455	585.0	594.6	9.6	585.0	594.85	9.85	9.85	103
29R	14 Jan	0555	594.6	604.2	9.6	594.6	596.10	0.00	0.00	0
30R	14 Jan	0730	604.2	613.8	9.6	604.2	613.97	9.77	9.77	102
31R	14 Jan	0840	613.8	623.4	9.6	613.8	623.45	9.65	9.65	101
32R	14 Jan	1035	623.4	633.0	9.6	623.4	633.34	9.94	9.94	104
33R	14 Jan	1140	633.0	642.6	9.6	633.0	641.60	8.60	8.60	90
34R	14 Jan	1300	642.6	652.2	9.6	642.6	652.11	9.51	9.51	99
35R	14 Jan	1430	652.2	661.8	9.6	652.2	661.71	0.00	9.51	0
36R	14 Jan	1615	661.8	671.5	9.7	661.8	670.98	9.18	9.18	95
Advanced total:			671.5							
Total interval cored:			331.5							

DRF = drilling depth below rig floor, DSF = drilling depth below seafloor, CSF = core depth below seafloor. H = advanced piston coring system, X = extended core barrel system, R = rotary core barrel system, W = washed interval. Time is Universal Time Coordinated.

Table T2. Sediment textures and compositions determined by smear slide, Site U1391.

Lith. unit	Texture (%)			Composition (%)			
	Sand	Silt	Clay	Siliciclastic	Detrital carbonate	Biogenic carbonate	Biogenic silica
IA	15	31	54	43	26	30	1
IB	8	27	65	32	30	35	3
II	9	31	60	40	23	28	7



Table T3. XRD peak intensities of minerals from bulk sediment, Hole U1391A.

Core, section, interval (cm)	Depth (mbsf)	Total intensity (counts)	Quartz (counts)	Calcite (counts)	K-feldspar (counts)	Plagioclase (counts)	Dolomite (counts)	Chlorite (counts)	Kaolinite (counts)	Illite (counts)	Smectite (counts)	Hornblende (counts)	Augite (counts)	Pyrite (counts)	Aragonite (counts)
339-U1391A-															
1H-3, 75–76	3.75	44,840	22,382	12,464	447	995	1,616	746	1,593	3,664	293	NA	640	NA	NA
2H-6, 110–111	12.7	55,931	30,606	12,475	1,037	1,409	1,701	888	1,515	4,417	241	941	701	NA	NA
3H-6, 115–116	22.25	66,039	22,324	11,165	1,914	2,588	2,217	2,485	4,201	17,618	670	193	664	NA	NA
4H-6, 137–138	31.97	55,399	32,548	11,012	706	1,414	1,547	842	1,446	4,678	249	391	566	NA	NA
5H-6, 139–140	41.49	52,314	25,694	13,832	527	987	2,206	779	1,771	5,340	392	135	651	NA	NA
6H-6, 127–128	50.92	65,628	40,331	12,018	718	2,014	1,996	742	1,270	5,136	347	487	569	NA	NA
7H-6, 137–138	60.67	49,638	25,155	15,195	708	1,691	1,332	NA	935	3,063	281	161	525	NA	592
8H-6, 125–126	69.73	57,184	27,935	16,153	515	1,633	1,945	944	1,550	4,898	299	154	644	NA	514
9H-6, 128–129	79.23	55,116	19,998	24,970	297	988	2,033	574	1,229	4,106	272	265	NA	NA	384
10H-6, 122–123	88.46	56,278	25,784	14,340	657	4,543	2,923	862	1,481	4,721	271	209	487	NA	NA
11H-7, 127–128	99.16	48,006	24,448	12,242	748	1,507	1,478	820	1,371	4,178	351	226	637	NA	NA
12H-6, 137–138	106.44	50,164	16,948	22,975	NA	797	1,050	823	1,361	5,165	333	65	454	193	NA
13H-6, 135–136	116.55	49,274	28,527	10,409	524	1,267	925	820	1,334	4,288	265	226	689	NA	NA
14H-6, 135–136	126.55	62,638	22,196	25,996	468	1,242	2,407	999	1,778	6,231	494	167	NA	NA	660
15H-6, 119–120	135.92	47,738	22,192	16,469	324	1,379	1,471	647	1,066	3,025	264	232	522	147	NA
16H-6, 135–136	144.58	66,256	36,842	14,373	728	2,249	2,934	909	1,685	4,935	280	519	NA	NA	802
17H-6, 124–125	154.98	58,136	29,977	15,118	635	1,415	4,313	535	1,160	3,850	340	130	NA	NA	663
18H-6, 70–71	163.28	51,358	23,823	17,636	374	1,033	2,086	762	1,135	3,326	429	143	NA	NA	611
19H-3, 124–125	169.52	48,796	23,729	13,096	495	2,169	1,991	785	1,226	3,928	579	217	581	NA	NA
20X-5, 135–136	178.45	46,141	23,068	11,409	495	1,178	1,872	868	1,650	4,432	350	156	663	NA	NA
21X-5, 114–115	187.77	50,059	21,912	19,845	466	980	1,548	551	1,075	3,083	378	221	NA	NA	NA
22X-7, 118–119	198.56	62,242	27,576	17,847	782	1,803	2,216	1,231	2,056	7,545	395	186	NA	NA	605
23X-6, 74–75	207.76	66,610	29,591	13,666	2,227	1,509	7,466	1,161	1,878	7,337	354	207	589	NA	625
25X-6, 49–50	226.74	56,401	22,346	12,945	818	1,770	2,054	1,685	2,868	10,369	725	136	505	180	NA
26X-6, 127–128	236.17	66,895	28,560	12,387	1,102	2,172	3,559	2,084	2,981	12,419	692	339	600	NA	NA
27X-6, 96–97	245.94	67,684	31,837	9,104	929	2,804	1,698	2,159	3,119	14,326	513	354	634	207	NA
28X-6, 65–66	254.95	59,200	31,118	10,879	1,364	1,773	1,760	1,602	2,193	7,274	543	145	549	NA	NA
29X-6, 43–44	265.15	54,085	24,049	15,433	NA	6,443	2,563	669	1,173	3,240	398	117	NA	NA	NA
30X-6, 130–131	275.13	53,033	25,551	16,329	457	1,141	2,361	1,016	1,542	4,010	514	112	NA	NA	NA
31X-6, 57–58	283.21	47,476	23,159	13,522	655	1,077	3,209	593	1,148	3,492	459	NA	NA	162	NA
32X-6, 141–142	294.41	67,611	23,855	9,923	1,052	2,424	2,201	3,002	4,479	18,936	600	410	729	NA	NA
33X-4, 123–124	301.53	59,491	24,871	12,494	943	3,361	2,407	1,625	2,285	10,092	605	156	652	NA	NA
34X-6, 128–129	313.85	54,185	31,414	9,005	926	2,730	2,021	886	1,474	4,438	338	242	711	NA	NA
35X-6, 39–40	322.05	53,014	25,251	17,303	493	1,499	1,248	874	1,425	3,988	329	154	450	NA	NA
36X-6, 116–117	332.71	51,778	30,304	8,901	719	1,944	1,874	838	1,235	4,245	340	385	580	413	NA
37X-6, 130–135	341.37	51,375	27,132	9,914	895	1,679	2,378	940	1,653	5,153	363	212	636	420	NA
38X-6, 75–76	351.66	56,854	30,126	15,391	655	1,234	2,144	798	1,718	4,179	345	264	NA	NA	NA

NA = no peak detected.



Table T4. Biostratigraphic datums, Site U1391.

Event	Reference	Age (Ma)	Hole U1391A depth (mbsf)			Hole U1391B depth (mbsf)			Hole U1391C depth (mbsf)		
			Top	Bottom	Mean	Top	Bottom	Mean	Top	Bottom	Mean
LrO <i>Emiliana huxleyi</i> (>4 µm)	Flores et al., 2010	0.01	2.92	3.60	3.26	0.00	9.61	4.80			
FO <i>Emiliana huxleyi</i>	Raffi et al., 2006	0.26	70.18	71.35	70.76	67.07	76.94	72.00			
LO <i>Pseudoemiliana lacunosa</i>	Raffi et al., 2006	0.46	114.57	115.95	115.26	114.83	123.75	119.29			
<i>Stilostomella</i> extinction	Hayward, 2002; Kawagata et al., 2005	0.65	189.27	199.40	194.33						
LO <i>Reticulofenestra asanoi</i>	Raffi et al., 2006	0.90	227.46	231.11	229.28	231.21	240.53	235.87			
FO <i>Reticulofenestra asanoi</i>	Raffi et al., 2006	1.07	291.84	294.70	293.27	298.63	308.79	303.71			
T paracme <i>Neogloboquadrina pachyderma</i> (sin)	Lourens et al., 2004	1.21	324.44	334.10	329.27	318.90	328.74	323.82			
LO large <i>Gephyrocapsa</i> (>5.5 µm)	Raffi et al., 2006	1.24	334.10	343.25	338.68	328.74	338.45	333.60			
LO <i>Helicosphaera sellii</i>	Raffi et al., 2006	1.25	343.25	353.51	348.38	328.74	338.45	333.60			
FO large <i>Gephyrocapsa</i> (>5.5 µm)	Raffi et al., 2006	1.61							391.49	399.92	395.71
LO <i>Calcidiscus macintyrei</i>	Raffi et al., 2006	1.66							399.92	412.14	406.03
LO <i>Discoaster brouweri</i>	Raffi et al., 2006	1.95							470.36	478.52	474.44
FO <i>Globorotalia inflata</i>	Lourens et al., 2004	2.09							498.75	507.95	503.35
T <i>Neogloboquadrina atlantica</i> (sin)	Weaver and Clement, 1987	2.41							546.94	556.62	551.78
LO <i>Globorotalia puncticulata</i>	Lourens et al., 2004	2.41							556.62	566.10	561.36
LO <i>Discoaster surculus</i>	Raffi et al., 2006	2.53							556.62	566.10	561.36
LO <i>Discoaster tamalis</i>	Raffi et al., 2006	2.80							594.85	613.97	604.41
Coiling change <i>Globorotalia crassaformis</i>	Zachariasse et al., 1991	2.99							594.85	613.97	604.41
LO <i>Sphaeroidinellopsis seminula</i>	Lourens et al., 2004	3.19							639.35	641.6	637.47
T disappearance of <i>Globorotalia puncticulata</i>	Lourens et al., 2005	3.31							652.11	670.98	661.545

LO = last occurrence, FO = first occurrence, LrO = last regular occurrence, T = top. sin = sinistral.



Table T5. Abundance of nannofossils, Site U1391. (Continued on next two pages.)

Table T5 (continued). (Continued on next page.)

Core, section	Depth (mbsf)	Preservation	Unbillediscphaea lineage											
			Thraustosphaera spp.			Sphaerosphaera spp.			Rhabdosphaera spp.			Symploctisphaera spp.		
339-U1391B-														
1H-CC	9.65	G	A	R	F	R							R	R
2H-CC	19.54	G	VA	F	F	R							F	F
3H-CC	28.89	G	VA	F	F	R							F	F
4H-CC	38.58	G	VA	F	F	R							F	F
5H-CC	47.89	G	VA	F	F	R							F	F
6H-CC	57.55	M	VA	F	F	R							F	F
7H-CC	67.07	M	VA	F	F	R							F	F
8H-CC	76.94	M	VA	F	F	R							F	F
9H-CC	86.24	G	VA	F	F	R							F	F
10H-CC	95.66	M	VA	F	F	R							F	F
11H-CC	104.98	G	VA	F	F	R							F	F
12H-CC	114.94	G	VA	F	F	R							F	F
13H-CC	123.75	G	VA	F	F	R							F	F
14H-CC	133.75	G	VA	F	F	R							F	F
15H-CC	143.38	G	VA	F	F	R							F	F
16H-CC	152.15	G	A	F	F	R							F	F
17H-CC	159.40	M	A	F	F	R							F	F
18H-CC	170.93	M	C	R	R	R							F	F
19X-CC	175.70	M	VA	R	R	R							F	F
20X-CC	184.51	G	A	R	R	R							F	F
21X-CC	193.83	G	C	R	R	R							F	F
22X-6	203.12	G	VA	R	R	R							F	F
23X-CC	213.43	M	C	R	R	R							F	F
24X-CC	223.28	M	A	R	R	R							F	F
25X-CC	231.21	M	VA	R	R	R							F	F
26X-CC	240.53	G	VA	R	R	R							F	F
27X-CC	250.13	M	VA	R	R	R							F	F
28X-CC	259.70	M	C	R	R	R							F	F
29X-CC	271.05	M	VA	R	R	R							F	F
30X-CC	280.99	M	VA	R	R	R							F	F
31X-CC	289.87	G	VA	R	R	R							F	F
32X-CC	298.63	M	C	F	R	R							F	F
33X-CC	308.79	M	VA	F	R	R							F	F
34X-CC	318.90	M	VA	F	R	R							F	F
35X-CC	328.74	M	VA	F	R	R							F	F
36X-CC	338.45	M	VA	F	R	R							F	F





Table T5 (continued).

Core, section	Depth (mbsf)	Preservation	Unbilled cephalopoda lineage															
			Thaumatosphera spp.				Rhabdosphera spp.				Syphobosphera spp.				Thaumatosphera osanoi (6 µm)			
339-U1391C-																		
2R-CC	345.05	G	VA	F	F	F	F	F	F	F	R	C	C	C	A	F	F	F
3R-CC	354.53	M	VA	F	F	F	F	F	F	F	P	F	F	F	F	R	F	F
4R-CC	357.98	G	VA	F	F	F	F	F	F	F	R	F	F	F	R	R	R	R
5R-CC	374.53	G	VA	R	F	F	F	F	F	F	R	F	F	F	R	R	R	R
6R-CC	377.37	G	A	F	F	F	F	F	F	F	R	F	F	F	R	R	R	R
7R-CC	391.49	G	VA	F	F	F	F	F	F	F	R	F	F	F	R	R	R	R
8R-CC	399.92	G	VA	F	F	F	F	F	F	F	R	F	F	F	R	R	R	R
9R-CC	412.14	G	VA	F	F	F	F	F	F	F	R	F	F	F	R	R	R	R
10R-CC	419.60	M	VA	F	F	F	F	F	F	F	R	F	F	F	R	R	R	R
11R-CC	431.15	M	A	F	F	F	F	F	F	F	R	F	F	F	R	R	R	R
12R-CC	441.65	M	A	F	F	F	R	F	F	F	R	F	F	F	R	R	R	R
13R-CC	451.17	M	VA	F	F	R	F	F	F	F	R	F	F	F	R	R	R	R
14R-CC	460.84	M	VA	F	F	F	R	F	F	F	R	F	F	F	R	R	R	R
15R-CC	470.36	G	VA	R	F	R	F	F	F	F	P	F	F	F	R	R	R	R
16R-CC	478.52	G	VA	F	F	F	F	F	F	F	P	F	F	F	R	R	R	R
17R-CC	484.79	M	VA	F	F	F	F	F	F	F	P	F	F	F	R	R	R	R
18R-CC	498.75	G	VA	F	F	F	F	F	F	F	P	F	F	F	R	R	R	R
19R-7	507.95	G	VA	F	F	F	F	F	F	F	P	F	F	F	R	R	R	R
20R-CC	511.52	G	VA	F	F	F	F	F	F	F	P	F	F	F	R	R	R	R
21R-CC	527.01	G	VA	F	F	F	F	F	F	F	P	F	F	F	R	R	R	R
22R-CC	537.22	G	A	F	F	F	F	F	F	F	P	F	F	F	R	R	R	R
23R-CC	546.94	G	VA	F	F	F	F	F	F	F	P	F	F	F	R	R	R	R
24R-CC	556.62	M	A	F	F	F	F	R	F	F	P	F	F	F	R	R	R	R
25R-CC	566.10	M	VA	F	F	F	R	C	R	F	P	F	F	F	R	R	R	R
27R-CC	584.19	M	VA	F	F	F	R	C	R	F	P	R	R	R	R	R	R	R
28R-CC	594.85	M	A	F	F	F	R	C	R	F	P	R	R	R	R	R	R	R
30R-CC	613.97	G	VA	F	F	F	R	C	R	F	R	R	R	R	R	R	R	R
31R-CC	623.45	M	VA	F	F	F	R	F	R	F	R	R	R	R	R	R	R	R
32R-CC	633.34	M	C	F	R	R	F	P	R	R	P	F	F	F	R	R	R	R

Preservation: G = good, M = moderate. Abundance: D = dominant, VA = very abundant, A = abundant, C = common, F = few, P = present, R = rare. See "Biostratigraphy" in the "Methods" chapter (Expedition 339 Scientists, 2013b) for abundance and preservation definitions.

Table T6. Abundance of planktonic foraminifers, Site U1391. This table is available in an [oversized format](#).**Table T7.** Abundance of benthic foraminifers, Site U1391. This table is available in an [oversized format](#).**Table T8.** Abundance of pollen and spores, Holes U1391A and U1391C.

Core, section	Depth (mbsf)		Preservation	Abundance	Ailanthus	Anthemis type	Apiaceae	Artemisia	Aster type	Betula	Brassicaceae	Caryophyllaceae	Chenopodiaceae	Corylus	Cupressaceae	Cyperaceae	Ephedra distachya type	Ephedra fragilis type	Ericaceae	Isoetes	Olea	Phillyrea	Pinus	Plantago	Poaceae	Quercus deciduous type	Quercus evergreen type	Salix	Taraxacum type	Taxodiaceae/Cupressaceae	Trilete ornamented
	Top	Bottom																													
339-U1391A-																															
1H-CC	4.11	4.16	M	A	F	A	F			C	A					C	C									C	F	F			
7H-CC	61.66	61.71	G	A	C	C	C			F	C					F	C	A	C	A					C	A	F	A			
14H-CC	128.14	128.19	G	A	F	F	C	C		C	A					F	F	C	A	C	C	F	C		C	A	C	A		F	
21X-CC	189.22	189.27	G	A		F	F				C					F	F	C	A	F	C	C			F	C	F	A			
28X-CC	256.92	256.97	M	A		C	C	C		F	F	A				F	C	F	C	C	A	A			C	C	A				
35X-CC	324.39	324.44	P	A		A	A	A	A	A	A	A					A	A	A	A	A	A			A	A	A				
339-U1391C-																															
5R-CC	374.48	374.53	M	A		F	C			F	F	F					F	F	C	F	A				C	C	A	F			
15R-CC	470.31	470.36	P	A		F	F	C	C								F	F	C	F	C	F			F	F	F	A			

Group preservation: G = good, M = medium, P = poor. Group abundance: A = abundant, C = common, F = few. See “[Biostratigraphy](#)” in the “Methods” chapter (Expedition 339 Scientists, 2013b) for abundance and preservation definitions.



Table T9. FlexIt tool core orientation data, Site U1391.

Core	Orientation angle (°)	Orientation standard deviation (°)
339-U1391A-		
4H	218	0.27
5H	70	0.08
6H	176	0.33
7H	132	0.28
8H	236	0.14
9H	178	0.07
10H	50	0.28
11H	214	0.10
12H	348	0.03
13H	337	0.14
14H	41	0.48
15H	280	0.10
16H	348	0.41
17H	74	0.01
18H	197	0.07
19H	242	0.02
339-U1391B-		
3H	16	0.21
4H	305	1.82
5H	224	0.59
6H	258	0.03
7H	66	0.13
8H	333	1.22
9H	233	0.03
10H	327	0.12
11H	331	0.02
12H	261	0.00
13H	84	0.24
14H	171	0.04
15H	39	0.02
16H	59	0.05
17H	153	0.02
18H	319	0.11

Table T10. NRM inclination, declination, and intensity data after 20 mT peak field AF demagnetization, Hole U1391A.

Core, section, interval (cm)	Depth (mbsf)	Inclination (°)	Declination (°)	FlexIt-corrected declination (°)	Intensity (A/m)
339-U1391A-					
1H-1	0.00				
1H-1, 5	0.05				
1H-1, 10	0.10				
1H-1, 15	0.15				
1H-1, 20	0.20				
1H-1, 25	0.25				
1H-1, 30	0.30				
1H-1, 35	0.35	60.2	228.2		0.014022
1H-1, 40	0.40	58.3	230.1		0.012544
1H-1, 45	0.45	59.5	220		0.011093
1H-1, 50	0.50	56.9	205.1		0.011461
1H-1, 55	0.55	56.5	203.6		0.013273
1H-1, 60	0.60	48.9	215.9		0.015693
1H-1, 65	0.65	49.3	219.5		0.017084
1H-1, 70	0.70	52.5	221.1		0.017791
1H-1, 75	0.75	57.5	220.1		0.019657
1H-1, 80	0.80	59.6	216		0.02317
1H-1, 85	0.85	62.5	217		0.025647
1H-1, 90	0.90	61.6	220.8		0.028343
1H-1, 95	0.95	63.3	220.7		0.027091
1H-1, 100	1.00	65.5	216.5		0.025337
1H-1, 105	1.05	63	216.1		0.025957
1H-1, 110	1.10	61.5	216.6		0.025611
1H-1, 115	1.15	61.1	212.8		0.025078
1H-1, 120	1.20	61.3	181		0.024382
1H-1, 125	1.25	58.9	166.3		0.0255
1H-1, 130	1.30	58.9	167		0.026128
1H-1, 135	1.35	58.2	161.4		0.025444
1H-1, 140	1.40				
1H-1, 145	1.45				
1H-1, 150	1.50				
1H-2	1.50				
1H-2, 5	1.55				
1H-2, 10	1.60				
1H-2, 15	1.65	60.7	197.7		0.023061
1H-2, 20	1.70	62.5	196.8		0.020941
1H-2, 25	1.75	62.5	190.4		0.020306
1H-2, 30	1.80	61.2	187.4		0.020883
1H-2, 35	1.85	62	187.3		0.020945
1H-2, 40	1.90	60	189.5		0.021987
1H-2, 45	1.95	61.8	190.7		0.022358
1H-2, 50	2.00	66.3	187		0.023267
1H-2, 55	2.05	63.4	185.2		0.026009
1H-2, 60	2.10	62.7	185.6		0.027397
1H-2, 65	2.15	62.7	184.5		0.027284
1H-2, 70	2.20	59.5	185.1		0.028287
1H-2, 75	2.25	63.8	184.3		0.027107
1H-2, 80	2.30	66.4	182.5		0.026874
1H-2, 85	2.35	64.7	190		0.027951
1H-2, 90	2.40	67	189.5		0.026269
1H-2, 95	2.45	65.1	187.4		0.025956
1H-2, 100	2.50	62	188.9		0.025714
1H-2, 105	2.55	65	187		0.023933
1H-2, 110	2.60	62.4	184.5		0.025918
1H-2, 115	2.65	62	181.4		0.026268
1H-2, 120	2.70	63.5	180		0.02569

Blank cells indicate depth levels where data were either not available (i.e., FlexIt-corrected declination data for nonoriented cores) or removed because of disturbance, voids, or measurement edge effects. Only a portion of this table appears here. The complete table is available in [ASCII](#).

Table T11. NRM inclination, declination, and intensity data after 20 mT peak field AF demagnetization, Hole U1391B.

Core, section, interval (cm)	Depth (mbsf)	Inclination (°)	Declination (°)	Flexlt-corrected declination (°)	Intensity (A/m)
339-U1391B-					
1H-1, 0.00					
1H-1, 5	0.05				
1H-1, 10	0.10				
1H-1, 15	0.15	86.5	293.9		0.04883
1H-1, 20	0.20	83.3	354.6		0.049121
1H-1, 25	0.25	77.1	349.6		0.041406
1H-1, 30	0.30	69	349.1		0.037523
1H-1, 35	0.35	65.4	351.4		0.038743
1H-1, 40	0.40	68.9	352.8		0.037628
1H-1, 45	0.45	73.2	348.4		0.033997
1H-1, 50	0.50	68.8	355.4		0.034376
1H-1, 55	0.55	65.1	356.2		0.035328
1H-1, 60	0.60	63.1	350		0.03269
1H-1, 65	0.65	61.4	351.1		0.029744
1H-1, 70	0.70	60.8	352.8		0.028656
1H-1, 75	0.75	60.9	349		0.027649
1H-1, 80	0.80	60.8	347.9		0.025769
1H-1, 85	0.85	60.2	349.8		0.023994
1H-1, 90	0.90	61.4	354.8		0.022075
1H-1, 95	0.95	62.9	355.1		0.019893
1H-1, 100	1.00	61.4	353.1		0.018273
1H-1, 105	1.05	58.3	350.9		0.018538
1H-1, 110	1.10	53.7	350.6		0.019631
1H-1, 115	1.15	55.2	349.7		0.020174
1H-1, 120	1.20	58.3	349.2		0.020879
1H-1, 125	1.25	58.4	349.1		0.022429
1H-1, 130	1.30	54.4	348.8		0.024558
1H-1, 135	1.35	53.8	346.1		0.024804
1H-1, 140	1.40				
1H-1, 145	1.45				
1H-1, 150	1.50				
1H-2	1.51				
1H-2, 5	1.56				
1H-2, 10	1.61				
1H-2, 15	1.66	60.3	359.4		0.02619
1H-2, 20	1.71	60.2	0.8		0.026749
1H-2, 25	1.76	60.7	357.9		0.026308
1H-2, 30	1.81	59.9	357.3		0.026556
1H-2, 35	1.86	59.3	1.6		0.027718
1H-2, 40	1.91	57.3	0.5		0.029682
1H-2, 45	1.96	56	0.7		0.030459
1H-2, 50	2.01	56.9	1.2		0.029949
1H-2, 55	2.06	57.1	1.3		0.029788
1H-2, 60	2.11	55.7	0.1		0.03015
1H-2, 65	2.16	53.5	1.7		0.031393
1H-2, 70	2.21	52.4	4.4		0.032268
1H-2, 75	2.26	52.4	6.6		0.032296
1H-2, 80	2.31	52.1	8.7		0.032217
1H-2, 85	2.36	50.8	11.1		0.032548
1H-2, 90	2.41	48.5	12.6		0.033827
1H-2, 95	2.46	49.3	11.4		0.033962
1H-2, 100	2.51	50.3	6.6		0.03335
1H-2, 105	2.56	49	7.7		0.033129
1H-2, 110	2.61	48.6	10.9		0.03329
1H-2, 115	2.66	52.6	14.9		0.031722
1H-2, 120	2.71	52.4	17.7		0.030419

Blank cells indicate depth levels where data were either not available (i.e., Flexlt-corrected declination data for nonoriented cores) or removed because of disturbance, voids, or measurement edge effects. Only a portion of this table appears here. The complete table is available in [ASCII](#).



Table T12. NRM inclination, declination, and intensity data after 20 mT peak field AF demagnetization, Hole U1391C.

Core, section, interval (cm)	Depth (mbsf)	Inclination (°)	Declination (°)	Flexlt-corrected declination (°)	Intensity (A/m)
339-U1391C-					
2R-1	340.00				
2R-1, 5	340.05				
2R-1, 10	340.10				
2R-1, 15	340.15	-9.8	84.6		0.001456
2R-1, 20	340.20	-10.4	86.3		0.001361
2R-1, 25	340.25	-8.5	92.6		0.001251
2R-1, 30	340.30	-8.6	94.6		0.0007586
2R-1, 35	340.35	8.2	101.3		0.001021
2R-1, 40	340.40	-9.5	109.4		0.0005744
2R-1, 45	340.45	-21.4	114.8		0.001065
2R-1, 50	340.50	-35.9	118.1		0.001159
2R-1, 55	340.55	-41	107.4		0.001083
2R-1, 60	340.60	-32.1	104.6		0.001118
2R-1, 65	340.65	-28.9	85.5		0.0009874
2R-1, 70	340.70	-24.4	83		0.0008581
2R-1, 75	340.75	-15.9	99.2		0.0009338
2R-1, 80	340.80	-18	101.4		0.0009876
2R-1, 85	340.85	-26	82.8		0.0008152
2R-1, 90	340.90	-24.5	66.6		0.001002
2R-1, 95	340.95	-25.5	80.4		0.001089
2R-1, 100	341.00	-32.2	113.9		0.000854
2R-1, 105	341.05	-19.9	108.2		0.0008253
2R-1, 110	341.10	-14.2	92.8		0.001024
2R-1, 115	341.15	-15.3	88.6		0.001103
2R-1, 120	341.20	-19.8	103.3		0.0009573
2R-1, 125	341.25	-40	170.7		0.0005689
2R-1, 130	341.30	22.3	7.1		0.001285
2R-1, 135	341.35	38.1	44.7		0.001194
2R-1, 140	341.40				
2R-1, 145	341.45				
2R-1, 150	341.50				
2R-2	341.50				
2R-2, 5	341.55				
2R-2, 10	341.60				
2R-2, 15	341.65	-35.6	260.1		0.001255
2R-2, 20	341.70	-43.1	309.6		0.001073
2R-2, 25	341.75	-48.5	328.2		0.000859
2R-2, 30	341.80	-57	269.4		0.0005821
2R-2, 35	341.85	-55.4	217		0.0003853
2R-2, 40	341.90	-68.2	59.3		0.0002504
2R-2, 45	341.95	-47.2	320.3		0.0003222
2R-2, 50	342.00	-42.2	309.5		0.0004406
2R-2, 55	342.05	-63	351.4		0.0004026
2R-2, 60	342.10	-73.2	267.1		0.0004312
2R-2, 65	342.15	-45.8	238.8		0.0008045
2R-2, 70	342.20	-44.3	270.5		0.001238
2R-2, 75	342.25	-64	264.1		0.0008406
2R-2, 80	342.30	-30.9	57.8		0.0007789
2R-2, 85	342.35	-2.2	7.4		0.000577
2R-2, 90	342.40	-28.5	270.4		0.0006048
2R-2, 95	342.45	-38.1	250.3		0.0006385
2R-2, 100	342.50	-47.2	246.1		0.0005717
2R-2, 105	342.55	-64.4	281.7		0.0004235
2R-2, 110	342.60	-59.9	248.3		0.0003664
2R-2, 115	342.65	-67.4	184.1		0.00034
2R-2, 120	342.70	-75.3	297.9		0.0002106

Blank cells indicate depth levels where data were either not available (i.e., Flexlt-corrected declination data for nonoriented cores) or removed because of disturbance, voids, or measurement edge effects. Only a portion of this table appears here. The complete table is available in [ASCII](#).



Table T13. Polarity boundaries, Site U1391.

Polarity boundary	Age (Ma)	Depth (mbsf)		
		Hole U1391A	Hole U1391B	Hole U1391C
Brunhes/Matuyama	0.781	Below 175	Below 175	
T Olduvai	1.778			452–463
B Olduvai	1.945			486
Matuyama/Gauss	2.581			575

T = top, B = bottom.

Table T14. Headspace sample hydrocarbon concentrations, Holes U1391A and U1391C.

Core, section	Depth (mbsf)	Concentration (ppmv)				
		Methane	Ethene	Ethane	Propene	Propane
339-U1391A-						
1H-3	3.00	5.43	—	—	—	—
2H-7	13.00	3.98	—	—	—	—
3H-7	22.41	2,494.22	—	—	—	—
4H-7	32.10	13,605.65	—	0.45	—	—
5H-7	41.60	23,483.6	0.53	0.69	—	—
6H-7	51.15	36,354.05	—	0.84	0.61	—
7H-7	60.73	26,225.48	—	0.88	0.47	0.31
8H-7	69.91	41,703.97	0.72	2.02	—	—
9H-7	79.36	16,198.78	0.81	1.23	—	—
10H-7	88.65	9,855.19	—	1.63	—	—
12H-8	107.94	6,405.11	—	—	—	—
13H-8	117.77	6,028.83	1	0.81	0.33	0.32
14H-7	126.70	6,277.29	—	0.88	—	—
15H-7	136.05	8,973.06	—	1.06	0.3	—
16H-8	146.28	12,022.39	0.59	0.81	0.37	—
17H-7	155.16	9,349.06	—	0.92	—	—
18H-8	165.43	12,358.28	1.66	1.67	—	—
20X-5	177.10	13,139.37	1	1.63	—	—
21X-5	186.63	11,539.07	0.71	1.44	—	—
22X-4	193.75	7,474.79	0.53	0.92	—	—
23X-4	204.30	7,022.86	1.1	2	—	—
25X-4	223.50	9,415.01	0.89	1.83	—	0.34
26X-6	234.90	13,225.2	0.78	2.12	—	—
27X-3	241.20	6,758.85	0.51	0.79	—	0.35
28X-4	252.31	20,642.64	1.75	2.32	—	—
29X-4	261.85	7,807.1	0.76	2.23	0.37	0.34
30X-4	271.02	6,120.59	—	0.94	—	—
31X-3	279.61	4,957.69	—	0.74	—	—
32X-4	290.19	8,901.46	1.22	1.82	—	—
33X-3	298.80	6,208.26	1.07	2.1	—	0.7
34X-4	309.60	5,862.39	0.47	1.03	—	0.36
35X-7	322.56	9,907.35	0.81	1.83	—	—
36X-7	332.84	6,349.51	—	0.85	0.32	0.54
38X-6	350.91	3,096.61	—	0.74	—	—
339-U1391C-						
3R-4	350.00	7,884.27	1.79	3.29	—	—
4R-2	356.60	3,600.97	—	1.03	—	—
5R-4	369.20	11,617.39	0.7	2.55	—	—
6R-2	375.80	6,535.09	0.76	1.89	—	—
7R-4	388.40	8,039.93	0.42	2.31	0.32	0.43
8R-3	396.50	6,864	0.55	1.57	—	0.56
9R-6	410.50	5,506.78	1.19	4.74	—	—
10R-5	418.60	2,807.05	0.48	1.32	—	—
11R-6	429.71	2,468.39	0.75	0.41	—	—
12R-7	440.81	3,281.06	—	0.67	—	—
13R-7	450.30	6,411.36	—	1.23	—	—
14R-7	459.91	1,627.41	1.05	—	—	—
15R-7	468.75	2,087.48	0.89	0.52	—	—
16R-6	477.50	2,487.33	0.87	0.62	—	—
17R-3	482.70	7,445.49	0.91	1.87	—	—
18R-6	496.50	8,057.85	0.85	2.37	—	0.42
19R-5	504.60	4,827.74	1.2	1.66	—	0.33
20R-2	509.60	5,064.61	—	1.68	—	—
21R-5	523.70	3,655.72	0.74	1.22	—	—
22R-5	533.30	4,400	1.27	2.22	—	—
23R-5	543.02	14,689.29	1.08	3.74	—	0.39
24R-5	552.60	3,253.71	—	1.04	—	—
25R-7	565.20	3,510.22	0.93	0.65	—	—
27R-6	582.88	5,085.88	1.11	2.59	—	—
28R-7	594.00	4,055.11	—	1.52	0.63	—
30R-7	613.20	3,752.66	1.03	1.72	0.3	—
31R-7	622.51	3,007.5	0.56	1.53	0.58	—
32R-7	632.40	1,062.85	0.91	1.04	0.43	—
33R-6	640.51	12,381.82	2.59	7.17	—	4.76
34R-5	648.60	7,763.52	1.18	2.24	—	0.54
36R-4	666.30	1,276.15	0.81	0.95	—	—

— = no data.



Table T15. Results from coulometric and CHNS analysis on whole-round squeezecake samples, Hole U1391A.

Core, section	Depth (mbsf)	Calcium carbonate (wt%)	Inorganic carbon (wt%)	Total carbon (wt%)	Nitrogen (wt%)	Organic carbon (wt%)	C/N
339-U1391A-							
1H-3	3.75	27.321	3.276	4.19	0.08	0.91	11.38
2H-6	12.70	22.653	2.716	3.59	0.07	0.87	12.43
3H-6	22.25	21.987	2.636	3.45	0.09	0.81	9.00
4H-6	31.97	22.704	2.722	3.38	0.07	0.66	9.43
5H-6	41.49	26.718	3.203	3.93	0.07	0.73	10.43
6H-6	50.92	24.774	2.970	3.86	0.06	0.89	14.83
7H-6	60.67	31.517	3.779	4.68	0.08	0.9	11.25
8H-6	69.73	32.072	3.845	5.13	0.07	1.28	18.29
9H-6	79.23	45.256	5.426	6.82	0.08	1.39	17.38
10H-6	88.46	26.163	3.137	4.06	0.08	0.92	11.50
11H-7	99.16	26.438	3.170	3.70	0.06	0.53	8.83
12H-6	106.44	40.143	4.813	6.11	0.09	1.30	14.44
13H-6	116.55	23.072	2.766	3.25	0.06	0.48	8.00
14H-6	126.55	43.494	5.215	6.83	0.09	1.62	18.00
15H-6	135.92	29.486	3.535	4.58	0.07	1.04	14.86
16H-6	144.58	29.198	3.501	4.65	0.08	1.15	14.38
17H-6	154.98	30.479	3.654	4.58	0.07	0.93	13.29
18H-6	163.28	33.479	4.014	5.26	0.09	1.25	13.89
19H-3	169.52	23.402	2.806	—	—	—	—
20X-5	178.45	17.559	2.105	3.90	0.08	1.79	22.38
21X-5	187.77	36.813	4.414	5.77	0.09	1.36	15.11
22X-7	198.56	34.836	4.177	5.48	0.07	1.3	18.57
23X-6	207.76	26.212	3.143	4.16	0.07	1.02	14.57
25X-6	226.74	23.330	2.797	3.62	0.08	0.82	10.25
26X-6	236.17	23.727	2.845	3.60	0.08	0.76	9.50
27X-6	245.94	18.899	2.266	2.98	0.08	0.71	8.88
28X-6	254.95	21.038	2.522	3.35	0.09	0.83	9.22
29X-6	265.15	30.533	3.661	4.64	0.09	0.98	10.89
30X-6	275.13	30.150	3.615	4.72	0.09	1.11	12.33
31X-6	283.21	27.810	3.334	4.17	0.09	0.84	9.33
32X-6	294.41	21.415	2.568	3.05	0.07	0.48	6.86
33X-4	301.53	23.516	2.820	3.60	0.08	0.78	9.75
34X-6	313.85	19.649	2.356	3.05	0.09	0.69	7.67
35X-6	322.05	30.700	3.681	4.78	0.10	1.10	11.00
36X-6	332.71	20.579	2.467	3.27	0.09	0.80	8.89
37X-6	341.37	22.836	2.738	3.41	0.08	0.67	8.38
38X-6	351.66	28.027	3.360	4.23	0.09	0.87	9.67

— = no data.



Table T16. Interstitial water major and minor elements, Site U1391. (Continued on next three pages.)

Core, section, interval (cm)	Depth (mbsf)	B (μM) 249.772 nm ICPAES	Ba (μM) 455.40 nm ICPAES	Fe (μM) 239.56 nm ICPAES	Li (μM) 670.78 nm ICPAES	Si (μM) 288.16 nm ICPAES	Sr (μM) 407.77 nm ICPAES	Alkalinity (meq/L) TITRA_AUTO
339-U1391A-								
1H-2, 145–150	2.95	489.59	2.74	37.11	0.00	319.88	76.32	8.17
2H-6, 135–140	12.95	553.92	2.82	13.20	0.00	251.82	61.87	15.82
3H-6, 126–131	22.36	469.71	36.07	4.29	1.36	182.96	68.45	9.89
4H-6, 145–150	32.05	450.89	28.79	2.38	1.02	202.84	69.64	7.72
5H-6, 145–150	41.55	452.91	40.30	1.57	1.54	150.07	76.97	6.26
6H-6, 145–150	51.10	413.42	34.11	7.56	1.27	231.39	79.16	6.95
7H-5, 145–150	59.23	396.73	38.11	19.08	1.43	392.78	85.49	7.19
8H-6, 131–141	69.79	400.54	38.92	14.46	1.52	178.41	83.50	5.96
9H-6, 136–141	79.31	426.00	38.88	8.08	1.46	149.87	91.37	5.41
10H-6, 136–141	88.60	405.11	35.55	18.32	1.33	247.97	86.69	6.72
11H-6, 135–140	97.84	355.11	34.54	3.59	1.26	143.12	87.49	6.16
12H-7, 136–141	107.89	354.18	32.18	3.97	1.13	190.57	86.55	6.92
13H-7, 105–110	117.72	324.42	33.38	2.38	1.19	179.56	84.55	7.35
14H-6, 146–151	126.66	335.94	35.14	3.33	1.27	255.79	85.45	8.24
15H-6, 126–131	135.99	357.54	38.03	5.34	1.40	226.48	89.21	8.56
16H-7, 147–152	146.23	257.08	46.22	1.63	1.76	235.98	87.86	8.24
17H-6, 137–142	155.11	293.65	51.41	1.35	2.03	268.07	90.20	9.44
18H-7, 132–142	165.33	295.68	54.23	3.32	2.16	308.92	88.16	8.63
20X-4, 140–150	177.00	294.52	55.63	2.63	2.22	309.35	92.72	NA
21X-4, 133–143	186.53	284.38	58.48	1.51	2.36	180.12	93.39	NA
22X-3, 140–150	193.65	257.63	60.75	1.49	2.46	234.18	98.11	NA
23X-3, 140–150	204.20	286.94	60.91	1.54	2.45	240.58	94.78	NA
25X-3, 140–150	223.40	246.57	65.49	1.56	2.70	272.24	99.84	6.96
26X-5, 140–150	234.80	257.49	60.57	3.91	2.45	233.20	98.68	6.41
27X-2, 140–150	241.10	257.97	59.46	1.95	2.39	253.04	103.69	8.08
28X-3, 140–150	252.21	299.88	51.52	1.46	1.93	592.36	104.48	8.92
29X-3, 134–144	261.75	232.44	51.49	1.29	1.91	385.32	106.94	7.85
30X-3, 140–150	270.92	241.46	49.47	1.43	1.79	419.20	107.68	9.44
31X-2, 141–151	279.51	208.81	50.24	1.46	1.84	312.71	105.26	7.19
32X-3, 140–150	290.09	230.06	49.86	1.92	1.86	338.54	103.26	6.89
33X-2, 140–150	298.70	216.39	51.64	7.48	1.98	501.61	106.97	7.97
34X-3, 140–150	309.50	262.31	52.76	3.43	2.02	241.70	111.99	7.32
35X-5, 138–148	321.56	257.00	50.53	7.30	1.95	493.38	110.25	7.28
36X-3, 141–151	328.44	216.90	55.30	1.53	2.17	209.45	109.77	5.99
37X-6, 135–150	341.42	223.09	56.93	1.70	2.26	235.96	112.23	5.79
38X-5, 135–150	350.76	224.24	52.67	3.07	2.02	384.06	115.94	5.83



Table T16 (continued). (Continued on next page.)

Core, section, interval (cm)	Depth (mbfs)	pH ISE	Cl ⁻ (mM) TITRA_AUTO	SO ₄ ²⁻ (mM) IC	Na ⁺ (mM) IC	K ⁺ (mM) IC	Mg ²⁺ (mM) IC	Ca ²⁺ (mM) IC	Na ⁺ /Cl ⁻	NH ₄ ⁺ (μ M) SPEC
339-U1391A-										
1H-2, 145–150	2.95	7.87	580.05	21.84	478.19	11.92	52.24	8.57	0.82	441.10
2H-6, 135–140	12.95	7.75	574.92	3.80	468.37	10.44	43.72	4.04	0.81	2,169.40
3H-6, 126–131	22.36	7.96	573.72	0.00	469.79	9.50	37.08	2.90	0.82	2,297.90
4H-6, 145–150	32.05	7.93	571.85	0.00	456.96	8.61	33.18	3.70	0.80	2,705.00
5H-6, 145–150	41.55	7.98	NA	0.00	478.28	8.55	33.89	4.22	NA	2,865.80
6H-6, 145–150	51.10	7.92	569.16	0.00	460.17	8.57	31.90	4.49	0.81	3,050.40
7H-5, 145–150	59.23	7.91	568.12	0.00	461.83	8.22	31.26	4.92	0.81	3,453.40
8H-6, 131–141	69.79	7.92	566.28	0.00	460.38	8.09	30.21	4.95	0.81	4,003.00
9H-6, 136–141	79.31	7.99	562.35	0.00	498.79	8.76	32.04	5.34	0.89	4,115.40
10H-6, 136–141	88.60	7.87	566.94	0.00	470.51	8.04	30.22	5.48	0.83	4,032.50
11H-6, 135–140	97.84	7.98	560.24	0.00	480.93	8.44	30.70	5.14	0.86	4,401.80
12H-7, 136–141	107.89	7.98	563.26	0.00	495.63	8.96	31.93	5.08	0.88	4,565.30
13H-7, 105–110	117.72	8.02	566.25	0.00	484.43	9.12	31.38	4.91	0.86	5,160.60
14H-6, 146–151	126.66	7.97	560.34	0.00	487.67	9.17	31.53	4.61	0.87	5,165.60
15H-6, 126–131	135.99	8.00	560.29	0.00	488.32	8.61	31.80	4.69	0.87	4,945.10
16H-7, 147–152	146.23	8.12	560.03	0.00	489.82	8.62	30.94	4.44	0.87	5,171.90
17H-6, 137–142	155.11	8.05	561.90	0.00	472.15	8.23	29.56	4.76	0.84	5,660.50
18H-7, 132–142	165.33	7.94	559.09	0.00	461.74	7.89	28.56	4.62	0.83	5,811.40
20X-4, 140–150	177.00	NA	560.13	0.00	471.04	7.79	28.38	4.95	0.84	6,063.40
21X-4, 133–143	186.53	NA	558.37	0.00	499.58	8.38	29.19	5.19	0.89	6,655.90
22X-3, 140–150	193.65	NA	553.75	0.00	487.40	7.65	29.38	6.18	0.88	5,887.20
23X-3, 140–150	204.20	NA	557.63	0.00	477.03	7.47	27.09	5.41	0.86	7,067.30
25X-3, 140–150	223.40	8.12	557.02	0.00	477.81	7.11	27.58	5.83	0.86	6,717.00
26X-5, 140–150	234.80	7.82	557.37	0.00	469.32	6.87	26.19	5.57	0.84	7,574.10
27X-2, 140–150	241.10	7.80	557.37	0.00	497.76	7.06	27.90	7.17	0.89	7,388.10
28X-3, 140–150	252.21	7.65	558.53	0.00	484.53	6.78	27.93	7.17	0.87	7,918.80
29X-3, 134–144	261.75	7.83	557.15	0.00	468.31	6.68	27.06	7.28	0.84	7,449.90
30X-3, 140–150	270.92	7.75	555.83	0.00	474.25	6.48	26.67	7.64	0.85	7,369.10
31X-2, 141–151	279.51	7.73	557.81	0.00	500.26	7.27	27.43	7.35	0.90	7,528.50
32X-3, 140–150	290.09	7.93	554.64	0.00	478.47	7.01	25.62	6.76	0.86	7,859.14
33X-2, 140–150	298.70	7.92	553.98	0.00	469.13	6.52	25.59	7.23	0.85	7,209.79
34X-3, 140–150	309.50	7.94	557.43	0.00	479.16	6.25	26.06	7.34	0.86	6,806.14
35X-5, 138–148	321.56	7.79	556.13	0.00	467.50	6.13	24.90	7.22	0.84	6,834.92
36X-3, 141–151	328.44	8.06	551.81	0.00	494.67	6.53	26.28	7.23	0.90	6,445.31
37X-6, 135–150	341.42	8.04	553.84	0.00	464.46	6.11	24.19	6.78	0.84	6,844.05
38X-5, 135–150	350.76	7.91	552.87	0.00	497.61	6.53	26.97	7.82	0.90	6,713.47



Table T16 (continued). (Continued on next page.)

Core, section, interval (cm)	Depth (mbsf)	B (μM) 249.772 nm ICPAES	Ba (μM) 455.40 nm ICPAES	Fe (μM) 239.56 nm ICPAES	Li (μM) 670.78 nm ICPAES	Si (μM) 288.16 nm ICPAES	Sr (μM) 407.77 nm ICPAES	Alkalinity (meq/L) TITRA_AUTO
339-U1391C-								
3R-3, 140–150	349.90	244.82	60.08	0.83	1.25	488.53	109.04	5.93
4R-1, 140–150	356.50	236.29	59.29	0.39	1.41	314.96	116.02	6.49
5R-3, 140–150	369.10	216.83	58.19	0.81	1.10	467.94	111.99	5.94
6R-1, 140–150	375.70	241.72	57.64	0.90	1.14	332.90	113.74	6.26
7R-3, 140–150	388.30	208.63	59.92	1.75	1.16	355.54	110.49	6.12
8R-2, 140–150	396.40	214.21	62.33	-0.05	1.41	274.24	111.43	6.42
9R-4, 140–150	407.50	270.24	53.47	3.29	0.93	362.85	120.43	7.24
10R-4, 140–150	418.50	255.13	63.26	1.69	1.34	605.34	113.35	8.68
11R-5, 141–151	429.61	213.44	64.38	1.79	1.51	342.48	112.87	8.73
12R-6, 141–151	440.71	227.85	66.30	0.27	1.43	373.78	110.39	9.08
13R-5, 140–150	448.70	219.22	64.21	0.94	1.57	351.82	114.13	9.43
14R-6, 136–151	459.76	239.40	63.05	1.64	1.02	521.67	106.69	12.48
15R-6, 135–150	468.60	253.54	62.28	3.87	0.98	542.62	111.82	14.42
16R-5, 135–150	477.35	226.19	59.51	1.08	1.09	416.41	113.22	14.99
17R-2, 135–150	482.55	233.48	56.16	0.74	0.55	376.28	107.67	14.53
18R-4, 135–150	494.85	283.70	61.01	1.29	1.14	409.57	123.32	19.61
19R-4, 135–150	504.45	211.44	61.72	0.65	0.60	445.71	111.06	19.85
20R-1, 135–150	509.45	225.68	63.24	0.97	0.99	460.28	120.24	22.12
21R-4, 135–150	523.55	232.77	71.27	1.15	0.91	774.30	127.36	27.89
22R-4, 135–150	533.15	253.01	69.83	1.36	0.94	572.59	130.85	27.90
23R-4, 135–150	542.87	214.59	63.87	1.92	0.15	386.84	122.72	25.91
24R-4, 135–150	552.45	185.33	56.79	1.07	-0.09	351.89	110.93	25.06
25R-5, 135–150	563.55	284.36	89.37	7.40	1.59	677.61	145.95	36.31
27R-5, 135–150	582.73	279.07	76.84	3.39	0.54	859.34	162.12	37.03
28R-5, 135–150	592.35	280.54	103.48	18.89	1.95	884.28	166.13	39.51
30R-5, 135–150	611.55	260.47	99.31	1.01	0.95	869.56	162.76	NA
31R-4, 135–150	619.65	262.06	101.68	2.64	1.08	1020.62	178.06	39.02
32R-4, 135–150	629.24	265.32	107.66	4.35	1.32	921.49	175.36	36.56
33R-5, 138–150	640.39	258.04	107.14	4.13	1.27	787.01	179.17	36.41
34R-4, 135–150	648.45	285.03	100.02	3.18	0.49	892.52	179.55	35.50
36R-3, 135–150	666.15	257.58	97.66	3.46	0.28	911.64	183.63	37.01

TITRA_AUTO = automatic titration, SPEC = spectrometer, IC = ion chromatograph, ICPAES = inductively coupled plasma–atomic emission spectrometer, ISE = ion-selective electrode. NA = not available.



Table T16 (continued).

Core, section, interval (cm)	Depth (mbsf)	pH ISE	Cl ⁻ (mM) TITRA_AUTO	SO ₄ ²⁻ (mM) IC	Na (mM) IC	K (mM) IC	Mg (mM) IC	Ca (mM) IC	Na /Cl	NH ₄ ⁺ (μM) SPEC
339-U1391C-										
3R-3, 140–150	349.90	7.97	556.72	0.00	517.35	5.94	25.37	7.39	0.93	3,667.20
4R-1, 140–150	356.50	7.93	553.95	0.00	493.40	5.80	24.53	7.49	0.89	6,648.26
5R-3, 140–150	369.10	7.93	557.18	0.00	493.28	5.86	25.17	7.45	0.89	5,747.74
6R-1, 140–150	375.70	7.68	555.75	0.00	496.39	5.88	25.50	7.52	0.89	6,233.80
7R-3, 140–150	388.30	8.01	553.34	0.00	478.49	6.06	23.56	6.68	0.86	5,700.24
8R-2, 140–150	396.40	8.04	550.70	0.00	498.47	6.51	24.29	6.86	0.91	6,340.51
9R-4, 140–150	407.50	7.86	555.70	0.62	510.55	6.58	26.91	7.02	0.92	5,466.85
10R-4, 140–150	418.50	7.87	551.44	0.00	482.93	6.11	24.09	6.54	0.88	5,772.53
11R-5, 141–151	429.61	8.04	552.66	0.00	494.23	6.83	25.24	6.33	0.89	6,003.17
12R-6, 141–151	440.71	7.96	552.04	0.00	480.09	6.51	24.04	5.65	0.87	6,327.43
13R-5, 140–150	448.70	8.03	550.90	0.00	482.31	6.53	23.86	4.75	0.88	6,653.77
14R-6, 136–151	459.76	7.85	551.14	0.00	471.06	6.22	23.93	5.12	0.85	6,713.66
15R-6, 135–150	468.60	7.73	549.85	0.00	483.43	6.72	25.93	5.11	0.88	6,925.02
16R-5, 135–150	477.35	7.94	550.16	0.00	486.54	7.57	27.16	3.96	0.88	6,772.87
17R-2, 135–150	482.55	7.67	551.38	0.04	493.76	7.95	28.73	3.83	0.90	6,606.95
18R-4, 135–150	494.85	7.83	553.33	0.00	510.53	8.38	29.90	3.60	0.92	8,001.10
19R-4, 135–150	504.45	7.87	547.40	0.00	494.94	8.70	29.23	3.01	0.90	7,805.57
20R-1, 135–150	509.45	7.61	552.79	0.00	486.96	8.64	30.26	3.38	0.88	7,636.90
21R-4, 135–150	523.55	8.02	548.47	0.00	484.39	8.61	30.74	4.02	0.88	8,164.95
22R-4, 135–150	533.15	8.05	547.14	0.00	485.14	9.05	32.11	3.91	0.89	8,445.84
23R-4, 135–150	542.87	7.57	552.71	0.00	523.11	10.73	35.85	3.68	0.95	8,754.28
24R-4, 135–150	552.45	7.69	551.30	0.00	489.10	10.94	32.93	2.66	0.89	9,488.18
25R-5, 135–150	563.55	7.71	547.46	0.00	471.05	9.59	32.64	4.34	0.86	9,247.91
27R-5, 135–150	582.73	7.46	549.76	0.00	481.61	10.07	35.51	5.59	0.88	8,909.18
28R-5, 135–150	592.35	7.33	544.34	0.00	487.81	10.03	33.84	5.94	0.90	10,082.33
30R-5, 135–150	611.55	NA	547.49	0.00	506.80	11.26	34.68	5.64	0.93	10,190.42
31R-4, 135–150	619.65	7.53	549.82	0.00	501.71	10.89	34.87	7.05	0.91	10,268.90
32R-4, 135–150	629.24	7.21	545.77	0.00	500.64	10.08	32.85	6.41	0.92	10,549.80
33R-5, 138–150	640.39	7.28	546.38	0.00	483.38	10.40	31.81	6.32	0.88	11,060.64
34R-4, 135–150	648.45	7.29	545.65	0.00	469.74	10.34	31.54	5.88	0.86	11,152.90
36R-3, 135–150	666.15	7.36	549.89	0.00	475.35	10.44	33.50	5.92	0.86	10,223.47



Table T17. Interstitial water oxygen and hydrogen isotopes, Site U1391.

Core, section, interval (cm)	Depth (mbsf)	$\delta^{18}\text{O}$ (‰, VSMOW)	δD (‰, VSMOW)
339-U1391A-			
1H-2, 145–150	3.00	0.94	3.82
2H-6, 135–140	13.00	0.87	5.46
3H-6, 126–131	22.41	1.03	7.30
4H-6, 145–150	32.10	0.87	7.25
5H-6, 145–150	41.60	0.95	8.71
6H-6, 145–150	51.15	1.07	6.71
7H-5, 145–150	59.30	0.37	1.75
7H-5, 145–150	59.30	0.32	1.32
8H-6, 131–136	69.91	0.68	6.36
9H-6, 136–141	79.36	0.88	6.50
10H-6, 136–141	88.65	1.44	6.64
11H-6, 135–140	97.89	1.21	6.68
12H-7, 136–141	107.94	0.91	5.77
14H-6, 146–151	126.7	0.76	6.11
15H-6, 126–131	136.05	0.78	6.29
16H-7, 147–152	146.28	0.71	5.05
17H-6, 137–142	155.16	0.74	5.07
18H-7, 132–137	165.43	0.70	5.59
20X-4, 140–145	177.1	0.84	3.45
21X-4, 133–138	186.63	0.91	5.56
22X-3, 140–145	193.75	0.41	4.65

VSMOW = Vienna standard mean ocean water.

Table T18. Results from APCT-3 temperature profiles, Site U1391.

Core	Original depth (mbsf)	Tidal sea level height*	Corrected depth (mbsf)	In situ temperature (°C)	Thermal resistance (m²K/W)
339-U1391A-					
4H	32.0	-0.4	32.6	11.8	25.7
7H	59.5	0.7	61.1	†	
10H	87.4	1.3	89.6	12.6	71.4
13H	116.3	0.8	118.1	13.1	95.9
16H	146.0	-0.4	146.6	13.3	117.6
339-U1391B-					
2H	19.3	-1.3	19.0	†	
5H	47.2	-0.7	47.5	12.0	37.2
8H	74.4	0.6	76.0	12.5	60.7
11H	102.3	1.2	104.5	12.8	85.2
14H	131.4	0.6	133.0	13.2	106.1

* = -1.0 m tidal height when mudline Core 339-U1391A-1H was taken. † = large range of possible values from the temperature decay curve.



Table T19. Meters composite depth scale, Site U1391.

Core	Top depth			Core	Top depth						
	(mbsf)	(mcd)	Offset (m)		(mbsf)	(mcd)	Offset (m)				
339-U1391A-											
1H	0.00	0.00	0.00	18H	161.50	186.92	25.42				
2H	4.10	5.05	0.95	19X	171.00	197.02	26.02				
3H	13.60	15.64	2.04	20X	175.50	201.53	26.03				
4H	23.10	25.68	2.58	21X	185.10	212.72	27.62				
5H	32.60	35.63	3.03	22X	194.60	223.52	28.92				
6H	42.10	45.01	2.91	23X	204.20	233.62	29.42				
7H	51.60	55.36	3.76	24X	213.80	243.22	29.42				
8H	61.10	65.78	4.68	25X	223.40	252.82	29.42				
9H	70.60	75.56	4.96	26X	233.00	265.22	32.22				
10H	80.10	86.75	6.65	27X	242.60	275.82	33.22				
11H	89.60	97.41	7.81	28X	252.20	285.43	33.23				
12H	99.10	107.82	8.72	29X	261.80	298.04	36.24				
13H	108.60	118.35	9.75	30X	271.40	310.24	38.84				
14H	118.10	129.71	11.61	31X	281.00	319.84	38.84				
15H	127.60	143.14	15.54	32X	290.60	329.43	38.83				
16H	137.10	157.34	20.24	33X	300.20	342.78	42.58				
17H	146.60	170.33	23.73	34X	309.80	354.47	44.67				
18H	156.10	180.83	24.73	35X	319.00	367.27	48.27				
19H	165.60	191.33	25.73	36X	328.70	382.37	53.67				
20X	171.10	196.83	25.73	37X	338.20	395.07	56.87				
21X	180.70	206.68	25.98	38X	347.90	409.16	61.26				
22X	190.20	216.17	25.97	339-U1391C-							
23X	199.80	229.56	29.76	1W	0.00	0.79	0.79				
24X	209.40	239.16	29.76	2R	340.00	396.34	56.34				
25X	219.00	249.75	30.75	3R	345.50	403.90	58.40				
26X	228.60	260.35	31.75	4R	355.10	414.85	59.75				
27X	238.20	272.15	33.95	5R	364.70	425.79	61.09				
28X	247.80	282.75	34.95	6R	374.30	436.73	62.43				
29X	257.40	292.35	34.95	7R	383.90	447.68	63.78				
30X	267.00	306.26	39.26	8R	393.50	458.62	65.12				
31X	276.60	315.87	39.27	9R	403.00	469.45	66.45				
32X	286.20	325.48	39.28	10R	412.60	480.39	67.79				
33X	295.80	336.82	41.02	11R	422.20	491.34	69.14				
34X	305.10	348.11	43.01	12R	431.80	502.28	70.48				
35X	314.70	359.71	45.01	13R	441.30	513.11	71.81				
36X	324.30	373.50	49.20	14R	450.90	524.06	73.16				
37X	333.90	387.10	53.20	15R	460.50	535.00	74.50				
38X	343.50	398.69	55.19	16R	470.00	545.83	75.83				
339-U1391B-											
1H	0.00	0.79	0.79	17R	479.70	556.89	77.19				
2H	9.50	11.81	2.31	18R	489.00	567.49	78.49				
3H	19.00	21.30	2.30	19R	498.60	578.43	79.83				
4H	28.50	31.49	2.99	20R	508.10	589.26	81.16				
5H	38.00	41.52	3.52	21R	517.70	600.21	82.51				
6H	47.50	50.09	2.59	22R	527.30	611.15	83.85				
7H	57.00	60.69	3.69	23R	537.00	622.21	85.21				
8H	66.50	71.39	4.89	24R	546.60	633.15	86.55				
9H	76.00	80.99	4.99	25R	556.20	644.10	87.90				
10H	85.50	91.95	6.45	26R	565.80	655.04	89.24				
11H	95.00	102.65	7.65	27R	575.40	665.99	90.59				
12H	104.50	113.59	9.09	28R	585.00	676.93	91.93				
13H	114.00	123.47	9.47	29R	594.60	687.87	93.27				
14H	123.50	135.97	12.47	30R	604.20	698.82	94.62				
15H	133.00	149.26	16.26	31R	613.80	709.76	95.96				
16H	142.50	164.51	22.01	32R	623.40	720.71	97.31				
17H	152.00	175.81	23.81	33R	633.00	731.65	98.65				
				34R	642.60	742.59	99.99				
				35R	652.20	753.54	101.34				
				36R	661.80	764.48	102.68				



Table T20. Splice tie points for Site U1391. (Continued on next page.)

Hole, core, section, interval (cm)	Depth		Hole, core, section, interval (cm)	Depth	
	(mbsf)	(mcd)		(mbsf)	(mcd)
339-			339-		
U1391A-1H-2, 56.88	2.07	2.07	Tie to	U1391A-1H-1, 0	0.00
U1391B-1H-4, 54.8	5.06	5.85	Tie to	U1391B-1H-1, 127.5	1.28
U1391A-2H-6, 83.21	12.43	13.38	Tie to	U1391B-2H-1, 79.73	4.90
U1391B-2H-5, 11.37	15.61	17.92	Tie to	U1391A-2H-2, 6.73	11.07
U1391A-3H-7, 46.44	22.87	24.91	Tie to	U1391A-3H-2, 77.82	15.88
U1391B-3H-6, 122.5	27.73	30.03	Tie to	U1391B-3H-3, 61.44	22.61
U1391A-4H-5, 147.81	30.58	33.16	Tie to	U1391A-4H-3, 135.46	27.45
U1391B-4H-7, 22.14	37.58	40.57	Tie to	U1391B-4H-2, 16.77	30.17
U1391A-5H-6, 81.45	40.91	43.94	Tie to	U1391A-5H-4, 43.77	37.54
U1391B-5H-3, 145.86	42.46	45.98	Tie to	U1391B-5H-2, 91.7	40.42
U1391A-6H-6, 123.27	50.88	53.79	Tie to	U1391A-6H-1, 97.37	43.07
U1391B-6H-6, 55.03	55.45	58.04	Tie to	U1391B-6H-3, 70.4	51.20
U1391A-7H-6, 137.29	60.67	64.43	Tie to	U1391A-7H-2, 115.58	54.28
U1391B-7H-5, 125.72	62.93	66.62	Tie to	U1391B-7H-3, 81.94	60.74
U1391A-8H-6, 69.72	69.18	73.86	Tie to	U1391A-8H-1, 84.39	61.94
U1391B-8H-4, 53.71	71.29	76.18	Tie to	U1391B-8H-2, 104.65	68.97
U1391A-9H-7, 44.41	79.80	84.76	Tie to	U1391A-9H-1, 61.73	71.22
U1391B-9H-6, 114.7	84.29	89.28	Tie to	U1391B-9H-3, 93.68	79.77
U1391A-10H-6, 124.65	88.49	95.14	Tie to	U1391A-10H-2, 111.19	82.63
U1391B-10H-6, 21.59	92.74	99.19	Tie to	U1391B-10H-3, 55.47	88.69
U1391A-11H-5, 70.28	95.83	103.64	Tie to	U1391A-11H-2, 36.95	91.38
U1391B-11H-5, 62.56	101.29	108.94	Tie to	U1391B-11H-1, 98.9	95.99
U1391A-12H-6, 106	106.13	114.85	Tie to	U1391A-12H-2, 52.84	100.22
U1391B-12H-6, 107.17	111.29	120.38	Tie to	U1391B-12H-1, 125.52	105.76
U1391A-13H-7, 48	117.15	126.90	Tie to	U1391A-13H-2, 88.56	110.63
U1391B-13H-6, 33.31	121.40	130.87	Tie to	U1391A-13H-3, 61.3	117.43
U1391A-14H-5, 115.2	124.95	136.56	Tie to	U1391A-14H-1, 115.62	119.26
U1391B-14H-6, 105.1	131.65	144.12	Tie to	U1391B-14H-2, 0.59	124.09
U1391A-15H-6, 44.55	135.18	150.72	Tie to	U1391A-15H-1, 97.5	136.56
U1391B-15H-7, 131.01	141.94	158.20	Tie to	U1391B-15H-2, 103.39	144.15
U1391A-16H-7, 115.54	145.92	166.16	Tie to	U1391A-16H-2, 42.5	148.01
U1391B-16H-5, 141.48	149.73	171.74	Tie to	U1391B-16H-3, 2.59	153.23
U1391A-17H-5, 58.37	152.82	176.55	Tie to	U1391A-17H-1, 73.7	152.74
U1391B-17H-5, 55.11	158.30	182.11	Tie to	U1391B-17H-2, 24.68	157.38
U1391A-18H-6, 80.89	163.39	188.12	Tie to	U1391B-18H-1, 119.67	162.70
U1391B-18H-4, 145.97	166.99	192.41	Tie to	U1391A-19H-1, 107.5	166.68
U1391A-19H-4, 134.64	171.10	196.83	Append to	U1391A-20X-1, 0	171.10
U1391A-20X-4, 115.51	176.76	202.49	Tie to	U1391B-20X-2, 49.8	176.46
U1391B-20X-5, 21.39	180.67	206.70	Tie to	U1391A-21X-1, 2.45	180.72
U1391A-21X-5, 95.53	187.59	213.57	Tie to	U1391B-21X-1, 85.04	185.95
U1391B-21X-4, 88.66	190.25	217.87	Tie to	U1391A-22X-2, 115.14	191.90
U1391A-22X-7, 62.82	198.01	223.98	Tie to	U1391B-22X-1, 45.88	195.06
U1391B-22X-5, 96.13	201.56	230.48	Tie to	U1391A-23X-1, 91.9	200.72
U1391A-23X-4, 29.65	204.60	234.36	Tie to	U1391B-23X-1, 74.03	204.94
U1391B-23X-6, 144.66	213.17	242.59	Append to	U1391B-24X-1, 0.07	213.80
U1391B-24X-5, 116.69	220.97	250.39	Tie to	U1391A-25X-1, 63.65	219.64
U1391A-25X-3, 42.13	222.42	253.17	Tie to	U1391B-25X-1, 35.23	223.75
U1391B-25X-5, 124.34	230.64	260.06	Append to	U1391A-26X-1, 0	223.17
U1391A-26X-5, 78.31	234.18	265.93	Tie to	U1391B-26X-1, 70.68	234.36
U1391B-26X-6, 83.96	240.02	272.24	Append to	U1391A-27X-1, 1.64	238.22
U1391A-27X-5, 4.36	244.08	278.03	Tie to	U1391B-27X-2, 72.58	244.81
U1391B-27X-5, 100.04	249.59	282.81	Tie to	U1391A-28X-1, 5.64	247.86
U1391A-28X-4, 63.64	252.95	287.90	Tie to	U1391B-28X-2, 96.67	254.67
U1391B-28X-5, 140.9	259.11	292.34	Append to	U1391A-29X-1, 1.21	257.41
U1391A-29X-5, 88.97	264.14	299.09	Tie to	U1391B-29X-1, 104.77	262.85
U1391B-29X-7, 32.34	270.37	306.61	Tie to	U1391A-30X-1, 35.12	267.35
U1391A-30X-5, 136.53	273.70	312.96	Tie to	U1391B-30X-3, 75.54	274.12
U1391B-30X-7, 114.69	280.44	319.28	Tie to	U1391A-31X-3, 39.91	280.01
U1391A-31X-5, 9.21	282.09	321.36	Tie to	U1391B-31X-2, 2.2	282.52
U1391B-31X-6, 95.61	289.47	328.31	Tie to	U1391A-32X-3, 33.84	289.03
U1391A-32X-6, 63.22	293.63	332.91	Tie to	U1391B-32X-4, 1.91	294.08
U1391B-32X-6, 85	297.91	336.74	Append to	U1391A-33X-1, 0	295.80
U1391A-33X-5, 38.93	302.00	343.02	Tie to	U1391B-33X-1, 24	300.44
U1391B-33X-4, 119.23	305.89	348.47	Tie to	U1391A-34X-1, 36.12	305.46
U1391A-34X-6, 103.03	313.60	356.61	Tie to	U1391B-34X-2, 64.18	311.94
U1391B-34X-6, 108.26	318.38	363.05	Tie to	U1391A-35X-3, 86.42	318.04



Table T20 (continued).

Hole, core, section, interval (cm)	Depth		Hole, core, section, interval (cm)	Depth		
	(mbsf)	(mcd)		(mbsf)	(mcd)	
U1391A-35X-7, 103.87	323.60	368.61	Tie to	U1391B-35X-2, 66.24	320.34	368.61
U1391B-35X-6, 42.33	325.83	374.10	Tie to	U1391A-36X-1, 60	324.90	374.10
U1391A-36X-7, 75.79	333.60	382.80	Tie to	U1391B-36X-1, 42.5	329.13	382.80
U1391B-36X-7, 72.59	337.57	391.24	Tie to	U1391A-37X-4, 67.79	338.04	391.24
U1391A-37X-7, 65.51	342.23	395.43	Tie to	U1391B-37X-1, 35.75	338.56	395.43
U1391B-37X-5, 54.57	344.75	401.62	Tie to	U1391A-38X-3, 2.46	346.43	401.62
U1391A-38X-6, 39.51	351.31	406.50	Tie to	U1391C-3R-2, 110.45	348.10	406.50
U1391C-3R-5, 82.5	352.33	410.73	Tie to	U1391B-38X-2, 7.37	349.47	410.73
U1391B-38X-5, 72.02	354.14	415.40	Tie to	U1391C-4R-1, 55	355.65	415.40
U1391C-4R-2, 130.11	357.90	417.66	Append to	U1391C-5R-1, 0	364.70	425.79
U1391C-5R-7, 71.06	374.41	435.50	Append to	U1391C-6R-1, 0	374.30	436.73
U1391C-6R-2, 137.5	377.18	439.61	Append to	U1391C-7R-1, 0	383.90	447.68
U1391C-7R-5, 137.73	391.28	455.05	Append to	U1391C-8R-1, 0	393.50	458.62
U1391C-8R-5, 68.18	399.87	464.99	Append to	U1391C-9R-1, 0	403.00	469.45
U1391C-9R-6, 152.02	412.02	478.47	Append to	U1391C-10R-1, 0	412.60	480.39
U1391C-10R-5, 89.23	419.49	487.29	Append to	U1391C-11R-1, 0	422.20	491.34
U1391C-11R-6, 132.16	431.03	500.17	Append to	U1391C-12R-1, 0	431.80	502.28
U1391C-12R-7, 69.29	441.50	511.98	Append to	U1391C-13R-1, 0	441.30	513.11
U1391C-13R-7, 71.86	451.02	522.83	Append to	U1391C-14R-1, 0	450.90	524.06
U1391C-14R-7, 71.05	460.62	533.78	Append to	U1391C-15R-1, 2.5	460.53	535.03
U1391C-15R-7, 146.83	470.22	544.72	Append to	U1391C-16R-1, 0	470.00	545.83
U1391C-16R-6, 82.08	478.32	554.15	Append to	U1391C-17R-1, 0	479.70	556.89
U1391C-17R-4, 56.53	484.58	561.76	Append to	U1391C-18R-1, 0	489.00	567.49
U1391C-18R-7, 65	498.66	577.15	Append to	U1391C-19R-1, 0.84	498.61	578.44
U1391C-19R-7, 68.26	507.89	587.73	Append to	U1391C-20R-1, 0	508.10	589.26
U1391C-20R-3, 50.7	511.33	592.49	Append to	U1391C-21R-1, 0	517.70	600.21
U1391C-21R-7, 54.9	526.86	609.37	Append to	U1391C-22R-1, 0	527.30	611.15
U1391C-22R-7, 67.5	536.98	620.83	Append to	U1391C-23R-1, 0.03	537.00	622.21
U1391C-23R-7, 71.66	546.74	631.95	Append to	U1391C-24R-1, 0	546.60	633.15
U1391C-24R-7, 77.34	556.38	642.94	Append to	U1391C-25R-1, 0	556.20	644.10
U1391C-25R-7, 71.64	565.92	653.81	Append to	U1391C-27R-1, 0.12	575.40	665.99
U1391C-27R-6, 117.27	584.05	674.64	Append to	U1391C-28R-1, 0	585.00	676.93
U1391C-28R-7, 66.06	594.66	686.59	Append to	U1391C-30R-1, 0	604.20	698.82
U1391C-30R-7, 73.53	613.94	708.55	Append to	U1391C-31R-1, 0	613.80	709.76
U1391C-31R-7, 73.37	623.24	719.21	Append to	U1391C-32R-1, 2.17	623.42	720.73
U1391C-32R-7, 75.39	633.15	730.46	Append to	U1391C-33R-1, 1.61	633.02	731.67
U1391C-33R-6, 124.7	641.76	740.41	Append to	U1391C-34R-1, 0.68	642.61	742.60
U1391C-34R-7, 89.67	652.04	752.03	Append to	U1391C-36R-1, 0	661.80	764.48



Table T21. Magnetic susceptibility splice, Site U1391.

Core, section, interval (cm)	Depth			Magnetic susceptibility	Magnetic susceptibility cleaned
	(mbsf)	(mcd)	Offset (m)		
339-U1391A-					
1H-1, 0	0.000	0.00	0.00	23.00	
1H-1, 2.5	0.025	0.03	0.00	39.67	39.67
1H-1, 5	0.050	0.05	0.00	42.67	42.67
1H-1, 7.5	0.075	0.08	0.00	44.00	44.00
1H-1, 10	0.100	0.10	0.00	44.00	44.00
1H-1, 12.5	0.125	0.13	0.00	43.67	43.67
1H-1, 15	0.150	0.15	0.00	43.67	43.67
1H-1, 17.5	0.175	0.18	0.00	43.00	43.00
1H-1, 20	0.200	0.20	0.00	43.33	43.33
1H-1, 22.5	0.225	0.23	0.00	44.33	44.33
1H-1, 25	0.250	0.25	0.00	43.33	43.33
1H-1, 27.5	0.275	0.28	0.00	42.00	42.00
1H-1, 30	0.300	0.30	0.00	42.33	42.33
1H-1, 32.5	0.325	0.33	0.00	43.00	43.00
1H-1, 35	0.350	0.35	0.00	40.67	40.67
1H-1, 37.5	0.375	0.38	0.00	38.00	38.00
1H-1, 40	0.400	0.40	0.00	37.00	37.00
1H-1, 42.5	0.425	0.43	0.00	36.67	36.67
1H-1, 45	0.450	0.45	0.00	37.00	37.00
1H-1, 47.5	0.475	0.48	0.00	38.00	38.00
1H-1, 50	0.500	0.50	0.00	39.00	39.00
1H-1, 52.5	0.525	0.53	0.00	40.33	40.33
1H-1, 55	0.550	0.55	0.00	41.33	41.33
1H-1, 57.5	0.575	0.58	0.00	41.00	41.00
1H-1, 60	0.600	0.60	0.00	41.33	41.33
1H-1, 62.5	0.625	0.63	0.00	41.00	41.00
1H-1, 65	0.650	0.65	0.00	41.00	41.00
1H-1, 67.5	0.675	0.68	0.00	26.00	26.00
1H-1, 70	0.700	0.70	0.00	39.00	39.00
1H-1, 72.5	0.725	0.73	0.00	40.00	40.00
1H-1, 75	0.750	0.75	0.00	40.00	40.00
1H-1, 77.5	0.775	0.78	0.00	40.00	40.00
1H-1, 80	0.800	0.80	0.00	39.33	39.33
1H-1, 82.5	0.825	0.83	0.00	39.67	39.67
1H-1, 85	0.850	0.85	0.00	39.00	39.00
1H-1, 87.5	0.875	0.88	0.00	39.33	39.33
1H-1, 90	0.900	0.90	0.00	40.00	40.00
1H-1, 92.5	0.925	0.93	0.00	40.00	40.00
1H-1, 95	0.950	0.95	0.00	41.33	41.33
1H-1, 97.5	0.975	0.98	0.00	42.00	42.00
1H-1, 100	1.000	1.00	0.00	42.00	42.00
1H-1, 102.5	1.025	1.03	0.00	42.00	42.00
1H-1, 105	1.050	1.05	0.00	41.33	41.33
1H-1, 107.5	1.075	1.08	0.00	40.00	40.00
1H-1, 110	1.100	1.10	0.00	34.33	34.33
1H-1, 112.5	1.125	1.13	0.00	17.33	17.33
1H-1, 115	1.150	1.15	0.00	18.00	18.00
1H-1, 117.5	1.175	1.18	0.00	33.33	33.33
1H-1, 120	1.200	1.20	0.00	38.00	38.00
1H-1, 122.5	1.225	1.23	0.00	38.00	38.00
1H-1, 125	1.250	1.25	0.00	38.00	38.00
1H-1, 127.5	1.275	1.28	0.00	38.33	38.33
1H-1, 130	1.300	1.30	0.00	39.00	39.00
1H-1, 132.5	1.325	1.33	0.00	39.67	39.67
1H-1, 135	1.350	1.35	0.00	39.00	39.00
1H-1, 137.5	1.375	1.38	0.00	38.00	38.00
1H-1, 140	1.400	1.40	0.00	37.00	37.00
1H-1, 142.5	1.425	1.43	0.00	36.33	36.33
1H-1, 145	1.450	1.45	0.00	35.00	35.00
1H-1, 147.5	1.475	1.48	0.00	32.00	32.00

Only a portion of this table appears here. The complete table is available in [ASCII](#).



Table T22. Natural gamma radiation (NGR) splice, Site U1391.

Hole, core, section, interval (cm)	Depth			Error		
	(mbsf)	(mcd)	Offset (m)	NGR (cps)	(cps)	
339-						
U1391A-1H-1	0.00	0.00	0.00	21.9279	1.3211	0.0602
U1391A-1H-1, 10	0.10	0.10	0.00	20.4376	0.4421	0.0216
U1391A-1H-1, 20	0.20	0.20	0.00	22.6205	0.2521	0.0111
U1391A-1H-1, 30	0.30	0.30	0.00	23.6014	0.2567	0.0109
U1391A-1H-1, 40	0.40	0.40	0.00	23.3433	0.2627	0.0113
U1391A-1H-1, 50	0.50	0.50	0.00	23.6123	0.2639	0.0112
U1391A-1H-1, 60	0.60	0.60	0.00	25.2522	0.2704	0.0107
U1391A-1H-1, 70	0.70	0.70	0.00	26.2261	0.2746	0.0105
U1391A-1H-1, 80	0.80	0.80	0.00	26.6025	0.2763	0.0104
U1391A-1H-1, 90	0.90	0.90	0.00	26.7382	0.2769	0.0104
U1391A-1H-1, 100	1.00	1.00	0.00	26.6892	0.2760	0.0103
U1391A-1H-1, 110	1.10	1.10	0.00	22.8773	0.2590	0.0113
U1391A-1H-1, 120	1.20	1.20	0.00	23.8130	0.2556	0.0107
U1391A-1H-1, 130	1.30	1.30	0.00	26.7202	0.2688	0.0101
U1391A-1H-1, 140	1.40	1.40	0.00	26.7158	0.5481	0.0205
U1391A-1H-1, 150	1.50	1.50	0.00	24.8659	1.4868	0.0598
U1391A-1H-2, 10	1.60	1.60	0.00	28.0064	0.5698	0.0203
U1391A-1H-2, 30	1.80	1.80	0.00	29.0586	0.2807	0.0097
U1391A-1H-2, 50	2.00	2.00	0.00	29.4290	0.2890	0.0098
U1391B-1H-1, 130	1.30	2.09	0.79	28.7626	0.2777	0.0097
U1391B-1H-1, 150	1.50	2.29	0.79	27.3568	1.5426	0.0564
U1391B-1H-2, 10	1.61	2.40	0.79	32.8975	0.6529	0.0198
U1391B-1H-2, 30	1.81	2.60	0.79	34.1276	0.3014	0.0088
U1391B-1H-2, 50	2.01	2.80	0.79	36.3695	0.3163	0.0087
U1391B-1H-2, 70	2.21	3.00	0.79	37.8855	0.3210	0.0085
U1391B-1H-2, 90	2.41	3.20	0.79	36.1596	0.3147	0.0087
U1391B-1H-2, 110	2.61	3.40	0.79	36.5849	0.3157	0.0086
U1391B-1H-2, 130	2.81	3.60	0.79	33.8333	0.4424	0.0131
U1391B-1H-3, 10	3.11	3.90	0.79	37.0477	0.7235	0.0195
U1391B-1H-3, 30	3.31	4.10	0.79	37.9776	0.3163	0.0083
U1391B-1H-3, 50	3.51	4.30	0.79	37.9242	0.3221	0.0085
U1391B-1H-3, 70	3.71	4.50	0.79	38.0545	0.3217	0.0085
U1391B-1H-3, 90	3.91	4.70	0.79	39.1477	0.3258	0.0083
U1391B-1H-3, 110	4.11	4.90	0.79	39.3182	0.3258	0.0083
U1391B-1H-3, 130	4.31	5.10	0.79	35.9221	0.3068	0.0085
U1391B-1H-3, 150	4.51	5.30	0.79	34.8122	2.0500	0.0589
U1391B-1H-4, 10	4.61	5.40	0.79	38.3587	0.7459	0.0194
U1391B-1H-4, 30	4.81	5.60	0.79	40.5491	0.3258	0.0080
U1391B-1H-4, 50	5.01	5.80	0.79	41.8718	0.3364	0.0080
U1391A-2H-1, 90	5.00	5.95	0.95	37.0430	0.3180	0.0086
U1391A-2H-1, 110	5.20	6.15	0.95	37.0778	0.3175	0.0086
U1391A-2H-1, 130	5.40	6.35	0.95	34.3483	0.3007	0.0088
U1391A-2H-1, 150	5.60	6.55	0.95	23.3724	1.4025	0.0600
U1391A-2H-2, 10	5.70	6.65	0.95	39.5747	0.7667	0.0194
U1391A-2H-2, 30	5.90	6.85	0.95	40.1657	0.3244	0.0081
U1391A-2H-2, 50	6.10	7.05	0.95	39.6623	0.3285	0.0083
U1391A-2H-2, 70	6.30	7.25	0.95	36.9307	0.3175	0.0086
U1391A-2H-2, 90	6.50	7.45	0.95	38.0644	0.3218	0.0085
U1391A-2H-2, 110	6.70	7.65	0.95	40.0730	0.3286	0.0082
U1391A-2H-2, 130	6.90	7.85	0.95	36.8174	0.3103	0.0084
U1391A-2H-2, 150	7.10	8.05	0.95	34.7811	2.0483	0.0589
U1391A-2H-3, 10	7.20	8.15	0.95	40.7662	0.7870	0.0193
U1391A-2H-3, 30	7.40	8.35	0.95	40.6276	0.3261	0.0080
U1391A-2H-3, 50	7.60	8.55	0.95	41.5980	0.3354	0.0081
U1391A-2H-3, 70	7.80	8.75	0.95	41.2260	0.3332	0.0081
U1391A-2H-3, 90	8.00	8.95	0.95	38.4049	0.3231	0.0084
U1391A-2H-3, 110	8.20	9.15	0.95	38.8278	0.3240	0.0083
U1391A-2H-3, 130	8.40	9.35	0.95	36.2078	0.3079	0.0085
U1391A-2H-4, 10	8.70	9.65	0.95	38.3261	0.7454	0.0194

Only a portion of this table appears here. The complete table is available in [ASCII](#).

